PREMIXED FLAME KINEMATICS IN A HARMONICALLY OSCILLATING VELOCITY FIELD

A Dissertation
Presented to
The Academic Faculty

by

Dong-hyuk Shin

In Partial Fulfillment
of the Requirements for the Degree
Doctor of Philosophy in the
School of Aerospace Engineering

Georgia Institute of Technology
December 2012

PREMIXED FLAME KINEMATICS IN A HARMONICALLY OSCILLATING VELOCITY FIELD

Approved by:

Dr. Tim Lieuwen, Advisor
School of Aerospace Engineering
Georgia Institute of Technology

Dr. Yingjie Liu
School of Mathematics
Georgia Institute of Technology

Dr. Suresh Menon
School of Aerospace Engineering
Georgia Institute of Technology

Dr. V. Yang
School of Aerospace Engineering
Georgia Institute of Technology

Dr. B. Zinn
School of Aerospace Engineering
Georgia Institute of Technology

Date Approved: October 22, 2012

To my family

ACKNOWLEDGEMENTS

The development of this thesis was one of the most challenging parts of my life. Without the great help from people surrounding me, I could not achieve this. They are true giants to me. I like to thank my parents, sister, who provided me support from the distance. I also thank Eunha for her constant support. All my burdens are blown out by her smile.

I deeply appreciate all the support from my advisor, Tim Lieuwen. He guided me to do good research, and showed me how to get things done. He is a great mentor and a role model. Without him, I would not achieve this much. I hope everything goes well with him, his family and his team. I would like to thank all the faculty members of Aerospace Engineering in Georgia Tech. They taught me the best, and helped me to construct solid basis.

I would like to thank all people from the combustion lab. I thank my seniors for their thorough training on me. Preetham, Santosh S., and Santosh H., I still vividly remember when I fought back to you about the concept of local isotropy. I also thank my crew of class 2012, Jackie, Jack, and Shreekrishna. We took classes together, did the research, and studied/passed the qualifying exam together. I never felt lonely and separated in the lab, and my qual exam would be hell without you guys. I also thank my colleagues, Vishal, Prabhakar, Ben E., Bobby, Ben W., Andrew, Ianko, Chris, Jordan, Alberto, Mike M., and Mike A. for keeping good research. I know our lab has bright future as we have smart young generations. All are up to you, Nick and Luke.

I also like to thank Korean gangs in Aerospace Engineering. 감사합니다! They are persons from many disciplines, so I can confer them for any new problems. I thank to Jaecheol Kim, who guided me and helped me in many ways. He was my roommate for 5

years! I also thank to Wongsik Choi, Yongjae Kim, Kyunghak Choo, and all other members.

Finally, I gratefully acknowledge the support of National Science Foundation, GE Energy for their financial support to make this work possible.

TABLE OF CONTENTS

LIST OF FIGURES

LIST OF SYMBOLS AND ABBREVIATIONS

$\widehat{C}$: progress variable
L_{11} : longitudinal integral length scale
L_f : Flame length measured in flow direction
R_{XY} : Correlation function between scalar values of X and Y
S_L : laminar flame speed
$S_{L,0}$: laminar, unstretched flame speed
S_T : turbulent flame speed
$S_{T,0}$: effective turbulent flame speed, $S_{T,\,eff}$, at zero mean curvature, defined in Eq. (7.32)
$S_{T,eff}$: effective turbulent flame speed, defined in Eq. (7.27)
$S_{T,disp}$: local displacement flame speed based on time average flow properties, defined in Eq. (7.28)
W_f : Flame width measured in the radial or transverse direction
c : flame curvature
f_0 : forcing frequency
n : coordinate normal to unforced flame front
s : coordinate tangential to unforced flame front
u : scalar velocity components
u_0 : mean velocity in the x-direction
u_a' : velocity fluctuation upstream of the bluff-body
$u_{c,v}$: phase speed of the velocity disturbance in the x-direction
$u_{c,f}$: the natural flame convection speed in the x-direction
$u_{s,0}$: mean velocity in the tangential direction to the unperturbed flame sheet
u_s : velocity in the s -direction
u_n : velocity in the n-direction
x : coordinate in the flow direction
y : coordinate normal to the flow direction
z : coordinate perpendicular to x-y plane
Σ^2 : variance of Gaussian random variable
$\nabla_{,t}$: tangential derivative
ε : oscillation magnitude of the flame holder
κ : flame front stretch rate
γ : exponential vortex decay rate
λ_0 : wavelength corresponding to u_0 (:u_0/f_0)
λ_c : wavelength corresponding to $u_{c,v}$ (:$u_{c,v}/f_0$)
λ_f : wavelength corresponding to $u_{c,f}$ (:$u_{c,f}/f_0$)
σ : Markstein length
σ_T : turbulent Markstein length
ω_0 : radial forcing frequency, $2\pi f_0$
ξ : flame position measured in y- or n-direction

ψ : initial phase

$(\ )_{\Theta}$: function corresponding to the order of Θ from the Taylor series expansion

$\tilde{(\ )}$: Non-dimensional form of a variable

$\tilde{(\ )}$: Non-dimensional form of a variable

$\bar{(\ )}$: time average

$\langle\ \rangle$: Ensemble average

SUMMARY

This thesis describes the spatio/temporal dynamics of the harmonically excited flames. Analytical and numerical analyses were performed to study excitation and dissipation of wrinkles on the flame front. Modern gas turbine systems face major challenges from the onset of combustion instabilities. In order to avoid this problem, in-depth understanding of the dynamics of the flame front is required. This thesis is devoted to provide insights into complex combustion dynamic problems.

Dynamics of the flame front are tracked by the so-called G-equation. The G-equation relates the motion of the flame front with the laminar flame speed and the velocity on the flame front. This partial differential equation is quite complex so that obtaining the explicit solution is not generally possible. Firstly, this equation is inherently nonlinear because of flame propagation normal to the flame. Secondly, velocity terms involve stochastic components with the presence of turbulent flow. Finally, the laminar flame speed, which has a dependence on geometric shapes, increases the order of the partial differential equation. Therefore, extensive mathematical techniques are used to obtain explicit solutions to the flame dynamics.

Previous studies pointed out a generic feature about the flame response to the harmonic velocity disturbances: the magnitude of the flame response grows, reaches a peak or multiple peaks, and then decays with axial distance. This evolution can be understood by a competition between the excitation and the dissipation of the flame response. Excitation processes controls the flame response in the near field, while dissipation processes controls the response in the far field. The excitation processes are

studied in two regions, the near field and the far field. The near field analysis is universal so that it applies to a general velocity disturbance field. On the other hand, the far field analysis requires spatial characteristics of the velocity fluctuations so that a specific velocity disturbance model was used. For the dissipating processes, three mechanisms are studied: kinematic restoration, flame stretch, and turbulent flow effects. Asymptotic analysis identifies key dimensionless parameters and compares their relative contributions in dissipating the flame response.

In the near field, two mechanisms can excite the flame response. They are the unsteady flame base motion and the normal velocity fluctuation. The unsteady motion propagates downstream with the tangential velocity, while maintaining its magnitude. In addition, the normal velocity fluctuation causes a linear increase in the flame response either by harmonic or stochastic velocity fluctuations. Furthermore, the growth rate of the flame response is proportional to the ratio of normal velocity disturbance to the tangential velocity. This relationship was verified with measurements of bluff-body stabilized flames.

Moving into the far field, spatial characteristics of the velocity fluctuation are required to understand the flame response. It is found that depending on the decay rate of the velocity fluctuation, the flame response shows two different behaviors. If the velocity fluctuation persists further downstream, the flame response shows oscillatory gains as a result of interference between waves propagating along the flame sheet. However, this interference behavior can change due to the decay of the velocity disturbances. With high decay of velocity fluctuations, the corresponding wave cannot cause interference,

allowing the other wave to dominate further downstream. This dominance leads to a constant magnitude for the flame response in the far field.

Kinematic restoration, one of the dissipation processes, shows a two zone behavior in smoothing flame wrinkles. A wrinkle on a flame excited with a single frequency decays quadratically in the near field at an amplitude dependent rate. The presence of multiple frequencies in the excitation, such as an additional harmonic, leads to a linear decay in the near field amplitude. Thus, the harmonic content of the excitation plays an important role in the decay rate of flame wrinkles. In the far field, the wrinkle decays inversely with downstream distance at a rate that is independent of forcing amplitude.

The smoothing of flame wrinkles by stretch effects in positive Markstein length flames can be understood from linear analysis. The analysis shows that the wrinkle decay rate is an exponential function of Markstein length and downstream distance.

Finally, the effect of turbulent flow in smoothing out the ensemble-averaged flame front is analyzed. In the near field, asymptotic results show three leading order contributions: (i) the phase jitter associated with random tangential convection of flame wrinkles, (ii) random flame angle changes, and (iii) kinematic restoration coupled with length scales of the velocity fluctuations. Farther downstream, additional processes become important. First, the time averaged turbulent burning velocity increases with downstream distance and turbulence intensity. This faster average displacement velocity of the front leads to an increase in the destruction of flame wrinkles. In addition, the ensemble averaged turbulent burning velocity is modulated by the harmonic forcing, with an inverse dependence upon ensemble averaged flame curvature, i.e., the turbulent

burning velocity changes in time. This effect is exactly analogous to positive Markstein length flames in the laminar flame case, but applies even to the ensemble averaged characteristics of stretch-insensitive turbulent flames.

CHAPTER 1

INTRODUCTION

1.1 Motivation

Fire, one form of combustion, has helped people civilize. From prehistoric times, people have used fire to cook food in order to increase the variety and availability of nutrients and to create warmth and light in order to overcome harsh winter and dark nights. By gaining control of fire, people were able to develop civilizations. The ability to smelt metals from ore opened a new era of the Bronze Age and later opened the Iron Age.

Extracting energy from nature has given humanity the ability to conquer nature and produce conveniences for people. The steam engine powered the Industrial Revolution, when people learned to draw energy effectively from coal, and it changed the paradigm of agriculture, manufacturing, mining, and transportation. Later, electricity became the popular medium for energy consumptions. Nowadays, people can fly to opposite sides of the world in a day and even further into space.

In extracting energy from nature, burning fossil fuel has long existed, and it is still the most effective and popular way to draw energy. Burning fossil fuel powers transportation, factories, and electricity generation for general purposes. Fossil fuels will be a major energy resource for the next decades.

With all these benefits, people slowly started to realize the side effects of burning fossil fuel. This combustion process produces harmful products such as nitrogen oxides

(NO_x), sulfur oxides (SO_x), and etc. Nitrogen oxides and sulfur oxides cause acid rain and respiratory symptoms to people [1, 2]. For sulfur oxide, its emission can be effectively minimized by removing sulfur from the fuel in the preprocessing stage. However, nitrogen oxide, both of whose elements originate from air, cannot be completely removed in the burning process, but its production can be minimized by controlling the combustion process.

Therefore, many recent developments to combustion systems is driven by the goal of minimizing NO_x emission. The main driver in reducing NO_x emission is to decrease the operating temperature because the major production of nitrogen oxide is from high temperature zone [3]. Accordingly, new systems have been proposed to lower the operating temperature. For example, these include catalytic combustion, rich-burn quick-quench lean-burn combustion (RQL), and lean-premixed combustion. However, each system comes with its own disadvantages. Catalytic combustion comes with high cost, low durability and safety issues. RQL suffers from soot formation and mixing problems. Lean premixed combustion has challenges with flame stabilities, flashback, lean blow out. Significant efforts have been expanded toward these operability issues in premixed systems. Combustion instability, or combustion dynamics in bigger scope, is the key motivator for this work.

Although understanding combustion instability is an eminent problem, difficulties arise in attempting to understand the dynamics of the combustion of practical systems. For example, combustion research involves the coupling of fluid dynamics and chemical reactions. Fluid dynamics in the combustion system is complicated by the presence of turbulent flow, and chemical reaction is complicated by the thousands of elementary

reactions. However, among all these processes, some are more important and some are less. Identifying key processes on combustion system will clear the dust cloud and helps to design a better combustion system. Therefore, this thesis focuses on identifying leading order processes to provide insights in the combustion dynamics.

1.2 Combustion Instability

Combustion instability generally refers to the self-excited pressure fluctuations of acoustic nature in a combustion chamber. It is not limited to the gas turbine systems; rather it includes all combustion systems such as liquid rockets and industrial boilers. In order to develop efficient, safe, and eco-friendly combustion system, the understanding on combustion instability is crucial.

1.2.1 Previous Studies on Combustion Instability

Historically, combustion instability arises as a major challenge during the early fifties and sixties on aircraft and rockets. For example, Pogo oscillation, a term used in liquid rockets, delayed several rocket launching missions [4]. However, with lack of proper understanding, engineers had to rely on expensive repeated experiments. Especially, for Saturn V rocket motor, 2000 full scale tests were conducted to avoid combustion instability [5].

In the rocket engines, it is known that longitudinal oscillations cause severe damage to the combustion chamber. Figure 1.1 shows the time trace of unsteady pressure inside a solid rocket motor, where two pulses are forced to excite instabilities. The first pulse excites the tangential oscillation, but the oscillation is small compared to the mean pressure. However, when the second pulse is applied, the longitudinal oscillations are

excited, leading to large fluctuations in the pressure accompanied with the increased mean pressure. This experiment illustrates the high sensitivity of the rocket system to small external disturbances.

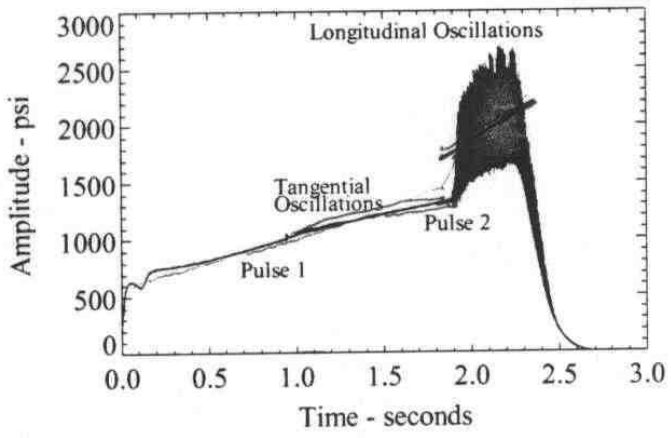

Figure 1.1. Example of solid rocket motor experience from Blomshield [6].

Later, gas turbine systems face a major challenge of combustion instability. Previously, industrial gas turbine systems operated with diffusion flames, where fuel and oxidizers are mixed at the combustion chamber. However, due to recent restrictions on emissions, engineers have moved to lean-premixed systems, where flame stability is the main challenge. This flame stability problem leads to frequent hardware failures and increased maintenance costs.

Combustion instability will continue to be a challenge as long as heat is a main energy source for human activities. Therefore, we should understand combustion dynamics better in order to extract energy from chemical reaction in clean, safe, and efficient ways.

1.2.2 Understanding the Combustion Instability

Lord Rayleigh was the first one to state a criterion, which describes the conditions under which a periodic heat addition process adds energy to acoustic oscillations. Following is a quote from his book, *The Theory of Sound* [7].

"If heat be given to the air at the moment of greatest condensation, or be taken from it at the moment of greatest rarefaction, the vibration is encouraged."

This criterion states that energy is added to the acoustic disturbances if unsteady heat release and unsteady pressure are in phase, which can be formulated as [8]:

$$\frac{1}{T}\int_0^T p'q'\,dt > 0 \tag{1.1}$$

Superficially, combustion instabilities seem to be easy to identify simply by knowing pressure and unsteady heat release. However, these identifications are quite difficult in real applications.

When it comes to prediction capabilities, evaluating Eq. (1.1) becomes extraordinarily difficult. Pressure and heat release are highly coupled and related by various flow/chemical/geometric parameters. For example, pressure fluctuations influence the fuel feeding system, which leads to the fluctuation in heat release [9], and unsteady heat release is a well known monopole acoustic source [10]. Therefore, instead of attempting to dissect Eq. (1.1) right away, people start to look at more elementary mechanisms in understanding interactions between pressure and unsteady heat release.

One promising approach to understanding these interactions is by utilizing so-called flame transfer functions. Dowling proposed that gas dynamic processes essentially remain in the linear regime, even under limit cycle operation [11]. For a linear process, a transfer function is a useful tool to understand instability. Subsequently, indentifying the heat release transfer function upon the flow oscillations becomes the major objectives for understanding combustion instability. Extensive measurements were performed to measure the heat release transfer function for various combustor designs. Santavicca and coworkers measured the various flame transfer function for a single nozzle configuration, and correlate with minimum response frequency with heat release center of mass [12, 13].

Candel and coworkers also performed flame transfer function measurements for various combustor configurations, such as Bunsen and slot burners [14-16]. One of their measurements is illustrated in Figure 1.2. These flame transfer function are also obtained by numerical simulations. Kornilov et al. performed numerical simulation with detailed binary diffusion with four species along with tabulation of CHEMKIN® package on multi-slit Bunsen burners and compare [17]. Poinsot and coworkers includes turbulent fluctuation and obtained many results [18, 19].

Modelling effort was followed as well. Modeling the flame transfer function using the G-equation was first attempted by Fleifil et al. [20], where they considered Poiseulle flow in a ducted chamber with a bulk velocity disturbance. Later, Lieuwen and coauthors developed more sophisticated models for transfer functions including fuel-air ratio fluctuations [13, 21], velocity disturbance [22], turbulent disturbance [23], and pressure disturbances [24]. One of the comparison shown in Figure 1.2b shows good agreement with measurements shown in Figure 1.2a, capturing quantitative/qualitative features. At low frequencies, gain approaches unity, and increases subsequently with the frequency. Then, the modeling predicts the oscillatory behavior which is also present in the measurements. Candel and coworkers also performed extensive study on modeling the flame transfer function using the G-equation [15, 16, 25].

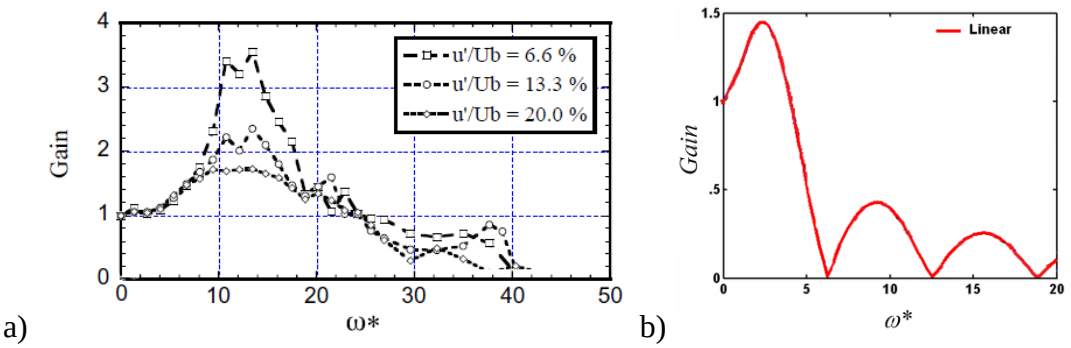

Figure 1.2 Dependency of gain of flame transfer function on frequency. a) Measured from V-flame [15], b) theoretical estimation by flamelet model [22].

However, most previous studies focused on obtaining the flame transfer function, an integrated value of distributed heat release. Significantly less attention was made to understand the spatio/temporal dynamics of the flame on the combustion instability. In addition, most previous studies have focused on the mechanisms for excitation of flame wrinkling, with significantly less attention given to the processes that smooth these wrinkles out.

1.3 Overview of Present Work

The objective of this research is to understand the spatio-temporal characteristics of harmonically forced premixed flames including processes that excites, transport and smooth-out flame perturbations. The remainder of this thesis is divided as follows. Chapter 2 starts with formulating the kinematic equation relating flame motion with various disturbances. Then, it reviews the early studies on combustion kinematics including kinematic restoration effect, flame stretch effect, and turbulent effect. Chapter 3 describes the methods used in this thesis to solve the flame front kinematic equations. Details about analytic and numerical methods are described. For the analytic methods, small perturbation methods, Hopf-Lax formula, and method of characteristics are presented with examples. For the numerical methods, two methods are presented. The first method is a level set method which can handle topological changes of flame front. The second method is solving its reduced model equation. This method is less general than the level set method, but still applicable to most laminar flames. Lastly, special treatments for the flame boundary and post-processing methods are explained, too.

New findings are presented in Chapter 4 through Chapter 7. Chapter 4 and Chapter 5 present analysis on excitations of the spatio/temporal response of the flame, while Chapter 6 and Chapter 7 cover analysis on dissipations of the response of the flame.

Chapter 4 covers the flame response near the flame holder, where the flame response starts to grow. It was found out that the growth rate of the flame response is proportional to the flow disturbance acting in flame normal direction. Quantitative comparison with measurements shows very good agreements. Chapter 5 extends this analysis further downstream and identifies two regimes by a flow dissipation parameter; *interference dominated regime* and *dissipation dominated regime*. In the interference dominated regime, the gain of flame response shows multiple peaks, and its peak axial locations can be predicted from an interference wavelength. In contrast, in the dissipation dominated regime, the gain of the flame response shows only single peak and decreases subsequently in a nonlinear fashion. Quantitative and qualitative comparisons with measurements are presented for both regimes.

Chapter 6 and Chapter 7 cover the processes leading to smoothing out wrinkles on the flame front. The Chapter 6 describes numerical and theoretical analyses of the nonlinear dynamics of harmonically forced, stretch-sensitive premixed flames. A key objective of this chapter is to analyze the relative contributions of kinematic restoration and flame stretch upon the rate at which flame wrinkles, excited by harmonic forcing, are smoothed out. Which process dominates is a function of the perturbation amplitude, frequency, stretch sensitivity of the mixture, and spatial location. Next, Chapter 7 describes numerical and theoretical analyses of the dynamics of harmonically forced, turbulent premixed flames. A key objective is to understand the role of the turbulent flow in dissipating the harmonic wrinkles on flames. In the near field, three mechanisms contribute to the decay of the flame response in the leading order; phase jitter, random flame angle change, and kinematic restoration induced by small scale velocity fluctuations. In the far field, ensemble-averaged flame fronts are further smoothed out by

the increase of the flame speed and the curvature-dependent flame speed fluctuations, whose effect is similar to thermodiffusive laminar flames. The dominant contributors vary with perturbation amplitude, turbulence intensity, and spatial location.

CHAPTER 2

FLAME FRONT KINEMATIC EQUATION

This chapter explains modeling approaches in the flamelet regime, and introduces the kinematic equation in the flamelet regime. Then, this chapter presents some of the general features found in the spatio/temporal flame response and reviews the elementary mechanisms influencing the flame response.

2.1 Flamelet Regime

Combustion in practical systems usually occurs in turbulent flows due to complex combustor geometries and high flow speeds. These turbulent flows consist of wide range fluctuations in length, time, and velocity scales. Therefore, it is beneficial to know different flame regimes of turbulent combustion. One of this categorization for premixed flames is the Borghi diagram [26, 27], where flame regimes are classified by two parameters, a normalized turbulent intensity, u_{rms}/S_L , and a normalized turbulent length scale, L_{11}/δ_F , as shown in Figure 2.1.

The discussion of this regime diagram closely follows Ref. [27]. Starting from the bottom left, the line of $\frac{u_{rms}}{S_L} \Big/ \frac{L_{11}}{\delta_f} = 1$ separates all turbulent regimes from the laminar flames due to low turbulent intensities. Moving into the turbulent regimes, there are two different regimes; the quasi-steady flamelet regime and the distributed reaction zone. If u_{rms}/S_L is lower than $\left(L_{11}/\delta_F\right)^{1/3}$ (quasi-steady flamelet regime), then turbulent length scale is not yet small enough to break thin flame thickness. Then, in the opposite case, ($u_{rms}/S_L > \left(L_{11}/\delta_F\right)^{1/3}$), lengths scales of turbulent flow get smaller than the flame

thickness so that turbulent fluctuation interferes the flame structure. This leads to reaction to occur all over the place inside the combustion chamber (Distributed reaction zone).

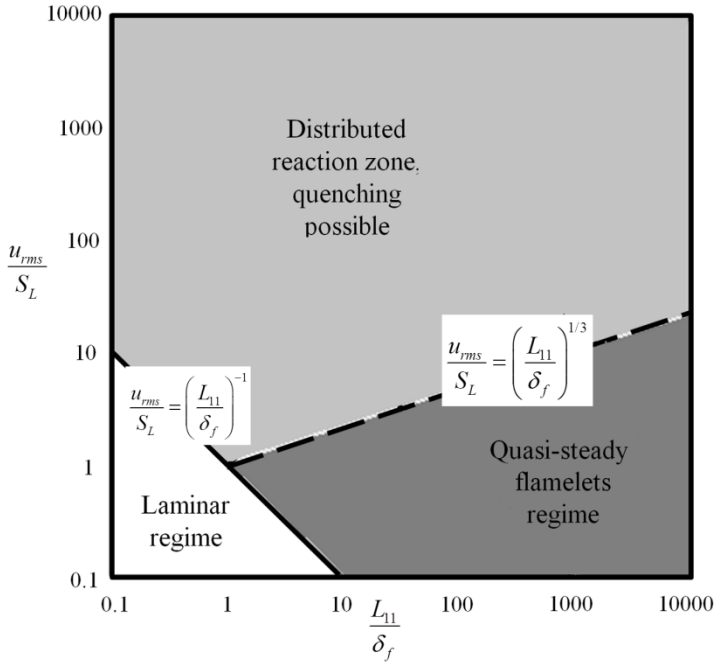

Figure 2.1 Turbulent combustion diagram illustrating different combustion regimes as a function of L_{11}/δ_F (integral length scale/flame thickness) and u_{rms}/S_L (turbulent velocity fluctuations/flame speed), reproduced from Ref. [27].

As many practical combustion systems operate within the quasi-steady flamelet regime [11], this thesis focuses on the analysis on the flamelet regime and laminar regime. In this flamelet regime, combustion processes occur within a very thin zone relative to different types of disturbance length scale. Therefore, the flame consists of thin layers separating reactants and products, and this layer is also called the flame front [27]. Details about dynamics of flame front in this regime are explained in the following section.

2.2 Flame Front Kinematic Equation

The flame front in the flamelet regime can be tracked by the so-called *G*-equation, which was first formulated by F. Williams [28] and is used extensively for various combustion problems such as theoretical flame transfer functions [20], theoretical turbulent consumption rate [29], and many computational fluid dynamics [30-32].

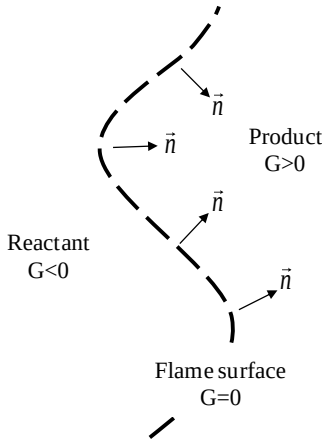

Figure 2.2 Instantaneous snapshot of a wrinkled laminar flame sheet, whose instantaneous positions are given by the parametric equation *G(x, y, z, t)* = 0 [26].

The flame front kinematic equation relates the motion of the flame front with various flow/flame parameters. Consider the flamelet as a gas dynamic discontinuity in three dimensional space described by the parametric equation, $G(\vec{x},t)=0$. In a flame fixed coordinate system (Lagrangian), the evolution of the *G* values on the flame does not change, which is expressed as:

$$\frac{D}{Dt}G(x,y,z,t)\Big|_{at\ the\ flame\ front}=0 \tag{2.1}$$

The above equation is, written in an Eulerian form as:

$$\frac{\partial G}{\partial t}+\vec{u}_f\cdot\nabla G=0 \tag{2.2}$$

where $\vec{u}_f$ is the velocity of the flame front. The velocity is then decomposed into sum of flow velocity and the normal flame propagation speed as $\vec{u}_f = \vec{u} - S_L \cdot \vec{n}$. Note that the normal direction to the flame front is $\vec{n} = \nabla G / |\nabla G|$ (see Figure 2.2). Then, Eq. (2.2) is rewritten as:

$$\frac{\partial G}{\partial t} + \vec{u} \cdot \nabla G = S_L |\nabla G| \tag{2.3}$$

In addition, the only condition of *G* outside the flamelet is non-zero. However, it is convenient to have negative values on the reactants side and positive values on the products side as shown in Figure 2.2.

In the unsteady case, the flame is being continually wrinkled by the unsteady flow field. On the contrary, the action of flame propagation normal to itself, the term on the right side of Eq. (2.3), is to smooth these wrinkles out through "Huygens propagation" / "kinematic restoration". A wrinkle created at one point of the flame due to a velocity perturbation propagates downstream and diminishes in size due to kinematic restoration. Indeed, the interaction between the excitation (acoustic/vortical flow oscillations) and the damping (restoration property of the flame) can lead to a range of effects depending upon flame stabilization and the relative values of the flow oscillations and flame speed. This equation is quite general so that it handles flames with complex, multi-connected surfaces, such as the flame shown in Figure 2.3.

Figure 2.3 Instantaneous edge of a highly contorted flame front [27].

A useful transformation of the G-equation is done by converting Eq. (2.3) in terms of the flame position, ξ. Although the equation for the flame position becomes less general than the *G*-equation, it enables us to track flame locations explicitly - note that in *G*-equation, the flame position is implicit function of *G*. Once these explicit flame positions are obtained, we can evaluate quantities such as flame surface area and flame curvature. A common way of transforming the *G*-equation to the flame position equation in 2D is by substituting $G(x,y,t) = y - \xi(x,t)$, where ξ represents the locations of the flame front, see Figure 2.4 for illustration. Then Eq. (2.3) is transformed into:

$$\frac{\partial \xi}{\partial t} + u_x \frac{\partial \xi}{\partial x} - u_y = S_L \sqrt{1 + \left(\frac{\partial \xi}{\partial x}\right)^2} \tag{2.4}$$

The left hand side of this equation is the usual convective operator. Therefore, in the absence of right hand side, any disturbance on the flame front is simply convected in the flow direction. The nonlinear forcing on the RHS in Eq. (2.4) originates from the property that flame fronts propagate normal to themselves. Geometrically, this property is similar to waves which propagate from every point source. This nonlinear operator can cause discontinuities in the slope of flame fronts, which is very hard to track by conventional asymptotic analysis.

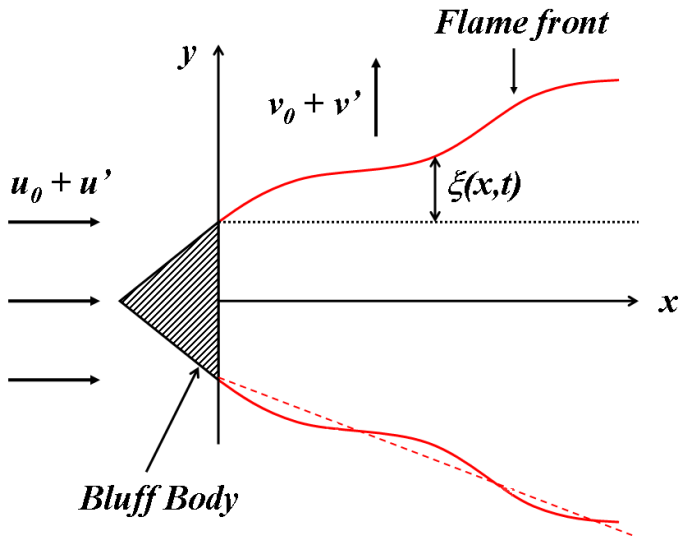

Figure 2.4. Schematic of bluff-body stabilized flame with its corresponding coordinates. red solid : instantaneous flame front, red dash : mean flame position.

2.3 Overview of Spatio/temporal Flame Response

We next discuss some general features of the spatio-temporal flame response to flow oscillations, summarizing results from the work of Shanbhogue *et al.* [33]. Figure 2.5 illustrates a typical image of the instantaneous edge of a flame forced by axial acoustic oscillations at a frequency, f_0. These acoustic fluctuations excite vortical disturbances whose influence on the flame is evident from the periodic wrinkles of the flame, quantified with the variable $\xi(x,t)$.

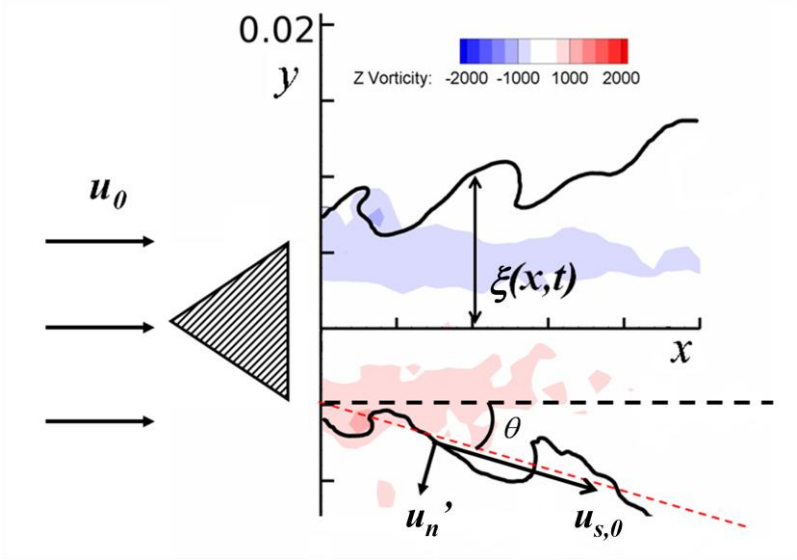

Figure 2.5. Instantaneous image of the flame front location (solid) and the underlying vorticity field [33] and corresponding coordinates.

The spatial distribution of the flame response is non-monotonic, as can be seen from typical measurements reproduced in Figure 2.6**,** which plots several spectra of the flame sheet location at different axial locations. This spectrum was determined from the Fourier transform of the flame front position, $\xi(x,t)$, indicated in Figure 2.5. The envelope of the flame response at $f=f_0$ is also drawn.

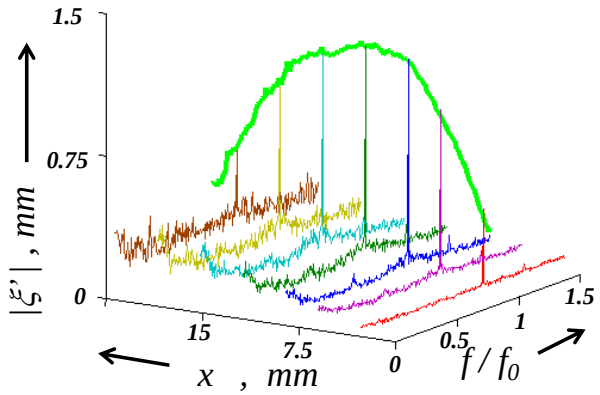

Figure 2.6. Dependence of the flame front fluctuation spectrum, $|\xi(x, f)|$ upon the axial location (f_0=300hz, u_0=4.5m/s, 9.5mm triangular bluff-body) [33] .

Figure 2.7a and Figure 2.7b plot other results at different operating conditions, focusing upon the flame response at the forcing frequency. From these plots, we can observe several generic features of the flame response, $|\xi(x, f_0)|$. First, $|\xi(x, f_0)|$starts near zero and grows monotonically with downstream distance. This near-flame holder behavior is controlled by flame anchoring. Shanbhogue showed that the slope of this rise, $\partial|\xi(x, f_0)|/\partial x$, is proportional to the magnitude of velocity forcing, indicating the flame response is linear in this region [34].

Next, the flame wrinkling amplitude exhibits a peak as in Figure 2.7b, or multiple peaks as in Figure 2.7a. This indicates that the flame response shows different behaviors by different flow conditions. Finally, the general trend for the magnitude of flame wrinkling is to decay with downstream distance. This decay length scale can be long or short relative to the interference length scale, as shown in Figure 2.7a and Figure 2.7b,

respectively. Especially, in Figure 2.7a, the decay does not scale with the magnitude of excitations, indicating nonlinear response of the flame.

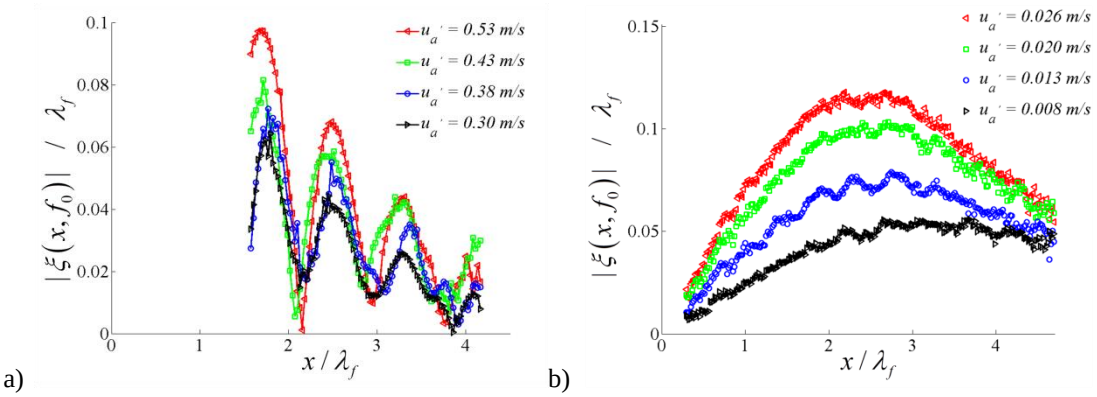

a) b)

Figure 2.7. Dependence of flame front fluctuation magnitude for circular bluff-body with 9.52mm diameter (a) 230hz, u_0=2.0m/s (b) 200hz, u_0=2.52m/s (u_a' represents acoustic forcingvelocity fluctuation upstream of bluff-body). Reproduced from Shanbhogue[34].

A complete description of the flame response to harmonic forcing requires capabilities to predict the flame wrinkling characteristics in regions of the flame controlled by flame anchoring, interference behavior, and flame wrinkle destruction, all of which will be addressed in this thesis.

2.4 Mechanisms Influencing Flame Kinematics

Mechanisms influencing the flame kinematic include kinematic restoration, flame stretch, and turbulent flow effect, which are reviewed in the followings.

2.4.1 Kinematic Restoration

Kinematic restoration refers to one of the dissipation mechanisms on the flame wrinkle through flame front propagation in its normal direction. This term is used in Peters' book where he states that the kinematic restoration acts as a sink term since the perturbed flame position will be restored to be smooth by the flame position [26].

For example, if we neglected the kinematic restoration term, the RHS of Eq. (2.4), the equation becomes a transport equation, with a velocity forcing. By further neglecting the axial velocities, Eq. (2.4) becomes:

$$\frac{\partial \xi}{\partial t} = u_y \tag{2.5}$$

This equation is Langevan's equation with the forcing term on the RHS. The solution for the random velocity term will be similar to the random walk. In this case, the variance of the flame speed will grow linearly with time. Therefore, without kinematic restoration, wrinkles will persist indefinitely.

A very well known manifestation of kinematic restoration is cusp formation as shown in Figure 2.8, where convex regions of the flame front become sharp edges. In the author's knowledge, the first appearance capturing cusps on flames is in Maxworthy's work, where he named it as *nodal shape* [35].

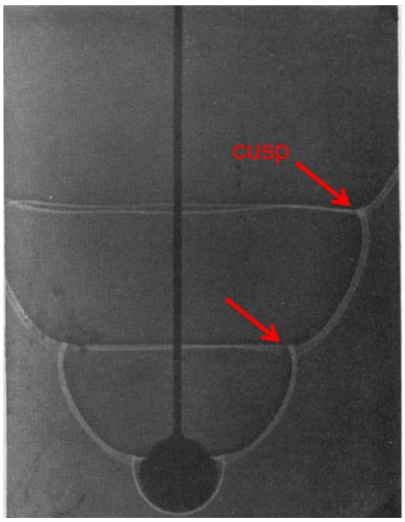

Figure 2.8. Development of cusps on the flame front for a bluff-body stabilized flame [35].

The first solution considering the kinematic restoration appeared in Petersen and Emmons's work where they referred to it as the Huygens' propagation [36]. In this paper, they evaluated the decrease of flame wrinkle height over the downstream distance as

shown in Figure 2.9. It was shown that the flame wrinkle height remains constant until it cusps, and then, the height starts to decrease further downstream. This trend was partially explained by Law and coworkers [37] where cusp formation time and its trace velocity were derived. Still, many dynamic behaviors of the flame front caused by the kinematic restoration are not well understood for combustion dynamics.

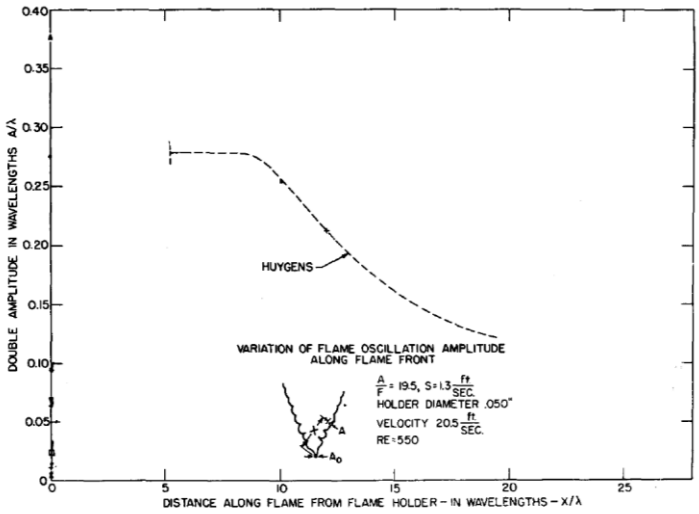

Figure 2.9. Dependency of the flame wrinkle height on the downstream distance assuming the Huygens's propagation of the initially sinusoidal flame front. Reproduced from Ref. [36].

2.4.2 Flame Stretch

The flame front kinematic equation, Eq. (2.3), seems quite simple. However, all complex chemistries and mass transports are buried in one parameter, S_L, the laminar flame speed. This laminar flame speed mainly depends on chemical processes and diffusive mass transport. However, the laminar flame speed depends on the flow parameters as well as flame geometry. For one dimensional flames, the flame speed is well understood [38] and many measurements show good agreements with models [39, 40]. However, as flames become multi-dimensional, chemical species and heat can

escape through transverse directions due to the finite thickness of the flame, leading to the flame speed varying a lot depending on flow/geometry conditions [41]. In order to model this effect, Williams related the change of the flame speed with a measure of the flame front distortion parameter, κ, defined as:

$$\kappa = \frac{1}{A}\frac{dA}{dt} \tag{2.6}$$

where, A is the surface area of an infinitesimal element of the flame front. Therefore, κ represents the logarithmic stretching/compressing rate of a surface area. This stretch rate, κ, can be decomposed into hydrodynamic and flame front curvature effects as [37]:

$$\kappa = \nabla_t \cdot \vec{u}_f + \left(\vec{u}_f \cdot \vec{n}\right) \cdot c \tag{2.7}$$

where ∇_t and c are the tangential derivative operator and twice the mean curvature, respectively. Two representative examples, illustrating the hydrodynamic strain and the curvature terms, are shown in Figure 2.10a and Figure 2.10b, respectively.

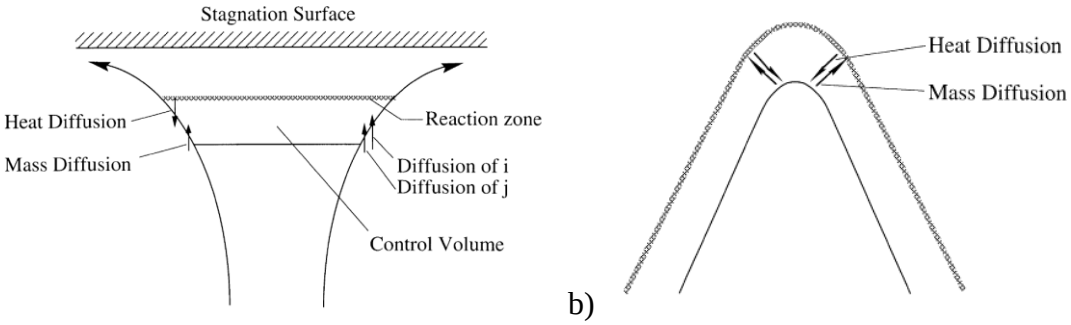

a) b)

Figure 2.10 Conceptual demonstration of stretched flames: a) a stagnation flame where hydrodynamic strain is present on the flame, b) a Bunsen flame tip where the curvature causes the flame stretch [37].

First, looking at the curvature effect, its linear dependency on the flame speed for weakly curved flames is related by the Markstein length, σ, as [37]:

$$\frac{S_L}{S_{L,0}} = 1 - \sigma \cdot c \tag{2.8}$$

However, this relationship is problematic for high curvature flames as the flame speed can reach negative values. Hence, Poinsot *et. al.* proposed a similar expression for the flame speed relationship [41], whose linear limit matches with Eq. (2.8) as:

$$\frac{S_L}{S_{L,0}} = \frac{1}{1 + \sigma \cdot c} \tag{2.9}$$

Measured dependencies of the flame curvature are shown in Figure 2.11 from a direct numerical simulation [42]. This data shows that as curvature deviate from zero, the flame speed lost linear dependency quickly; rather this measurement is similar to expression in Eq. (2.9).

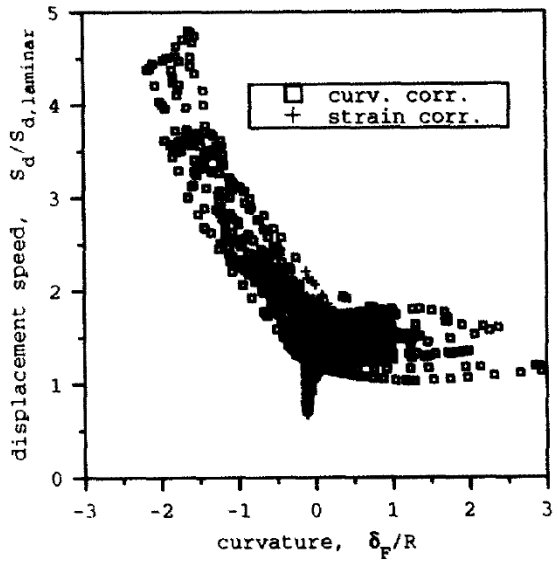

Figure 2.11 Correlation of the flame speed, S_L, at the flame reference location with respect to the local gas speed with curvature [42].

The next discussion is about the hydrodynamic strain rate dependency. Some common features regarding hydrodynamic strain rate can be found from Figure 2.12, where the flame speeds are calculated by CHEMKIN-PRO© with Davis and GRI 3.0 Mechanisms [43, 44]. The flame speed evaluation is performed on positively strained flames. From this figure, it is seen that the as the strain rate increases, the flame speed increases as well. The increases are steep near κ=0, however, the curves slightly bend down until the flames finally extinguish (the positions where each line stops represent the points of extinction).

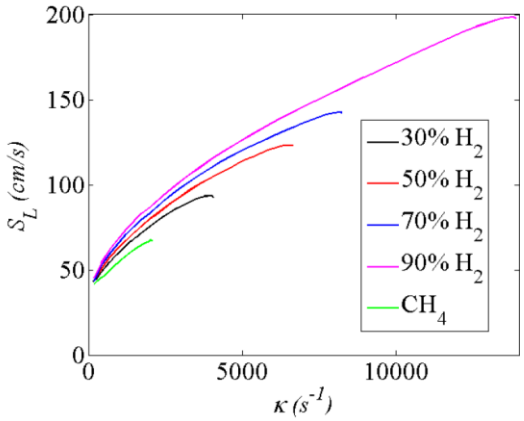

Figure 2.12 Calculated hydrodynamic strain sensitivity of H_2/CO mixtures (Calculation is done by opposed flames by CHEMKIN-PRO©) [45].

Prior studies related to flame dynamics have assumed that the burning velocity was constant [16], so that the flame speed is independent of the flow field. In reality, hydrodynamic strain and flame curvature introduced by the flow oscillations lead to perturbations in flame speed. In flames that are thermo-diffusively stable, these unsteady stretch effects act to smooth out the flame front corrugation. This causes the amplitude of the flame wrinkles to diminish as they propagate along the flame. As the radius of flame

wrinkling is approximately proportional to the inverse of the squared frequency, it can be anticipated that this effect grows in significance with frequency.

2.4.3 Turbulent Flames

Understanding of the dynamics of turbulent flames is crucial for combustion instability as most practical combustion systems operate under strong turbulent flows. Specifically, a study on turbulent flame speed, denoted as S_T, is one of the main research areas in turbulent combustion. Figure 2.13 shows some measurements and numerical calculations of the turbulent flame speed for different turbulent intensities. Lipatnikov and Chomiak summarized the recent development of studies of the turbulent flame speed in their paper [46]. They pointed out some of the common trends found on the turbulent flame speed: (1) an increase of S_T by increasing turbulent intensity, u', (2) an increase in S_T and dS_T/du' by the laminar burning velocity, and (3) an increase in S_T by pressure.

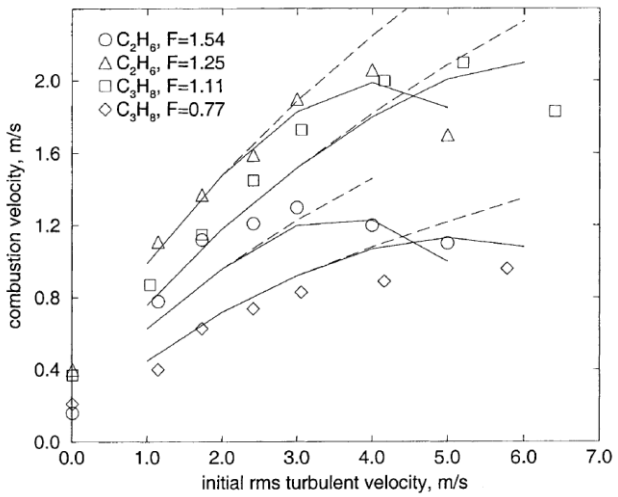

Figure 2.13. Dependencies of combustion velocities on turbulent intensity. Symbols show the experimental data of Karpov and Severin [47]. Solid and dashed curves have been computed with and without flamelet quenching submodel [48], repsectively.

It is also important to note that S_T is definition dependent. Extensive discussion of the advantages and disadvantages of various definitions are covered in the literature. Some resolution has been achieved in two recent reviews [49, 50] and through the International Workshop on Premixed Flames [51], where it is noted that there are actually multiple useful definitions for S_T that are relevant for different combustion issues (e.g., flashback and heat release rate). Four definitions of S_T have been proposed as local displacement speed, global displacement speed, local consumption speed, and global consumption speed.

There are also many efforts to obtain theoretical expressions for the turbulent flame speed. Clavin and Williams initiated the study on the turbulent flame speed using the *G*-equation and formulated an unclosed form solution [52]. Later, Aldredge and Williams calculated turbulent flame speeds for flat flames based on assumed isotropic turbulent flow [53]. Then, Aldredge extended his analysis with more general turbulent flows [29]. Creta and coworkers performed the numerical simulations solving Kuramoto-Sivashinsky equation [54] and G-equation [55] with prescribed turbulent flow to obtain effect of the turbulent velocity fluctuation on the flame propagation speed. Santosh and Lieuwen also performed analytical turbulent flame speed analysis for anchored flames [23]. They suggested that turbulent flame speed evolves from the flame holding points due to the tangential flow on the flame. This idea of an evolving turbulent flame from an initial state is consistent with a finding from spark-ignited spherical flames [46]. However, in these studies, they neglected the nonlinearities associated with kinematic restoration. Therefore, their solution shows that turbulent flame speed increases indefinitely with a positive integral time scale.

CHAPTER 3

G-EQUATION SOLUTION METHODS

The flame kinematic equation is a nonlinear partial differential equation rendering difficulties in obtaining analytic solutions. This chapter describes the methodology of solving the flame kinematic equation, a 3D version of Eq. (2.3) as:

$$\frac{\partial G}{\partial t} + \vec{u} \cdot \nabla G = S_L |\nabla G| \tag{3.1}$$

where, points satisfying $G(\vec{x}) = 0$ represent coordinates of flame positions. Then, the equation for the flame position, ξ, reproduced from Eq. (2.4) is:

$$\frac{\partial \xi}{\partial t} + u_x \frac{\partial \xi}{\partial x} - u_y + u_z \frac{\partial \xi}{\partial z} = S_L \sqrt{1 + \left(\frac{\partial \xi}{\partial x}\right)^2 + \left(\frac{\partial \xi}{\partial z}\right)^2} \tag{3.2}$$

While Eq. (3.1) can only be solved by numerical methods, Eq. (3.2) can be solved by various analytical methods as well as a numerical method. Analytic methods to be presented are the Hopf-Lax formula, the method of characteristics, and the perturbation methods. The Hopf-Lax formula and the method of characteristics render the exact solution for limited conditions. In contrast, the asymptotic method can be applied to many applications, but it provides an approximate solution. Still, this approximate solution is helpful in providing insight to the problems, and one can improve accuracy by keeping higher order of expansions if necessary. Lastly, numerical methods provide the exact solutions for wider range of applications, but the accuracy and domain size are limited.

3.1 Hopf-Lax Formula

The Hopf-Lax formula can give the exact explicit solution for limited cases. We will consider a class of problems where the flame propagates into a quiescent flow[i] with the given initial flame front.

$$u_x = u_y = 0, \quad \xi(x, t=0) = \xi_{init}(t) \tag{3.3}$$

In addition, we use $\xi = -\xi$ in this section to be consistent with the form used in Ref. [56]. Then, the governing equation for the flame position, Eq. (3.2), is rewritten as:

$$\frac{\partial \xi}{\partial t} = -S_L \sqrt{1 + \left(\frac{\partial \xi}{\partial x}\right)^2} \tag{3.4}$$

The Legendre transformation of the RHS of Eq. (3.4) is:

$$L(p) = \begin{cases} \infty & p < -S_L \\ -\sqrt{S_L{}^2 - p^2} & -S_L < p < S_L \\ \infty & S_L < p \end{cases} \tag{3.5}$$

Then, the general solution of Eq. (3.4) is described by the Hopf-Lax formula as [56]:

$$\xi(x,t) = \min_{x - S_L t < x^* < x + S_L t} \left(\xi_{init}(x^*) - \sqrt{(S_L t)^2 - (x - x^*)^2} \right) \tag{3.6}$$

Although the deriving steps and the solution seem quite complicated, the solution states a simple, well-known physical process. This solution simply states that the flame propagates in every radial direction from all points on flame fronts at the local displacement speed, S_L. Then, the new flame fronts become the set of outer most points from all circles. This process is also referred to as "Huygens propagation", see Ref. [57].

---

[i] In reality with flame wrinkles, moving flame induces a flow field ahead of it. So this assumption implicitly assumes a low density jump across the flame.

To illustrate, Figure 3.1 shows the instantaneous flame location at two instances of time, at $t=0$ and dt. The dashed lines indicate circles with radius, $S_L dt$, centered at points on the flame fronts at t=0. The flame position at later times can be drawn by connecting outer most points from all circles centered at the flame as shown in the figure. If the flame is curved, different points influenced new flame positions in different ways. For example, in the new flame fronts, less amounts originate from circles from concave region of old flame fronts (point B) than the convex region (point A). In the radical case, some concave region does not contributes at all to the new flame fronts (point D) as the new flame fronts are overshadowed by propagation from points C and E. In other word, the only convex region is important in determining the new flame fronts in the far later time. This also indicates that you cannot calculate back the initial flame front from the later flame front, which is called *irreversibility*.

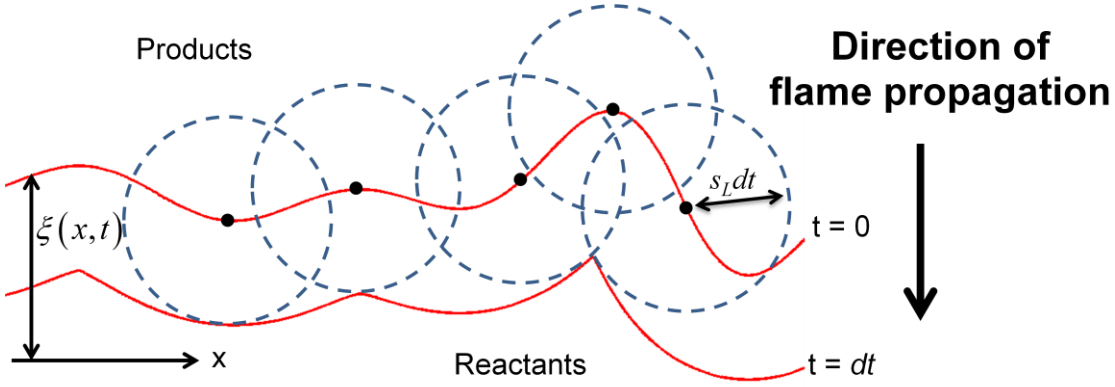

Figure 3.1 Sketch illustrating Huygens propagation and outer most flame fronts described by the Hopf-Lax solution for flame propagation.

3.2 Method of Characteristics

The method of characteristic is a powerful technique for solving nonlinear partial differential equations. Consider a example where the flame has an initial steady state

shape matching the given the flow condition, then suddenly the axial velocity changes from $u_{x,a}$ to $u_{x,b}$, which are described as:

$$u_y = 0, \quad u_x = \begin{cases} u_{x,a} & t < 0 \\ u_{x,b} & t \geq 0 \end{cases} \tag{3.7}$$

When the flame equilibrates at steady states, the two steady state solutions are obtained from Eq. (3.2) as:

$$\xi = \begin{cases} \dfrac{S_L}{\sqrt{u_{x,a}{}^2 - S_L{}^2}} \cdot x & t < 0 \\ \dfrac{S_L}{\sqrt{u_{x,b}{}^2 - S_L{}^2}} \cdot x & t >> 1 \end{cases} \tag{3.8}$$

The transient solution after t=0 can be obtained by the method of characteristics as followings. First, differentiate Eq. (3.2) with respect to x, and the equation becomes a special case of the more general equation as [58]:

$$\frac{\partial g}{\partial t} + c(g)\frac{\partial g}{\partial x} = 0 \tag{3.9}$$

where, $g = \partial\xi / \partial x$ and $c(g) = u_x - S_L \cdot g / \sqrt{1+g^2}$. The solution of this equation can be obtained by the method of characteristics. We will look at the case $u_{x,a} < u_{x,b}$ for illustration. The other case is solved in APPENDIX A. The characteristics are illustrated below:

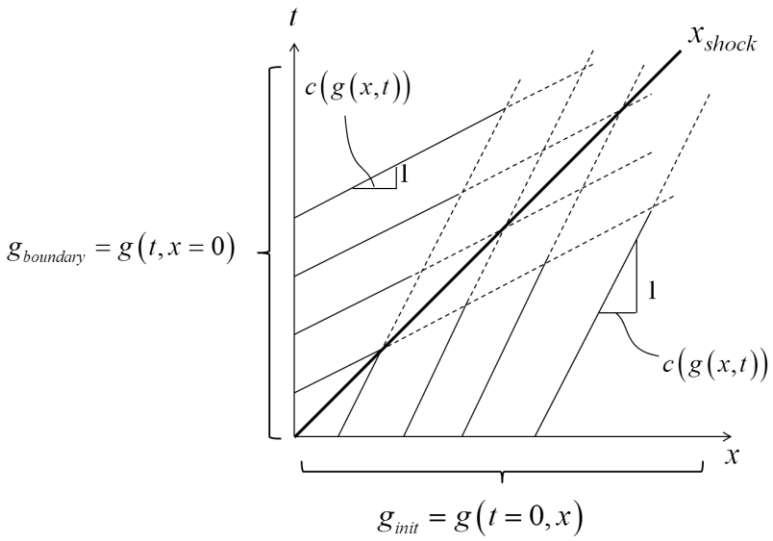

Figure 3.2 Illustration of space-time evolution of solution characteristics and formation of a shock.

Because $u_{x,a} < u_{x,b}$, the characteristic lines intersect and thus form "shocks". The "shock" location, x_{shock} can be obtained from the Rankine-Hugoniot jump condition [56] as following:

$$\frac{d\,x_{shock}}{dt} = \frac{F\left(g^{+}\right) - F\left(g^{-}\right)}{g^{+} - g^{-}} \tag{3.10}$$

where, *F(g)* is an indefinite integral of *c(g)*, i.e., $F(g) = u_{x,b}g - s_L\sqrt{1+g^2}$. Here, *F(g)* only uses $u_{x,b}$ because the axial velocity is $u_{x,b}$ during all calculation time. The values with superscript '+' and '-' represent the values before and after the jump, respectively. Then, it solves as:

$$c_{shock} = \frac{dx_{shock}}{dt} = \frac{{u_{x,b}}^2 - {S_L}^2 + \sqrt{\left({u_{x,b}}^2 - {S_L}^2\right)\cdot\left({u_{x,a}}^2 - {S_L}^2\right)}}{u_{x,a} + u_{x,b}} \tag{3.11}$$

Lastly, the solution becomes

$$g(x,t)=\begin{cases}\dfrac{S_L}{\sqrt{u_{x,b}{}^2-S_L{}^2}} & x\le c_{shock}\cdot t\\ \dfrac{S_L}{\sqrt{u_{x,a}{}^2-S_L{}^2}} & x>c_{shock}\cdot t\end{cases} \tag{3.12}$$

This example illustrates the use of methods of characteristics in solving dynamics of the flame front.

3.3 Asymptotic Analysis

Asymptotic analysis is popular methods to solve nonlinear partial differential equations as it is applicable to many applications. Fundamental idea behind the asymptotic analysis is based on the continuity of solutions over small parameters. For example, let's consider a small parameter ε. If we know a solution when ε=0, then the solution for nonzero ε can be approximated by the known solution, and the difference is proportional to the nonzero ε.

The procedure for our problem is followings. First decompose the input parameter into mean and perturbation. Here, we will impose small perturbation in the velocity field with perturbation amplitude of ε. For the convention, we use subscript '*0*' for unperturbed values and superscript prime as the perturbed values.

$$\begin{aligned}u(x,y,z,t)&=u_0(x,y,z)+\mu\cdot u'(x,y,z,t)\\ v(x,y,z,t)&=v_0(x,y,z)+\mu\cdot v'(x,y,z,t)\\ w(x,y,z,t)&=w_0(x,y,z)+\mu\cdot w'(x,y,z,t)\end{aligned} \tag{3.13}$$

Next, we consider both the linear and nonlinear response character of the flame. Hence, ξ, is written as:

$$\xi(x,t)=\xi_0(x)+\varepsilon\cdot\xi'(x,t)+O(\varepsilon^2) \tag{3.14}$$

By expanding the solution in powers of ε [59], the zeroth order equation for the flame fluctuation is written as follows :

$$u_0 \frac{d\xi_0}{dx} - v_0 = S_L \sqrt{1 + \left(\frac{d\xi_0}{dx}\right)^2} \tag{3.15}$$

The general solution of the zeroth order solution can be obtained by solving the following ordinary differential equation.

$$\frac{d\xi_0}{dx} = \frac{u_0 v_0 \pm S_L \sqrt{u_0^2 + v_0^2 - s_L^2}}{u_0^2 - S_L^2} \tag{3.16}$$

The solutions for Eq. (3.16) are geometrically illustrated in Figure 3.3. Given the mean flow velocities, the flame propagation with S_L should be perpendicular to the mean flame position. Therefore, we can draw a circle centered at end point of the mean flow vector with a radius of S_L. Then, draw tangent line to the circle in dashed line. The solution in Eq. (3.16) as well as the drawing in Figure 3.3 shows two possible slopes of the mean flame position. The uniqueness of the solution can be obtained once the location of the reactants is known. For example, if the reactants are on the top side, the mean flame position becomes *Flame 1* as the flame should propagate into the top direction and vice versa. Also, note that for *Flame 1*, as v_0 increases, the flame becomes more vertical (i.e. flame will be more perpendicular to the axial direction), and as u_0 increases, the flame becomes horizontal.

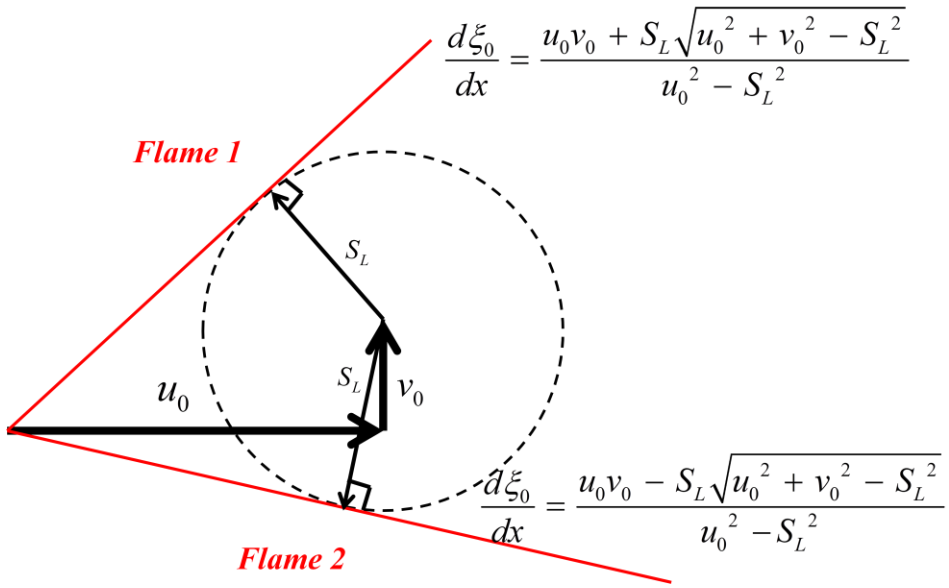

Figure 3.3 Geometric illustration of possible mean flame positions for given mean velocities.

Next consider the first order equation. Inserting this expansion into Eq. (3.2) and retaining only the first order terms leads to:

$$\frac{\partial \xi_1}{\partial t} + \underbrace{\left(u_{x,0} - S_{L,0} \cdot \frac{\partial \xi_0 / \partial x}{\sqrt{1 + \left(\partial \xi_0 / \partial x\right)^2}} \right)}_{u_{s,0} \cdot \cos\theta} \cdot \frac{\partial \xi_1}{\partial x} = \underbrace{-u_{x,1} \frac{\partial \xi_0}{\partial x} + u_{y,1} + S_{L,1}\sqrt{1 + \left(\partial \xi_0 / \partial x\right)^2}}_{\left(-u_{n,1} + S_{L,1}\right)/\cos\theta} \quad (3.17)$$

where, $d\xi_0/dx$ are obtained by eq. (3.16), and new parameters are illustrated in Figure 3.4.

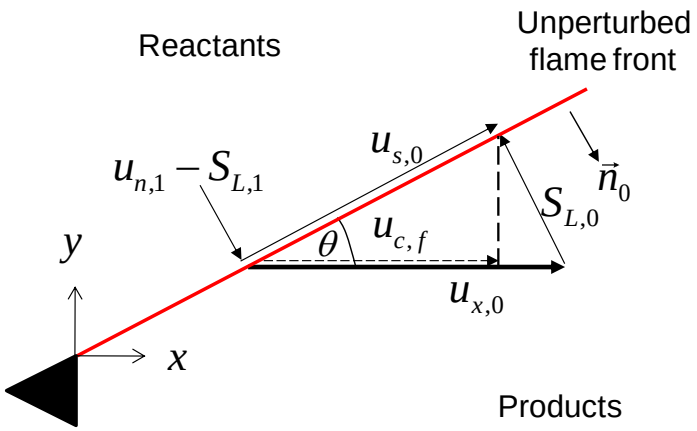

Figure 3.4 An illustration of the top half of an attached flame, indicating the velocity components tangential and normal to the flame. Reproduced from [27].

If $d\xi_0/dx$ is substituted with $1/\tan\theta$, Eq. (3.17) can be rewritten as:

$$\frac{\partial \xi_1}{\partial t} + u_{s,0}\cos\theta \cdot \frac{\partial \xi_1}{\partial x} = \frac{v_{F,n1}}{\cos\theta} \tag{3.18}$$

where $v'_{F,n1}$ and $u_{s,0}$ denote a fluctuation of normal component to the flame ($-u_{n,1} + S_{L,1}$) and a mean velocity in the tangential direction of the flame, respectively. Note that it is a sub-class of the more general equation of

$$\frac{\partial \xi_1}{\partial t} + \alpha \frac{\partial \xi_1}{\partial x} = f(x,t) \tag{3.19}$$

The flame position at a given (x_s, t_s) is a superposition of wrinkles from upstream points that were generated at earlier times and have propagated along the flame front at the velocity, $u_{s,0}\cos\theta$. This can be seen from the solution of Eq. (3.17). To simplify the presentation, we assume that the mean velocity field is spatially uniform. Assuming a flame position boundary condition at $x = 0$, $\xi(x=0,t) = \xi_b(t)$, the general solution of the G-equation is:

$$\xi_1(y_s, t_s) = \xi_b\left(t_s - \frac{x_s}{u_{s,0}\cos\theta}\right) + \frac{1}{u_{s,0}\cos\theta}\int_0^{x_s} \frac{1}{\cos\theta} v_{F,n1}\left(\chi,\, t_s - \frac{x_s - \chi}{u_{s,0}\cos\theta}\right) d\chi \tag{3.20}$$

This solution shows that the flame response at each spatial position and time is a superposition of two waves that propagate along the flame front. The first wave, denoted as the "Homogeneous part" is excited at the flame anchoring point and propagates along the flame sheet at an axial velocity of $u_{s,0}\cos\theta$, together with what was already presented by the boundary condition. The second wave propagates at the excitation phase velocity. Note that the particular solution is a convolution of the velocity at all points upstream of *x* while the homogeneous solution is only influenced by the velocity field near the attachment point. The spatial variation in amplitude and phase of these two solutions leads to interesting interference phenomenon, as will be described later.

3.4 Numerical Methods

3.4.1 The Kinematic Equation for the Flame Position, ξ

For the fully nonlinear solutions, Eq. (3.2) can be obtained by numerical calculation. Spatial derivatives are discretized using a Weighted Essentially Non-Oscillatory (WENO) [60] scheme designed for Hamilton-Jacobi equations. This scheme is uniformly fifth order accurate in regions where the spatial gradients are smooth and third order accurate in discontinuous regions. Derivatives at the boundary nodes are calculated using fifth order accurate upwind-differencing schemes so that only the nodes inside the computational domain were utilized. A Total Variation Diminishing (TVD) Runge-Kutta scheme [61], up to third order accurate, was used for time integration and Local Lax-Friedrich (LLF) scheme, which is detailed in APPENDIX B, was used for improved stability [60]. The spatial and temporal grid size were $\lambda_0/100$ and $1/(10{,}000f_0)$, respectively.

3.4.2 Level Set Method

This section describes the computational approach used to solve the level-set equation in Eq. (6.1). These computations closely follow previously reported work which are detailed in Sethian and Osher [62, 63], and by Hemchandra and Lieuwen [64] for this particular application. The level set equation is solved using the semi-Lagrangian Courant–Isaacson–Rees scheme together with the back and forth error compensation and correction (BFECC) technique [65]. This is a second order scheme with low numerical dissipation and dispersion errors. The local level-set method is adopted to achieve significant reduction in computation time [66]. The level-set field is reset to a signed distance function by solving an auxiliary re-distancing equation using the prescription of Dupont and Liu [65].

The computational domain consists of 201x201x801 grid cells with a spatial resolution of $(u_{s,0}/f_0)/100$, $L_{11}/10$, and the time step of $1/1000f_0$. Several grid convergence studies were performed. First, a grid study was performed for a laminar case with the baseline and factor of ten increased grid density, showing less than a 1% difference in flame position at $s/\left(u_{s,0}/\omega_0\right)$=25. A similar comparison of calculations using the baseline and factor of two increased density for 7% turbulent intensity case showed a 3% difference in ensemble averaged flame position at $x/\left(u_{x,0}/\omega_0\right)$=15.

The instantaneous flame position is evaluated numerically from the level set field using numerical approximations for the Heaviside function [63] and the delta function [67]. The numerical results are then phase-averaged over 160 ensembles to produce one time series in the forcing period.

In order to compare these computations with analytical results, it is necessary to calculate the ensemble averaged flame positions, $\left\langle \tilde{\xi} \right\rangle$. At lower turbulence intensities, the instantaneous flame position is a single valued function of (s,z) for the majority of time instants; e.g., the flame is multi-valued in less than 1% of realizations for $u'/u_{s,0} = 0.07$. However, the occurrence of multi-valuedness increases significantly with increasing turbulent intensity (e.g., see Figure 3.5); e.g., in about 25% of the realizations for $u'/u_{s,0} = 0.34$.

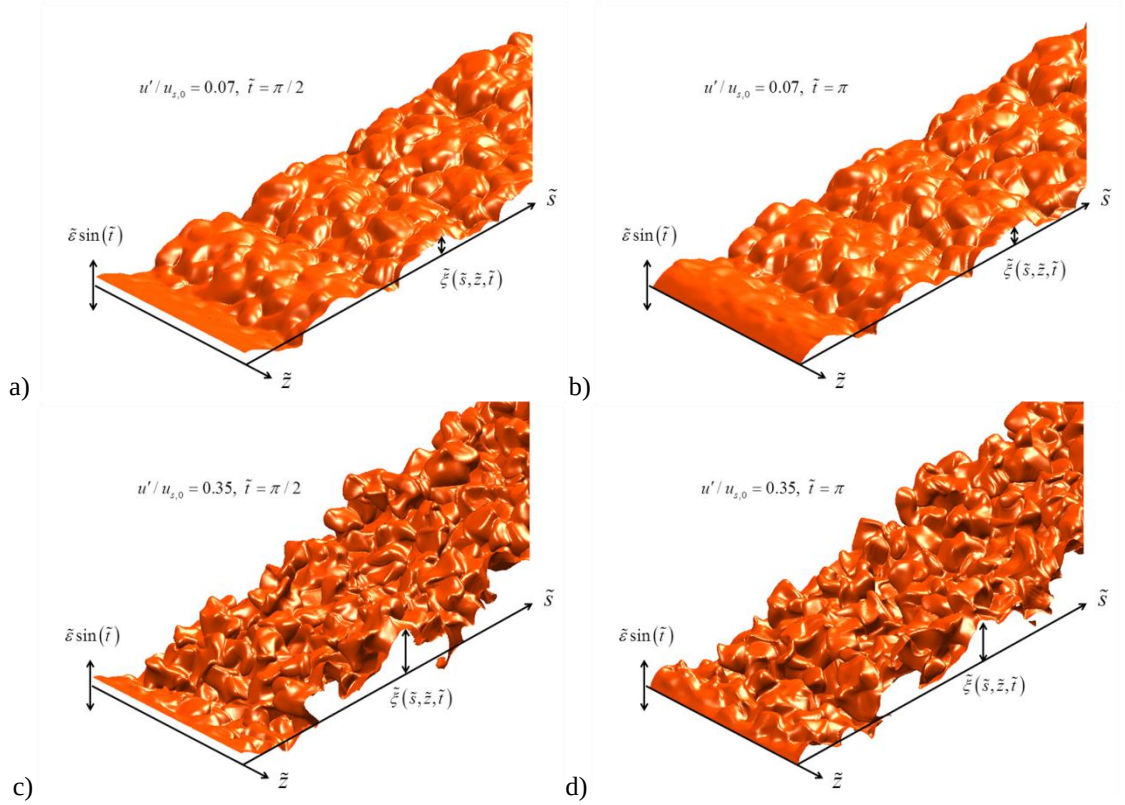

Figure 3.5. Instantaneous realizations of the flame sheet extracted from solution of full level set equation, Eq. (6.1). a,b) $u'/u_{s,0}$**=0.07, c,d)** $u'/u_{s,0}$**=0.35 (**$S_L/u_{s,0}$**=0.25,** $\varepsilon/\left(u_{s,0}/\omega_0\right)$**=0.65,** $L_{11}/\left(u_{s,0}/\omega_0\right)$**= 0.65).**

3.4.2.1 Applying Moving Flame Holder in Uniform Grid

This subsection describes the numerical implementation on specifying the boundary conditions of the level set equation, when grid points do not align with the boundaries. Figure 3.6 shows the schematics of the flame position at an instance where the top side is reactant and bottom side is product. Flame holder, marked in the solid black circle, is oscillating on a thick solid line. A sample flame front is marked in a solid red line, which starts from the flame holder and extends further to the right direction.

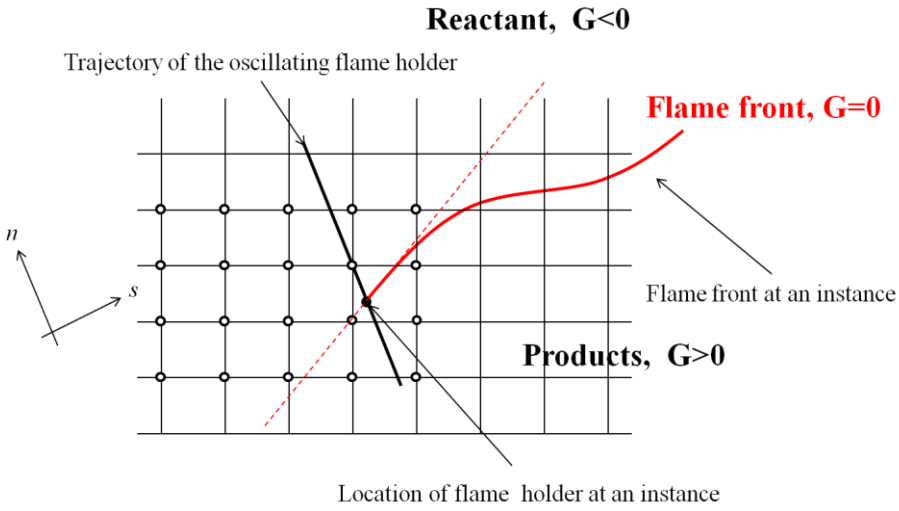

Figure 3.6. Schematic of the motion of the flame holder in the uniform grid. A solid red line is the flame front, and a dashed redline is a tangent of the flame front at the flame holder.

As the flame holder location is not on the grid, we need to specify level set values in the neighboring grid points. As seen from Figure 3.6, we need to know the tangent of the flame position (a red dashed line in Figure 3.6) so that we put positive values on reactant side and positive values on product side. Furthermore, once the tangent line is determined, neighboring values are determined from bilinear interpolation [68]. Note that s and n coordinates are chosen to align with the flame tangential and normal direction in this example (i.e., θ=0 in Eq. (3.18)). Then Eq. (3.18) is rewritten as:

$$\frac{\partial \xi_1(s,t)}{\partial t} + u_{s,0}\frac{\partial \xi_1(s,t)}{\partial s} = u_{n,1} \tag{3.21}$$

Therefore, the initial slope in the normal-tangential coordinate system, it is obtained as:

$$\frac{\partial \xi_1(s,t)}{\partial s} = \frac{u_{n,1} - \partial \xi_b / \partial t}{u_{s,0}} \tag{3.22}$$

Then, based on this slope, the neighboring points marked in the empty circle are prescribed at each time before the computation.

3.4.2.2 Determination of Flame Position from Level Set Field

The level set simulation gives outputs as the level set values in the uniform grid. Two difficulties arise from evaluating the flame position from the given level set field. The first difficulty is the misalignment of the grid directions and the desired flame coordinate. Grid direction aligns with the mean flow direction (for the easy of flow field implementation), but the flame coordinates aligns with the flame tangential/normal directions. As shown in Figure 3.6, the flame position is measured in the y-direction. Therefore, simply marching in one direction and find a value where the level set value becomes zero is not trivial.

The second difficulty is multi-valued flame position (i.e., for one *n*-direction, there are multiple flame fronts). There are several choices. The first choice is using the average of progress variables for the turbulent flame [27]. First, binarize the *G* field into progress variable space, $\tilde{c}$, defined as:

$$\tilde{c}(x,y,z) = \begin{cases} 1 & \text{if } G(x,y,z) > 0 \quad \textit{i.e., product side} \\ 0 & \text{if } G(x,y,z) < 0 \quad \textit{i.e., reactant side} \end{cases} \tag{3.23}$$

Then, take ensemble average over many realizations, and obtain the contour satisfying $\tilde{c}$ =0.5 for the representative flame position. However, this definition of progress variable contour 0.5 is different definition of the mean of the flame position. APPENDIX D shows that the progress variable contour 0.5 represents the median of the

flame position while conventional definition of the flame position is the mean of the flame position for the single valued flame. However, this median of the flame position is hard to express by the flame position kinematic equation.

The third choice, which we chose to use, is using average of the multiple flame position at every instant. Then the flame position is evaluated by integrating the product of *y*, delta function and Heaviside function in the domain as:

$$\xi = \frac{1}{W} \frac{\int_{W\times\infty} y \cdot \delta(G) H(G) dx}{\int_{W\times\infty} \delta(G) H(G) dx} \tag{3.24}$$

Therefore, the flame position is the average of the flame position over the *x*-domain of width *W*. In order to integrate with in the specified region, the 3D delta function is from Ref. [67], and the numerical heaviside function [62] is:

$$H(G) = \begin{cases} 0 & G < -dx \\ \frac{1}{2}\left(1 + \frac{G}{\varepsilon_H} + \frac{1}{\pi}\sin\left(\pi \frac{G}{\varepsilon_H}\right)\right) & -dx < G < dx \\ 1 & dx < G \end{cases} \tag{3.25}$$

where, *dx* is the grid size. In addition, if the flame position is multi-valued, Eq. (3.24) will provide the area weighted mean flame position of the multiple locations (the 3D delta function itself is an area weighted function).

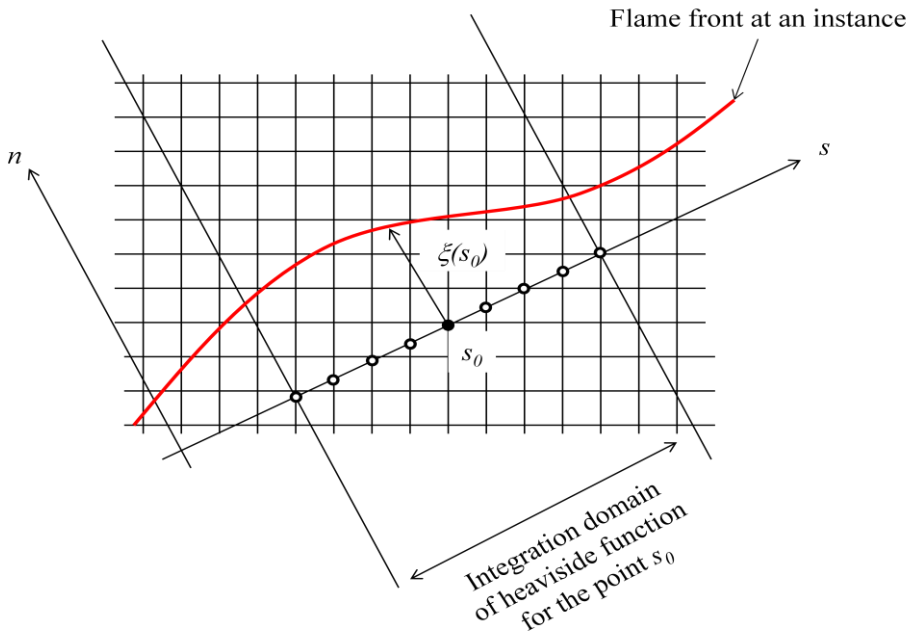

Figure 3.7 The schematics of integration domain in order to evaluate the flame position and the local surface area at s_0.

3.4.2.3 Progress Variable and Mean Flame Position

Different approaches can be used to specify the ensemble averaged flame position in these cases. One approach is to turn each realization into a field of binarized values, with zero and unity denoting reactants and products, respectively. These fields can then be averaged and the ensemble averaged value associated with some progress variable, $\widehat{C}$, such as $\langle \widehat{C} \rangle$ =0.5 as [49]:

$$\widehat{C} = \begin{cases} 1 & \text{in the product side} \\ 0 & \text{in the reactant side} \end{cases} \tag{C26}$$

This is a fairly standard way in which ensemble averaged flame characteristics are presented in experimental turbulent combustion studies. The problem with this binarization approach, however, is that it is a nonlinear operation. Consequently, even

for a single valued flame front, the $\langle \widehat{C} \rangle$=0.5 iso-contour describes the median as shown in APPENDIX D, not the mean, of the flame position. However, the asymptotic analysis quantifies the mean, so the two calculations approaches cannot be quantitatively compared. Therefore, we did not utilize this progress variable approach. Rather, we extracted the instantaneous flame position coordinates and defined $\langle \tilde{\xi} \rangle$ as the average of each transverse value at a given axial location. This result leads to a consistent comparison approach for single valued flames where the asymptotic analysis can be performed. Practically speaking, the difference between the two calculation approaches does not appear to be significant, as Figure 3.8 compares the $\langle \widehat{C} \rangle$=0.5 iso-contour and $\langle \tilde{\xi} \rangle$ for a typical case showing that they are nearly identical. Figure 3.8 shows the comparison of the ensemble average of the flame position and 0.5-contour of ensemble-averaged progress variable. The maximum difference, which occurs at trailing edge of the flame in the far field, was 5% of the harmonic excitation ($\tilde{\varepsilon}$).

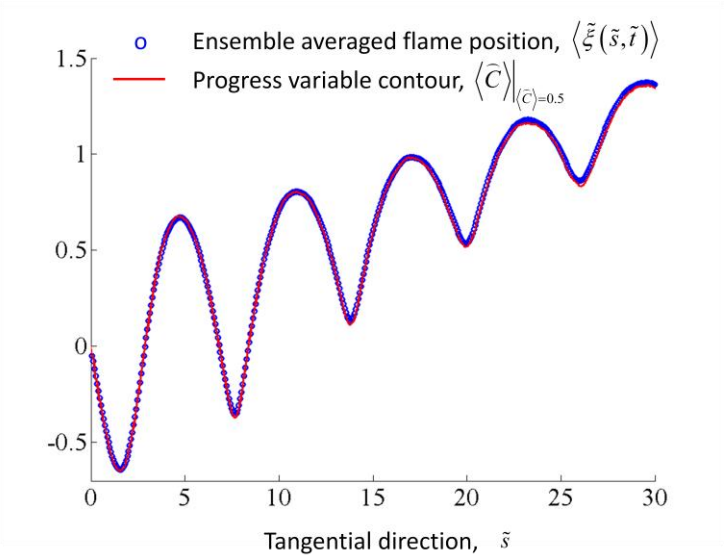

Figure 3.8. Comparison of ensemble average of instantaneous flame position and progress variable contour of 0.5 at one phase of the forcing period ($\tilde{t}$ =0). (Conditions are $\tilde{\varepsilon}$ =0.65, $\tilde{\mu}$ =0.04, $\tilde{S}_L$ =0.25, and $\tilde{L}_{11}$ =0.65).

3.4.2.4 Prescribed Turbulent Velocity

In order to be consistent with the theoretical analysis, the velocity field in the current computations in prescribed rather than solved for. This is done for two reasons. Firstly, the aim is to compare the numerical solution with the linear theoretical solutions in order to study the effect of non-linearity on the non-local nature of the flame response. Secondly, physical processes controlling the flame response are independent of how the turbulence field was generated. Hence the computationally cheaper approach of specifying the velocity field has been adopted so that a larger parametric space could be explored.

The prescribed turbulent velocities also closely follows Hemchandra's approach, which are detailed in his thesis [69]. The turbulent velocities fields are incompressible and isotropic. The longitudinal correlation function is specified as [70]:

$$R_{11}(r) = \exp\left(-\frac{\pi}{4}\frac{r^2}{L_{11}^{\ 2}}\right) \tag{3.27}$$

where, L_{11} is the longitudinal integral length scale and r is the spatial separation between two points for which the correlation is sought. The above correlation function is representative of that of low intensity large scale turbulence. Such correlation functions have been used in the prior analyses of local consumption speed of freely propagating flame flames of Aldredge et al. [53] and Creta et al. [54]. Assuming spatial isotropy, the energy spectrum function corresponding to the above correlation function is:

$$E(k) = \frac{4L_{11}}{\pi^3} {u_{rms}}^2 (kL_{11})^4 \exp\left(-\frac{(kL_{11})^2}{\pi}\right) \tag{3.28}$$

Lastly, this turbulent flow fluctuation is convected downstream with the mean flow, the Taylor's hypothesis. These hypothesis enables us to relate the time correlation with space correlations, which are derived in APPENDIX H.

CHAPTER 4

FLAME WRINKLE EXCITATION PROCESSES – BASIC CONSIDERATIONS

This chapter describes the excitation of the flame response for the nominally 2D/axisymmetric flame. The flame front can be excited through unsteady motion of the flame base, or it can be continuously perturbed by field disturbances such as velocity or fuel/air ratio fluctuations. The analysis in this chapter is limited to the linear regime. Nonlinearities and wrinkle decay mechanisms will be covered in the following chapters. The first section presents the general analysis of the flame response and provides an explicit form for the unsteady flame position. Then, three specific model problems will be examined along with experimental validation. The first problem deals with a flame which is excited through the oscillating flame holder in a steady flow. In the second and third problems, the flame base is set to be fixed, and the flame is excited by harmonic and broadband velocity disturbances, respectively. It is shown that the unsteady flame base motion propagates with a velocity equal to the tangential velocity and its oscillation magnitude remains constant in the subsequent region. Furthermore, among the field disturbances, it is the normal components acting on the normal direction which disturbs the flame front position. For the harmonic disturbance or the broadband velocity disturbances, the flame response increase linearly downstream in the near field.

4.1 Linear Flame Response

The investigated configuration is a nominally 2D flame[ii] as shown in Figure 4.1. The coordinate system is also drawn. The 2D surface in Figure 4.1 is the flame front separating reactants (top region) and products (bottom region). The position of the flame front, denoted as ξ, is assumed to be a single valued function of x, z and t. This single valued assumption may break down for highly wrinkled flames, such as vortex driven flames or strong turbulent flames. For small disturbance, however, the flame front remains single valued [34], which enables to track the problem analytically.

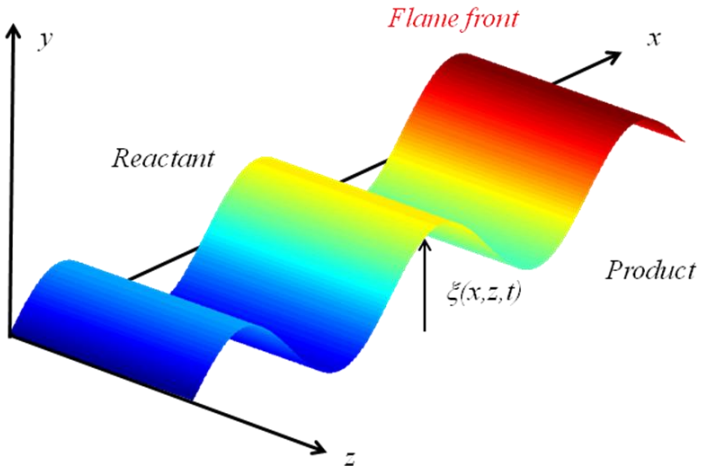

Figure 4.1. An illustration of a nominally 2D flame and its coordinate system. The position of the surface, or the flame front, is denoted as ξ.

For this configuration, the kinematic equation for the flame position, ξ, is (a repetition of Eq. (3.2) for convenience):

[ii] The nominally 2D flame denotes the flame which is 2D in the absence of any disturbance. However, the nominally 2D flame becomes 3D if any of disturbance is 3D.

$$\frac{\partial \xi}{\partial t} + u_x \frac{\partial \xi}{\partial x} - u_y + u_z \frac{\partial \xi}{\partial z} = S_L \sqrt{1 + \left(\frac{\partial \xi}{\partial x}\right)^2 + \left(\frac{\partial \xi}{\partial z}\right)^2} \tag{4.1}$$

Equation (4.1) is a nonlinear partial differential equation (PDE), which is difficult to solve analytically. Alternatively, asymptotic analysis can be applied to convert the nonlinear PDE into a series of linear PDEs, which give the approximate solutions for small fluctuations of the flame position. In performing the asymptotic analysis, we first expand the flame position, the flame speed and the velocity as sums of mean and fluctuation components as (see Sec. 3.3):

$$\begin{aligned} \xi &= \xi_0(x,z) + \xi_1(x,z,t) \\ S_L &= S_{L,0}(x,z) + S_{L,1}(x,z,t) \\ \vec{u} &= \vec{u}_0(x,z) + \vec{u}_1(x,z,t) \end{aligned} \tag{4.2}$$

Inserting these expansions into Eq. (4.1) and retaining only the linear terms lead to:

$$\begin{aligned} \frac{\partial \xi_1}{\partial t} + \left(u_{x,0} - S_{L,0}\frac{1}{N}\frac{\partial \xi_0}{\partial x}\right)\frac{\partial \xi_1}{\partial x} + \left(u_{z,0} - S_{L,0}\frac{1}{N}\frac{\partial \xi_0}{\partial z}\right)\frac{\partial \xi_1}{\partial z} \\ = -u_{x,1}\frac{\partial \xi_0}{\partial x} - u_{z,1}\frac{\partial \xi_0}{\partial z} + u_{y,1} + S_{L,1}N \end{aligned} \tag{4.3}$$

where, $N = \sqrt{(\partial \xi_0 / \partial x)^2 + (\partial \xi_0 / \partial z)^2 + 1}$. This equation can be simplified in terms of the flame normal vector ($\vec{n}_0$), the tangential velocity ($\vec{u}_s$), and the normal velocity ($\vec{u}_n$), which are defined respectively as:

$$\vec{n}_0 = \frac{1}{N}\left(\frac{\partial \xi_0}{\partial x}\vec{e}_x - \vec{e}_y + \frac{\partial \xi_0}{\partial z}\vec{e}_z\right),\ \vec{u}_{s,0} = \vec{u}_0 - s_{d,0}\vec{n}_0,\ \ \textit{and}\ \ u_{n,1} = \vec{u}_1 \cdot \vec{n}_0 \tag{4.4}$$

Note that the flame normal vector, $\vec{n}_0$, is chosen to point into the products as shown in Figure 4.2. For the 2D flame, those velocity components are depicted in Figure 4.2 for reference. The simplified form of Eq. (4.3) is then:

$$\frac{\partial \xi_1}{\partial t} + \vec{u}_{s,0} \cdot \nabla \xi_1 = N \cdot v_{F,n1} \tag{4.5}$$

where,

$$v_{F,n1} = -u_{n,1} + s_{d,1} \tag{4.6}$$

This equation shows that the linearized kinematic equation is a convective equation with a forcing term. The convective operator on the LHS of Eq. (4.5) indicates that the flame wrinkle propagates in the tangential direction, while the RHS of Eq. (4.5) shows that the flame is perturbed by the normal component of the velocity disturbance and the flame speed disturbance. Note that flame speed and the velocity disturbances can be lumped as $v_{F,n1}$.

Furthermore, if the flame is assumed to be 2D/axisymmetric, then Eq. (4.5) can be further simplified in physically more revealing form. After using the identities, $\tan\theta = \partial\xi_0 / \partial x$ and $N = 1/\cos\theta$ (see Figure 4.2 for θ), Eq. (4.5) is rewritten as:

$$\frac{\partial \xi_1}{\partial t} + u_{s,0}\cos\theta \frac{\partial \xi_1}{\partial x} = \frac{v_{F,n1}}{\cos\theta} \tag{4.7}$$

where, $u_{s,0} = \left|\vec{u}_{s,0}\right|$. The velocity, $u_{s,0}$, represents the mean tangential velocity along the flame while $u_{n,1}$ denotes the fluctuating velocity component in the direction normal to the unperturbed flame front. The $\cos\theta$ term on both sides comes from the choice of the flame position coordinate; i.e., if ξ is written instead as a function of vertical coordinate *y*, then $\sin\theta$ arises. Alternatively, if the coordinate system is aligned with the unperturbed flame position (tangential direction), this term does not appear at all. This propagation speed is equal to the *x*-component of the mean flow velocity in the tangential direction along the flame, $u_{c,f}$, as illustrated in Figure 4.2.

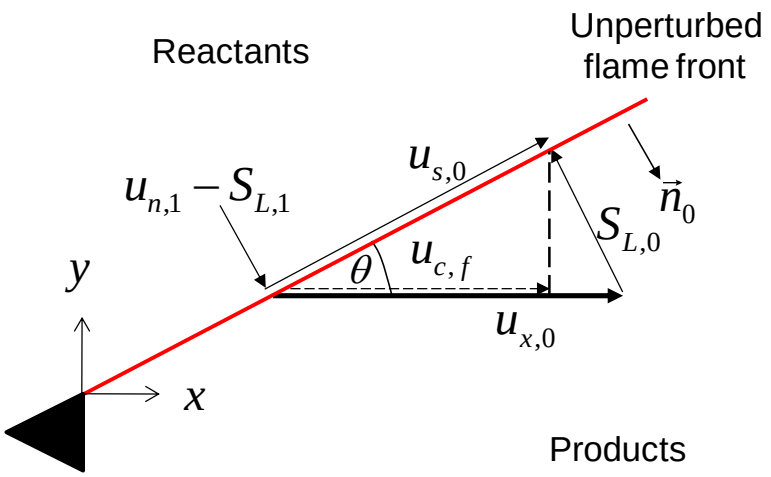

Figure 4.2 An illustration of the top half of an attached flame, indicating the velocity components tangential and normal to the flame. Reproduced from [27].

4.1.1 Generic Solution for the Linearized Equation

This section describes the linearized dynamics of flames with tangential flow, i.e., flows where $u_{s,0}$ is not equal to zero, and illustrates the effects of flame attachment, flow forcing, and advection processes on the flame response. Note that in the absence of tangential flow the linearized flame dynamics are described by Langevin's equation, which is an ordinary differential equation. In this case, the unsteady flame motion at each point is a function of the local disturbance field, $v_{F,n1}$. In contrast, flame dynamics with tangential flow are described by a partial differential equation, usually introducing an additional spatial boundary condition to the problem and making the local flame position a non-local function of the disturbance field.

In addition, we will drop the *z*-dependency on the flame response (2D assumption) until the last section. This assumption simplifies the analysis and provides the physical insight in understanding the flame kinematics. We will come back with 3D consideration in the last section, where we deal with the turbulent disturbance. Until then, flame response is a function of *x* and *t*.

The flame position at a given (x,t) is a superposition of wrinkles from all upstream points that were generated at earlier times and have propagated along the flame front at the velocity $u_{s,0}$. This can be seen from the solution of Eq. (4.7). To simplify the presentation, we assume that the mean velocity field is spatially uniform. Assuming the flame boundary condition of $\xi(x=0,t)=\xi_b(t)$ and the flow disturbance of $v_{F,n1}(x,t)$, the general solution of the ξ-equation is:

$$\xi_1(x,t)=\xi_b\left(t-\frac{x}{u_{s,0}\cos\theta}\right)+\frac{1}{u_{s,0}\cos\theta}\int_0^x\frac{1}{\cos\theta}v_{F,n1}\left(\chi,\,t-\frac{x-\chi}{u_{s,0}\cos\theta}\right)d\chi \quad (4.8)$$

Specific examples will be further examined in the following sections.

4.2 Example 1: Flame Excitation by the Unsteady Flame Base Motion

The first example considers the oscillating flame holder in a uniform steady flow. This example simulates the experiments by Petersen and Emmons[iii] [36]. The boundary and flow conditions are:

$$\xi_1(x=0,t)=\xi_b(t),\quad \vec{u}=u_{x,0}\vec{e}_x \quad (4.9)$$

The linear solution of this example is deduced from Eq. (4.8), which is:

$$\xi_1(x,t)=\xi_b\left(t-\frac{x}{u_{s,0}\cos\theta}\right) \quad (4.10)$$

[iii] However, in the experiments, the steady flow condition cannot be achieved because the oscillating flame holder induced velocity fluctuations. Those effects can be minimized by using small flame holder.

If the flame base motion is harmonic, such as $\xi_b(t) = \varepsilon \cdot \cos(\omega_0 t)$, then the gain and the phase of the flame position at the frequency, ω_0 are:

$$Gain: |\xi_1(x, \omega_0)| = \varepsilon \tag{4.11}$$

$$Phase: \angle\xi_1(x, \omega_0) = -2\pi x / (u_{s,0} \cos\theta) \tag{4.12}$$

These results indicate that the gain, or equivalently the magnitude of the oscillation, remains constant over the downstream distance while the phase decrease linearly with a slope of $2\pi / (u_{s,0} \cos\theta)$. These phase result physically represents that the shape of the flame front convects downstream with a velocity of $u_{s,0} \cos\theta$.

The magnitude of the flame position oscillation was measured by Petersen and Emmons [36]. Note that the magnitude they measured is not exactly the gain of the flame response at the forcing frequency; rather it is the peak-to-peak amplitude within which the flame position fluctuates (i.e., the total variation). Figure 4.3 depicts the evolution of the flame front magnitude over the downstream distance. The dashed line is the theoretical estimation, including nonlinearities associated with kinematic restoration if the flame wrinkle is perfectly sinusoidal. This dashed line is initially flat because the peak-to-peak amplitude remains the same until the flame front develops cups [35]. Then, by kinematic restoration processes, the peak-to-peak amplitude will decrease subsequently [26]. This decrease of the total variation due to the kinematic restoration is not covered in this chapter; rather it will be covered in CHAPTER 5 and CHAPTER 7 in more detail.

The solution in Eq. (4.10) indicates that the flame response remains constant. However, in reality nonlinear and additional disturbance field will cause the change of the oscillation magnitude in the real flame. However, the results with symbol * in Figure 4.3 shows that the flame wrinkle maintains quite constant magnitude for some downstream distance because of its small nonlinearity.

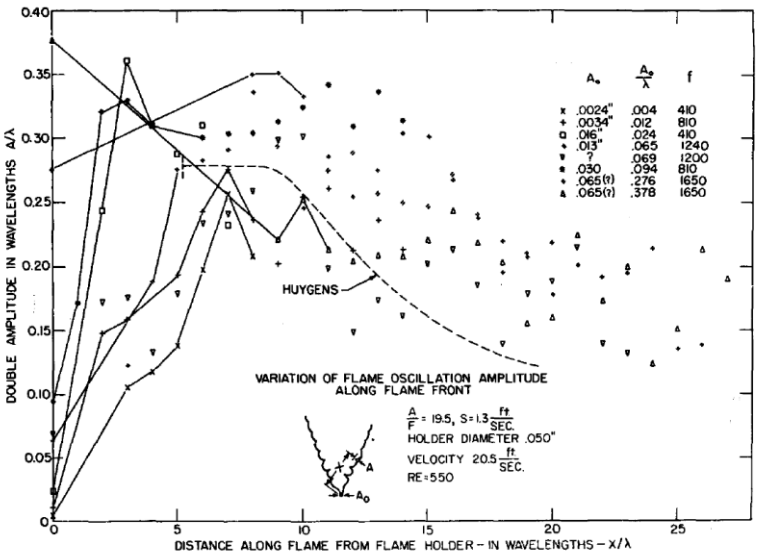

Figure 4.3. Dependency of the magnitude of the flame position fluctuation on the downstream distance for different conditions. Initial flame wrinkle is excited by the oscillating flame holder [36].

4.3 Flame Excitation for Attached Flames

The second and the third examples are the flame response of the attached flame to velocity disturbances; either harmonic or broadband. For the harmonic velocity disturbance case, the flame response at the forcing frequency will be analyzed, while for the broadband velocity disturbance case, the root mean square value of the flame position will be analyzed. Equations (4.5) and (4.6) suggested that the velocity disturbance and the flame speed disturbance can be lumped together as $v_{F,n1}$.

With the flame attachment and unsteady normal velocity assumptions, Eq. (4.8) is reduced to:

$$\xi_1(x,t) = \frac{1}{u_{s,0}\cos^2\theta}\int_0^x v_{F,n1}\left(\chi,\, t - \frac{x-\chi}{u_{s,0}\cos\theta}\right) d\chi \tag{4.13}$$

First, this solution suggests that the flame response is proportional to the integration of the normal velocity disturbance over the downstream distance. Therefore, if we drop the time dependency on the velocity disturbance, the flame response linearly increases over the downstream distance. However, note that the time dependency on the integration will cause the flame to respond non-monotonically because of interference, a topic which will be covered in the next section. Second, this equation suggests that the flame response is inversely proportional to the mean tangential velocity.

4.3.1 Example 2: Harmonic Velocity Disturbance

In this section, we assume that the velocity disturbance is harmonic and obtain the flame response at the forcing frequency. It is convenient to decompose the velocity field in terms of gain and phase, where gain is varying arbitrarily over the downstream distance and phase is simply convected with constant phase speed of $u_{c,v}$. Then, the velocity is expressed in terms of Taylor series as:

$$\frac{v_{F,n}{}'(x,t)}{\cos\theta} = \mathrm{Re}\left[\left(a_0 + a_1 x + \cdots\right)\cdot\exp\left(i\omega_0\left(t - x/u_{c,v}\right)\right)\right] \tag{4.14}$$

Similarly, we can assume the form of the flame response as following:

$$\xi'(x,t) = \mathrm{Re}\left[\,|\xi'(x)|\cdot\exp\left(i\left\{\omega_0 t + \phi_f(x)\right\}\right)\right] \tag{4.15}$$

At the flame attachment point (x=0), the flame attachment condition indicates $\xi'(t)=0$, or $d\xi'/dt=0$. Taking the absolute value of the remaining terms and noting that $|\partial\xi'/\partial x| = \partial|\xi'|/\partial x$ since $\xi'(t) = 0$, leads to:

$$|\xi'(x)| = \frac{a_0}{u_{s,0}\cdot\cos\theta}x + \frac{a_1}{2u_{s,0}\cdot\cos\theta}x^2 + O\left(x^3\right) \tag{4.16}$$

Expanding the solution in Eq. (4.15) around $x=0$ subject to the boundary conditions there leads to:

$$\phi_f(x) = -\frac{1}{2}\left(\frac{\omega}{u_{c,v}} + \frac{\omega}{u_{s,0}\cdot\cos\theta}\right)x - \frac{a_1}{12a_0}\left(\frac{\omega}{u_{c,v}} - \frac{\omega}{u_{s,0}\cdot\cos\theta}\right)x^2 + O\left(x^3\right) \quad (4.17)$$

Lastly, at x=0, the gain and the slope of phase can be derived as follows:

$$\left.\frac{\partial|\xi'|}{\partial x}\right|_{x=0} = \frac{|u_n'|}{u_{s,0}}\frac{1}{\cos^2\theta} \quad (4.18)$$

$$\left.\frac{\partial\phi_f}{\partial x}\right|_{x=0} = -\frac{1}{2}\left(\frac{\omega_0}{u_{c,v}} + \frac{\omega_0}{u_{s,0}\cdot\cos\theta}\right) \quad (4.19)$$

Equation (4.18) shows that the increase of the flame response as a function of downstream distance is proportional to the magnitude of the normal velocity fluctuation. There are additional factors which contribute, such as the inverse relation with the mean tangential velocity and the flame angle. For the phase in Eq. (4.19), the slope of the phase is equal to the harmonic mean of the disturbance convective velocity and the mean tangential velocity.

This linear relationship between the rate of the flame response increase and the magnitude of the velocity fluctuation is verified in the bluff-body stabilized flame. Shanbhogue measured the flame response at the forcing frequency at various conditions using the Mie scattering image [34]. In Figure 4.4, he showed that the flame responses in the near field increase linearly over the downstream distance. Furthermore, all data collapse into a single line in the near field (x/λ_0<1.5) when the gains are scaled by a reference velocity, u'_a. Note that the reference velocity disturbance used in these measurements is not the velocity right at the flame front, but the one measured well ahead of the flame holder. However it is hypothesized that the reference velocity disturbance is proportional to the actual velocity disturbance with a constant.

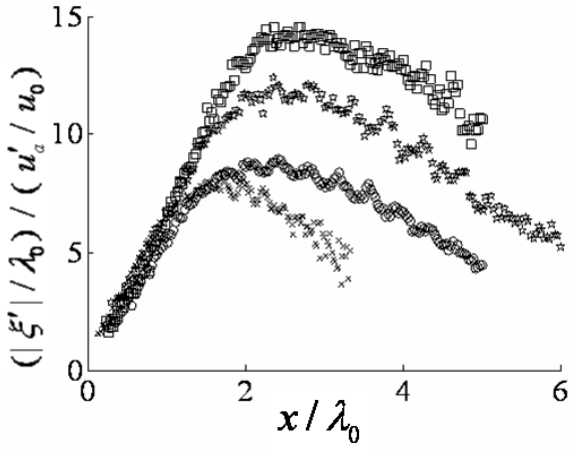

Figure 4.4. Measured amplitude response normalized by acoustic velocity amplitude upon normalized axial distance, $\lambda_0=u_0/f_0$: (o) f_0 = 150 Hz, u_a'/u_0 = 0.028/2.27, (★) f_0 = 150 Hz, u_a'/u_0 = 0.01/2.27, (□) f_0 = 180 Hz, u_a'/u_0 = 0.015/2.27, (×) f_0 = 150 Hz, u_a'/u_0 = 0.021/3.37 (cylindrical bluff body, reproduced from Shanbhogue [34])

Among the flame response shown in Figure 4.4, he also measured spatial/temporal velocity field by particle image velocimetry. Based on this data set, we tried to validate the relationship between the flame response with the velocity as shown in Eq. (4.18). Figure 4.5a and Figure 4.5b show the measured flame response and the measured normal velocity disturbance, respectively. Around x/λ_0=0.3~0.6, the rate of the increase of the flame response is around 0.14 and the corresponding the normalized velocity disturbance is 0.15, indicating the good match of Eq. (4.18).

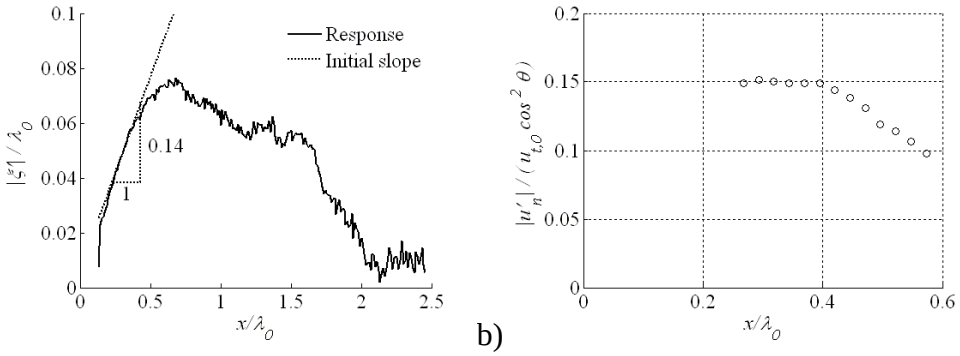

a) b)

Figure 4.5. a) Dependence of flame front fluctuation spectrum, $|\xi'(x, f_0)|/\lambda_0$ upon axial location. b) Dependence of normal velocity fluctuation amplitude, $|u_n'(x, f_0)|/(u_{s,0}\cos^2\theta)$ upon axial direction. (u_0 = 4.5 m/s, f_0 = 300 Hz)

Equation (4.18) is also validated for the high velocity flow flame [71]. The investigated flame is also the bluff-body stabilized flame but in a closed chamber. In this experiment, the flame position is measured by luminosity of the flame and the velocity is measured by the particle image velocimetry. Figure 4.6a and Figure 4.6b show the measured flame response and the measured normal velocity with the error bar, respectively. Around $0.1<x/\lambda_c<0.7$, the rate of the increase of the flame response is 0.109, and the normal velocity measurement suggests that the value is 0.11. Therefore within the error bound, it shows the good match of Eq. (4.18).

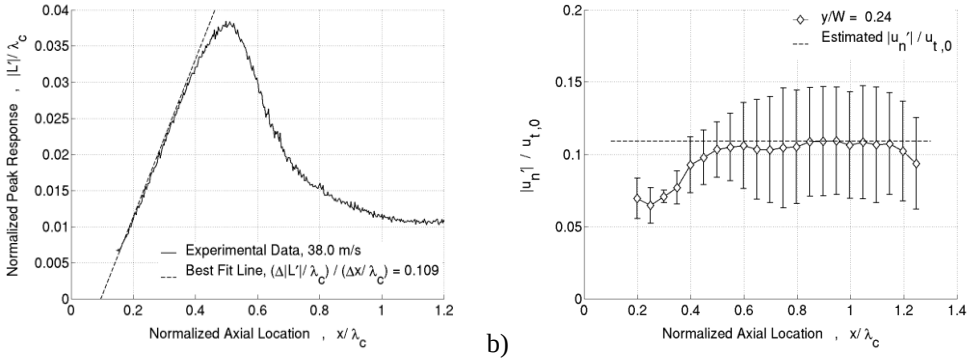

a) b)

Figure 4.6. a) Normalized flame edge amplitude and best-fit line to the initial linear region. b) Ratio of transverse velocity amplitude to mean axial velocity as a function of downstream distance. The slope of the best-fit line from a) is the dashed line. The excitation voltage is 12V and the mean flow velocity is 38 m/s.

Therefore, the gain relationship equation is verified in the bluff-body stabilized flames, where the attachment condition is a valid assumption.

4.3.2 Example 3: Broadband Velocity Forcing

This section presents an example focusing on the anchored flame with tangential flow as shown in Figure 4.7, subjected to random turbulent fluctuations. This problem is analogous to the harmonically forced problem considered in the previous section with the velocity model replaced by a random function.

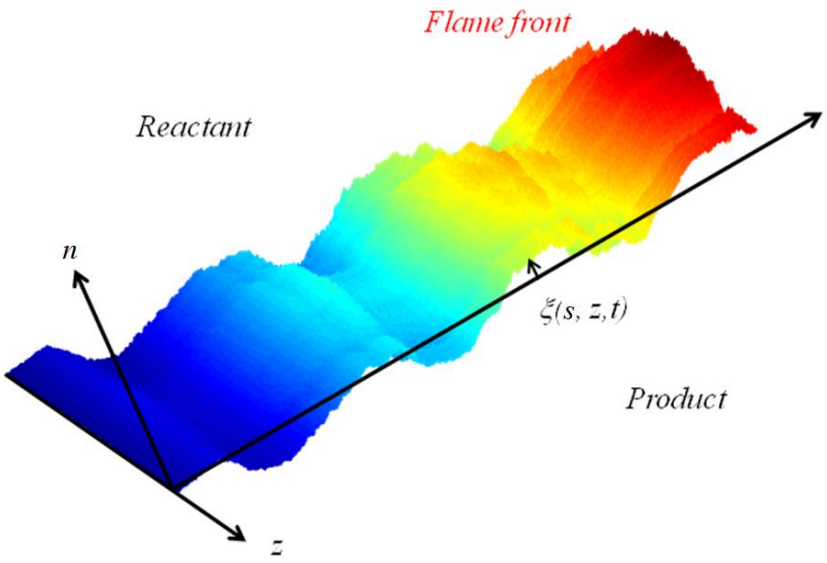

Figure 4.7 Schematic of an anchored turbulent flame with tangential flow showing the coordinate system used for the model problem.

Here, for the simple presentation, a coordinate system is fixed to the tangential-normal coordinates, (s,n,z), as opposed to flow direction coordinates, (x,y,z), which

was used in previous sections. The governing equation for the three dimensional flame front is:

$$\frac{\partial \xi}{\partial t} + u_s \frac{\partial \xi}{\partial s} - u_n + u_z \frac{\partial \xi}{\partial z} = S_L \sqrt{1 + \left(\frac{\partial \xi}{\partial s}\right)^2 + \left(\frac{\partial \xi}{\partial z}\right)^2} \tag{4.20}$$

The turbulent velocity assumed to be isotropic combined with Taylor's hypothesis in order to relate space and time correlations and explicitly specify the following longitudinal velocity space correlation function:

$$R_{LL}(\boldsymbol{r}) = \exp\left(-\frac{\pi}{4}\left(\frac{\boldsymbol{r}}{L_{11}}\right)^2\right) \tag{4.21}$$

where $\boldsymbol{r}$ and L_{11} are the distance between two points and the longitudinal integral length scale, respectively. With the similar decomposition as in Sec. 4.1, the linearized version of the flame position is obtained as:

$$\xi_1(s,z,t) = \frac{1}{u_{s,0}} \int_0^s v_{F,n1}\left(\chi,\, t - \frac{s-\chi}{u_{s,0}}\right) d\chi \tag{4.22}$$

From this relationship, since the ensemble average of the velocity fluctuation is zero, i.e., $\langle v_{F,n1} \rangle = 0$, the ensemble average of the flame position, $\langle \xi_1 \rangle$, also vanishes. Therefore, in order to illustrate the magnitude of the unsteady motion, the root mean squared value of the flame position is considered, which is:

$$\left(\xi_1(s,z,t)\right)^2 = \frac{1}{\left(u_{s,0}\right)^2}\left[\int_0^s v_{F,n1}\left(\chi_1,\, t - \frac{s-\chi_1}{u_{s,0}}\right) d\chi_1\right] \cdot \left[\int_0^s v_{F,n1}\left(\chi_2,\, t - \frac{s-\chi_2}{u_{s,0}}\right) d\chi_2\right] \tag{4.23}$$

As the equation involves the product of two velocities, the velocity correlations are required. The derivations for the correlation function are in APPENDIX H. Then, the solutions for $\langle \xi_1^2 \rangle^{1/2}$ is:

$$\left\langle \xi_1(s)^2 \right\rangle^{1/2} = \left\{ \begin{array}{l} \frac{4L_{11}{}^2}{\pi}\left[\exp\left(-\frac{\pi}{4}\left(\frac{s\cdot\tan\theta}{L_{11}} \right)^2 \right) - 1 \right] \\ \qquad + 2sL_{11}\tan\theta\cdot\mathrm{erf}\left(\frac{\sqrt{\pi}s\cdot\tan\theta}{2L_{11}} \right) \end{array} \right\}^{1/2} \frac{u_{rms}}{\sqrt{3}S_L} \tag{4.24}$$

whose leading order contribution for small s/L_{11} value is given by:

$$s/L_{11} << 1: \quad \left\langle \xi_1{}^1 \right\rangle^{1/2} = \frac{u_{rms}\tan\theta}{\sqrt{3}S_L}s + \mathrm{O}\left(s^3\right) \tag{4.25}$$

This equation shows that the flame brush thickness grow linearly with downstream distance, *s*. The downstream growth in flame brush thickness is a well known experimental result for turbulent flames [46].

Figure 4.8 compares these flame brush calculations with the solutions for $|\xi_1|$ for the homogeneous harmonic forcing case, i.e., $v_{F,n1} = \sin\left(2\pi f_0 t\right)$. Note the identical behavior of both curves near the attachment point, but then the sharp difference farther downstream, with interference effects dominating the behavior of the harmonic case and turbulent diffusion in the random case. The interference effect will be detailed in the next chapter.

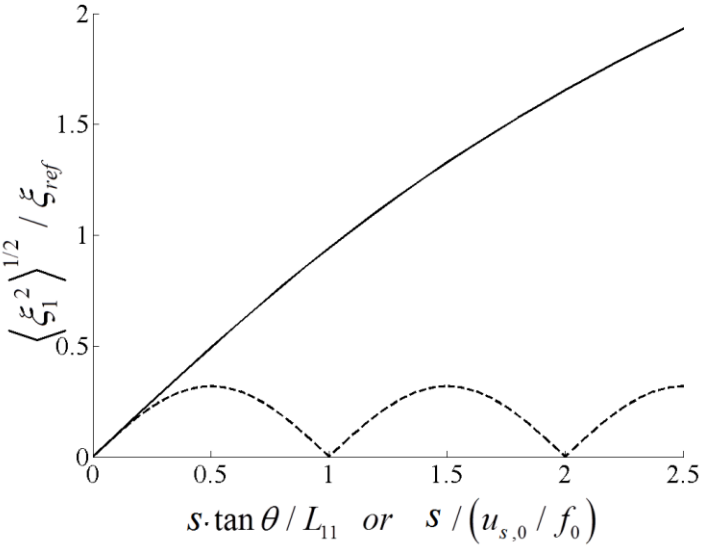

Figure 4.8. Comparison of the axial dependence of the flame brush thickness of a flame subjected to harmonic ($\xi_{ref} = \left(v_{F,n1}\right)_{rms} / f$) and random ($\xi_{ref} = \left(u_{rms} / \left(\sqrt{3} S_L\right)\right) L_{11}$) disturbances. Reproduced from [27].

CHAPTER 5

FLAME WRINKLE EXCITATION PROCESSES – DISTURBANCE DECAY EFFECTS

This chapter covers the flame response excited by a decaying disturbance. It presents analytic and numerical results along with the experimental validation to understand the temporal/spatial flame response. While the previous chapter covers the excitation of the flame response in the near field, this chapter extends the analysis further downstream with the decaying disturbance. Furthermore, we also try to understand the factors controlling the different types of behaviors as shown in Figure 5.1; Figure 5.1a shows a repeating node/antinode behavior, while Figure 5.1b shows a single peak in the similar downstream domain.

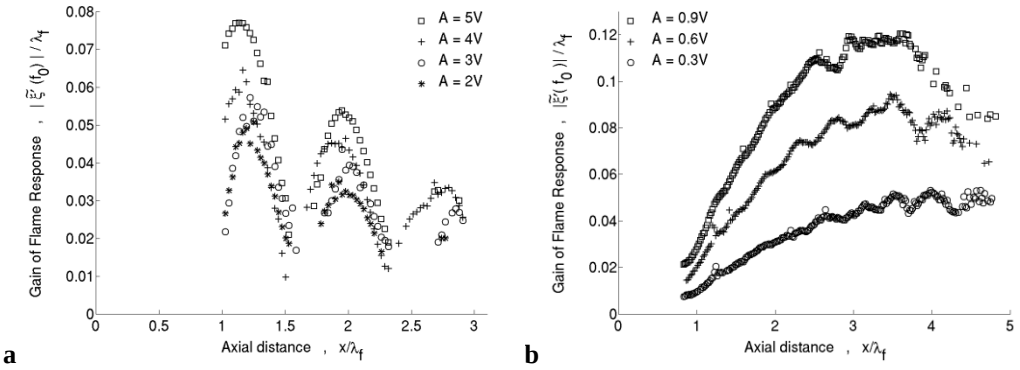

a **b**

Figure 5.1. Dependence of flame front fluctuation magnitude and effective convection speed of flame response for circular bluff-body with 9.52mm diameter (a) 230hz, $u_{x,0}$=2.0m/s (b) 200hz, u_0=2.52m/s ("A" represents the excitation voltage to the loud speaker. Reproduced from Shanbhogue et al.[72, 73])

The first two sections introduce the decaying velocity model and the flame kinematic model. In the third section, the analytic solution shows that the flame response

exhibit two fundamentally different behaviors, referred to here as "interference dominated" and "dissipation dominated" behaviors. The last section validates two different behaviors with experimental data. A key contribution of this chapter is to focus on the flame characteristics farther downstream where interference of excitations and decay of vorticity fundamentally control the flame characteristics.

5.1 Decaying Disturbance Velocity Field

In unsteady flows, the velocity fluctuations can be decomposed into three components: vortical, entropy, and acoustic disturbances [30]. Among these disturbances, the vortical disturbance is suspected to be the main driver for the unsteady flame response [12]. The vortical disturbance is generated by the flame holder or the abrupt change of the combustor geometry. Once generated, the vortical disturbance is dissipated further downstream by various mechanisms; they include vortex stretch, baroclinic torque, viscosity, and gas expansion [74]. Especially, inside the combustion chamber, the temperature rises significantly, leading to high gas-expansion and an increase of viscosity, both of which accelerate the dissipation of the vortical disturbances.

In order to model the flame response in the further downstream, we first need to better characterize the velocity disturbance, mainly a vortical disturbance. Many vortex models have been developed including the Rankine vortex, the Bachelor vortex, and the Oseen vortex [75]. Among those models, a distinctive feature of the Bachelor vortex and the Oseen vortex is that the strength of the velocity disturbance decays exponentially in time. The decay in time of these two models can be applied to the decay in space in our problem through the convection of the vortex - this convection speed of vortices

determines the conversion factor from time to space. The convection velocity, $u_{c,v}$, is similar to the mean flow velocity, but not necessarily same, as the vortices usually lie in the shear layer.

Although those vortex models specify velocities at all points, the flame kinematic equation in Eq. (2.4) only requires the velocities at the flame front, a 2D surface. Therefore, those vortex models can be reduced to specify the velocity on the flame front. Furthermore, Eq. (4.7) indicates that only the normal velocity has the leading order effect for the flame response. Therefore, the vortex models are further reduced to specify the normal velocity disturbance at the flame front in the following form:

$$v_{F,n1} / u_{x,0} = \varepsilon \cdot e^{-\gamma x} \cos\left(2\pi f_0 \left(t - x / u_{c,v}\right) + \psi\right) \tag{5.1}$$

where, $v_{F,n1} = u_{x,1} \sin\theta - u_{y,1} \cos\theta - S_{L,1}$ as defined in Eq. (4.6) (see Figure 5.2 for symbols). This Eq. (5.1) describes periodic flow disturbances with an initial amplitude, ε, an initial phase, ψ, and an exponential decay rate, γ, that propagate downstream with a speed, $u_{c,v}$.

Several prior studies have considered the flame response to convecting velocity disturbances whose amplitudes do not decay [76]; i.e., setting γ=0. However, this is a problematic assumption as it implies that the excitation source of flame wrinkling persists indefinitely downstream, and this leads to predicted flame wrinkling fluctuations that also persists indefinitely – a prediction that is clearly at odds with data, such as shown in Figure 5.1.

In addition, we assume a spatially uniform axial mean velocity, a zero mean transverse velocity, and a flame attachment condition [33], which are expressed as:

$$\vec{u}_0 = u_{x,0} \vec{e}_x, \quad \xi\left(x = 0, t\right) = 0 \tag{5.2}$$

These assumptions can be readily relaxed, but do not fundamentally change the solution characteristics.

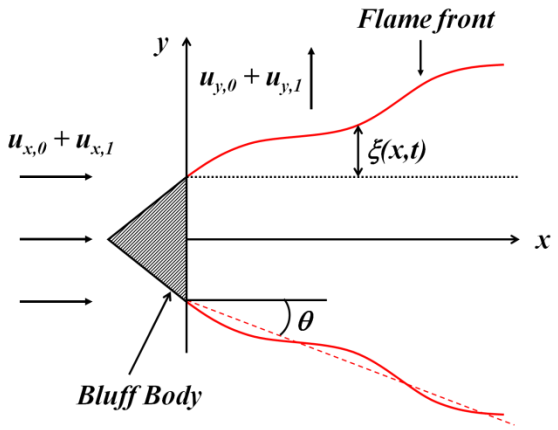

Figure 5.2. Schematic of bluff-body stabilized flame with its corresponding coordinates. red solid : instantaneous flame front, red dash : mean flame position, θ = the angle of mean flame position measured from the flow direction.

5.2 Kinematic Model

The investigated geometry is a 2D/axi-symmetric bluff-body stabilized flame, as shown in Figure 5.2. The instantaneous location of the flame surface is determined from the *G*-equation. The principal assumptions made in this analysis are that: (i) the flame is a thin interface, dividing reactants and products, (ii) the velocity perturbation is prescribed, (iii) the flame speed, S_L is a constant. For small velocity fluctuation, the flame front position is single-valued, an approximation that breaks at high amplitude fluctuations. This leads to the following equation for the flame position, $\xi(x,t)$, or a 2D version of Eq. (3.2) as:

$$\frac{\partial \xi}{\partial t} + u_x \frac{\partial \xi}{\partial x} - u_y = S_L \left[\left(\frac{\partial \xi}{\partial x} \right)^2 + 1 \right]^{1/2} \tag{5.3}$$

This equation was solved both analytically by linearization, and numerically for the general case of large amplitudes. The analytical solution was obtained by decomposing u_x, u_y, and ξ into its time average and perturbation as described in Section 3.3. For the fully nonlinear case, Eq. (5.3) is solved numerically by the methods described in Section 3.4.1.

5.3 Solution Characteristics: Interference/Dissipation Dominated Flame Response Regimes

The solution for the linearized equation of Eq. (5.3) with the velocity models and the flame boundary condition specified in Eq. (5.1) and (5.2) is given by:

$$\xi_1 = \mathrm{Re}\left[A\left(\exp\left(-\gamma x + i2\pi f_0 x / u_{c,v}\right) - \exp\left(i2\pi f_0 x / u_{c,f}\right)\right)\cdot \exp\left(-i2\pi f_0 t\right)\right]$$
$$\textit{where, } A = \frac{\varepsilon u_{x,0} \tan\theta e^{-i\psi}}{f_0(\gamma u_{c,f} / f_0 + i2\pi(1 - u_{c,f} / u_{c,v})} \tag{5.4}$$

Wrinkles excited on the flame front propagate downstream at the characteristic velocity, $u_{c,f} = u_{x,0}\cos^2\theta$ (see Figure 5.3), which equals the axial component of the tangential mean velocity; i.e., $u_{c,f} = \left(\vec{u}_{x,0} - S_L\vec{n}\right)\cdot\vec{e}_x$, where $\vec{n}$ is the normal unit vector to the flame front pointing to products.

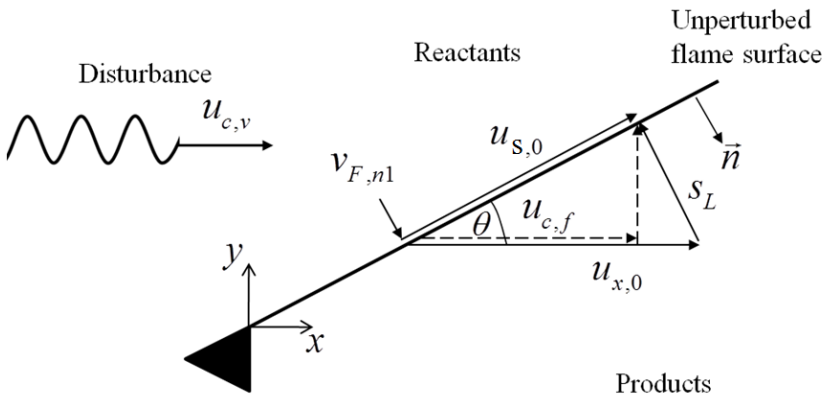

Figure 5.3 An illustration of the top half of an attached flame, indicating the velocity components tangential and normal to the flame and a disturbance which convects downstream at a speed of $u_{c,v}$.

Note that the solution consists of two parts. First, the particular solution is excited by the unsteady velocity field at all positions upstream of x. Second, the homogeneous solution is controlled by the boundary condition at x=0, $\xi(x=0,t)=0$. Mirroring the underlying perturbation velocity field, the particular solution propagates with the same phase velocity as the excitation, $u_{c,v}$. In contrast, the homogenous solution propagates at a phase velocity, $u_{c,f}$.

Next, it is useful to start with the solution characteristics when γ=0, in which case the spatially dependent gain term in Eq. (5.4) is:

$$|\xi_1(x)| = A \cdot \sin(\pi(u_{c,f} / u_{c,v} - 1)x / \lambda_f) \tag{5.5}$$

where, $\lambda_f = u_{c,f} / f_0$. This shows that the gain oscillates periodically over the length scale, $\lambda_f / |u_{c,f} / u_{c,v} - 1|$, with the first maximum occurring at $x = \lambda_f / \left|2\left(u_{c,f} / u_{c,v} - 1\right)\right|$. In other words, the magnitude of flame front oscillations will be near zero at some locations, large at other locations, and oscillate spatially downstream, repeating this pattern. This spatial behavior is identical to that of a standing acoustic wave, but for

entirely different reasons. In a standing wave, this alternating node/antinode behavior is due to the superposition of two waves propagating at the same speeds, but in opposite directions. For this problem, this behavior is due to two waves propagating in the same direction, but at different speeds. This behavior reflects the important role of interference between the particular and homogeneous solution.

The above solution in Eq. (5.5) clearly shows the significance of two length scales to the problem: the convective wavelength, λ_f , and the interference wavelength, $\lambda_f / |u_{c,f} / u_{c,v} - 1|$. The length scale over which the velocity magnitude is significant, $1/\gamma$, is also significant as discussed next.

The flame exhibits two limiting behaviors based upon the relative magnitudes of the latter two length scales, $\lambda_f / |u_{c,f} / u_{c,v} - 1|$ and $1/\gamma$. In other words, if the disturbance persists far downstream relative to the interference wavelength, then the flame behavior will resemble that described by Eq. (5.5) and exhibit significant oscillatory gain behavior as shown in Figure 5.1a. Moreover, the drop in gain after a local maximum is not due to dissipation, but interference. In contrast, if the velocity disturbance decays quickly relative to this interference wavelength, then this oscillatory gain behavior does not occur. The drop in flame gain after the point of peak response in this case is due to dissipation of velocity disturbances and destruction of flame wrinkles as shown in Figure 5.1b.

Moreover, the flame response for spatial regimes where $\gamma x >> 1$ will be dominated by a single flame wrinkling source, the homogeneous solution, which propagates at the speed $u_{c,f}$. The first limit we title the *Interference dominated regime*, where two waves with similar magnitudes interfere with each other to result in an oscillatory gain. The

other limit is *Dissipation dominated regime*, where the velocity disturbance dissipates rapidly relative to the interference wavelength:

$$\begin{aligned} &\textit{Dissipation dominated regime}: \ \gamma\lambda_f / |u_{c,f} / u_{c,v} - 1| \ >> 1 \\ &\textit{Interference dominated regime}: \ \gamma\lambda_f / |u_{c,f} / u_{c,v} - 1| \ << 1 \end{aligned} \tag{5.6}$$

Recognizing these two limiting behaviors is very helpful for interpreting the range of different types of flame response behaviors that are experimentally observed, such as those seen in Figure 5.1.

Typical values of $u_{c,f}/u_{c,v}$ for vortical disturbances are on the order of unity. For example, Michalke calculates values of $0.5<u_{c,v}/u_{x,0}<1.25$ for the propagation velocity of the most amplified axisymmetric shear layer disturbance [77]. This indicates that vortically disturbed flame characteristics are quite sensitive to small changes in the propagation velocity. For example, a 20% increase in $u_{c,v}/u_{x,0}$ from 0.7 to 0.84 changes the first maximum location in flame gain from $1.5\lambda_f$ to $2.6\lambda_f$, see Eq. (5.5). In contrast, typical values of $u_{c,f}/u_{c,v}$ for acoustic disturbances are quite small, approaching zero for a plain wave. The interference wavelength is quite close to the convective wavelength in this case, $\lambda_f / |u_{c,f} / u_{c,v} - 1| \approx \lambda_f$.

It is also useful to consider the phase variation of the flame response. Far downstream where the vortex has decayed, flame wrinkles propagate at the speed $u_{c,f}$. This corresponds to a phase slope, $\partial\psi / \partial(x / \lambda_f) = 2\pi$. Phase characteristics are more complex close to the flame holder where the velocity disturbance is strong. In this region, the net flame wrinkling is a superposition of two disturbances. Henceforth, the resultant phase slope does not correspond to the propagation speed of any physical

disturbance, but rather the vector summation of multiple disturbances. A simple result for this phase variation can be derived when $\gamma x << 1$, see Eq. (5.4),

$$\partial\psi / \partial(x / \lambda_f) = \pi(u_{c,f} / u_{c,v} + 1) \tag{5.7}$$

This discussion shows that the slope of the axial phase variation changes with downstream distance, evolving from a value of $\pi\left(u_{c,f} / u_{c,v} + 1\right)$ near the flame holder ($\gamma x << 1$), to a value of 2π farther downstream ($\gamma x >> 1$).

These linearized solution characteristics are helpful for understanding the important roles of propagation velocity disparities between the flame wrinkles and the vortex, and the rate of vortex decay, in controlling the solution characteristics. However, nonlinear effects are required to capture the far field decay in flame response. For example, the linearized solution, to be shown in the following section, approaches a non-zero steady state (i.e., oscillation about a non-zero value), which is not consistent with the data shown in Figure 5.1a. This nonlinear process arise from the inherently nonlinear kinematic restoration processes, whereby the flame propagates normal to itself. This nonlinear process leads to a gradual reduction in flame wrinkling amplitude with increasing distance downstream [78], which will be deeply covered in Section 6.3.1.

5.4 Simulation Results and Analysis of Data

Having discussed general solution characteristics and obtained the ranges of parameters, this section presents and discusses results from these simulations and the implications of these results on understanding flame response data.

In order to compare the analysis with measurements, the model requires specification of several parameters specified in Eq. (5.1). Unfortunately, we do not have

simultaneous flame and flow field data. Extensive separate flame and flow field measurements were obtained by Shanbogue [79], which allow some assessment of bounds on these parameters. More details about post-processing procedures can be found in Ref. [80], which suggest that $u_{c,v}/u_{c,f}$ ranges from 0.5 to 1.4 and $\gamma\lambda_0$ ranges from 0.3 to 2.4 for vortical disturbances. For reference, other measurements indicate values of $u_{c,v}/u_{x,0}$ = 1 or 1.13 for the vortical convection speed [81-83].

5.4.1 Predictions of the Flame Response in the Interference Dominated Regime

First, the axial location at which the flame response peaks, x_{peak}, is examined. This axial location cannot be precisely determined since the flame edge is blurred by the line of sight measurement. But the sensitivity study on the threshhold values, I_t suggests the peak lies between $0.4 < x_{peak}/\lambda_c < 0.6$ (See Figure 5.4).

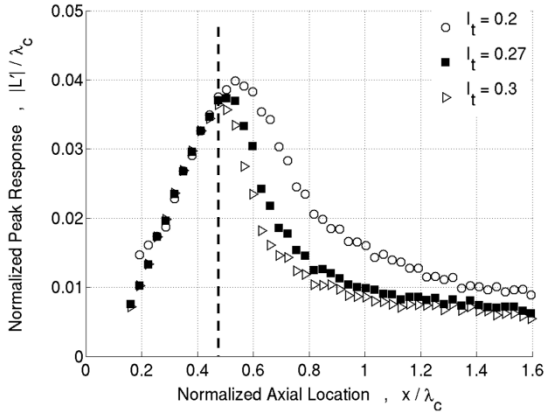

Figure 5.4. Dependence of flame edge response amplitude on threshold value, I_t and theoretical estimation of the peak location shown in dashed line. Fow conditions: 38 m/s mean flow velocity, 644 K approach temperature, and 12V excitation [71].

Simple theoretical calculations of x_{peak} cannot be developed, since x_{peak} depends upon amplitude of perturbation and the detailed character of the velocity field. However,

an approximate expression for x_{peak} can be derived using wave interference arguments, as shown in Eq. (5.5). Since flame excitation and flame response disturbances do not propagate at the same speed, they lead to constructive and destructive interference along the flame [84]. The location of x_{peak} approximately coincides with the point where they constructively superpose with each other; i.e., where they are in phase. As shown in Eq. (5.5), this leads to the following predicted location for x_{peak}:

$$x_{peak} / \lambda_c = \frac{\cos^2 \theta}{2\left|u_0 \cos^2 \theta / u_{c,v} - 1\right|} \tag{5.8}$$

It should be noted that this equation assumes the decay in the exciting vortex is negligible at x_{peak}, which appears to be the case as from Figure 5.5. Using the value of $u_{c,v}/u_0 = 0.48$ (see Ref. [71]), Eq. (5.8) predicts that x_{peak}/λ_c=0.45. This prediction, indicated by the dashed vertical line in See Figure 5.4, is in good agreement with the data. Note that when $u_{c,v} \sim u_{x,0}$, the sensitivity of x_{peak} to parameter values and uncertainties is very large, making it more difficult to accurately predict.

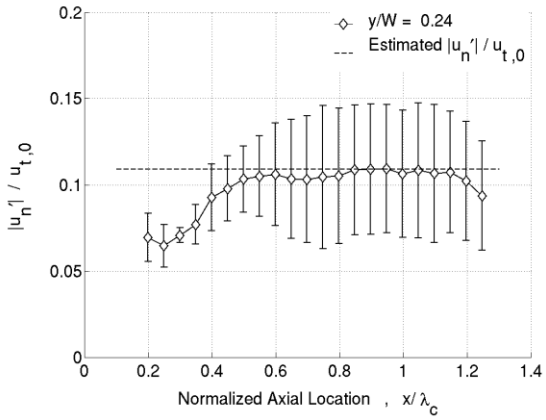

Figure 5.5. Ratio of transverse velocity amplitude to mean axial velocity as a function of downstream distance. The slope of the best-fit line from a) is the dashed line. The excitation voltage is 12V and the mean flow velocity is 38 m/s [71].

5.4.2 Solution Characteristics in the Far Field

5.4.2.1 Interference Dominated Regime

We start with linear and nonlinear solution characteristics for the interference dominated case. Figure 5.6 plot the calculated spatial distributions of the flame gain and phase for $\gamma\lambda_f / |u_{c,f} / u_{c,v} - 1| = 0.36$ with $u_{c,f} / u_{c,v} = 0.006$ (i.e., an acoustic disturbance with slow decay).

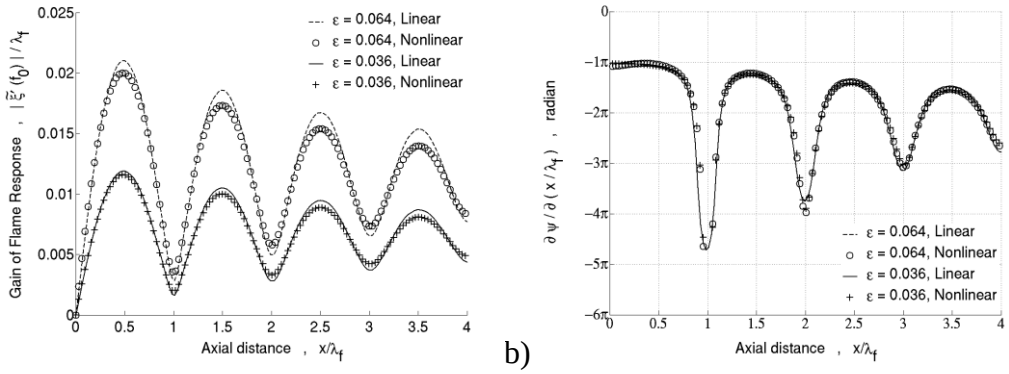

a) b)

Figure 5.6. Dependence of flame front fluctuation magnitude and effective convection speed of flame response a) gain, and b) slope of phase. Simulation with $u_{c,f}/u_{c,v}=0.006$, $\gamma\lambda_f=0.36$.

Starting with the linear case, note the periodic undulations in flame gain. For example, at $x=0.5\lambda_f$ in the former case, the flame exhibits large amplitude wrinkling, while at $x=\lambda_f$, the flame response is approximately zero. This repeating node/anti-node behavior was anticipated by the discussion in the context of Eq. (5.5). The amplitude of undulation slowly decreases with downstream distance, due to the small but nonzero value of γ. The undulation amplitude of the linearized solution does not decay to $|\xi_1|=0$, however, but oscillates around some offset value corresponding to the homogeneous solution. Nonlinear effects cause the gain response to actually tend toward a zero value

through the action of kinematic restoration. However, this occurs farther downstream than what is shown in this graph.

Turning to the phase, note the roughly constant value of the phase slope at $-\pi$, accompanied by rapid phase changes near nodal points. In addition, the phase slope gradually drifts toward -2π, the value associated with the homogeneous solution alone. This drift is slow because of the low value of the dissipation parameter.

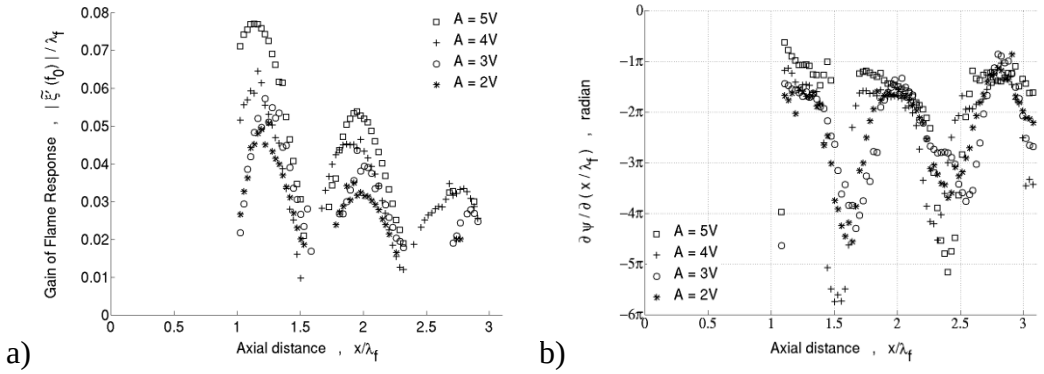

a) b)

Figure 5.7. Dependence of flame front fluctuation magnitude and effective convection speed of flame response for circular bluff-body with 9.52mm diameter measurements a) gain, and b) slope of the phase. (conditions: f_0=230hz, u_0=2.0m/s, β=4, *A* describes the excitation voltage to the loud speaker. Reproduced from Shanbhogue et al.[72, 73])

These flame gains and phase characteristics are very similar to the experimental results shown in Figure 5.7. Specifically, the experimental data clearly show the oscillatory flame gain, associated with repeating nodes and antinodes, spaced at even intervals of λ_f. This nodal spacing suggests that the dominant velocity disturbance is a fast propagating acoustic disturbance. Although not shown, an even better fit to these gain/phase measurements is obtained assuming the additional presence of a smaller convecting vortical disturbance.

5.4.2.2 Dissipation Dominated Regime

We next consider the solution characteristics for the dissipation dominated case. Figure 5.8 plot the spatial distribution of the flame gain and phase for $\gamma\lambda_f /|u_{c,f} /u_{c,v}-1|$=3.64 with $u_{c,f}/u_{c,v}$=1.33 (i.e., a decaying vortical disturbance). Starting with the linear case, note that only a single peak in flame gain is observed, followed by a decay in amplitude of the linearized solution toward a non-zero $|\xi'|$ value. The effect of nonlinearity is clearly evident by the monotonic reduction in $|\xi'|$ amplitude toward zero in the far field, at a relative rate that increases with disturbance amplitude. Turning to the phase, note the roughly constant value of the phase slope at -2.4π near the flame attachment point. Here, the drift in phase slope toward -2π with increasing downstream distance is clearly evident, the value associated with the homogeneous solution alone.

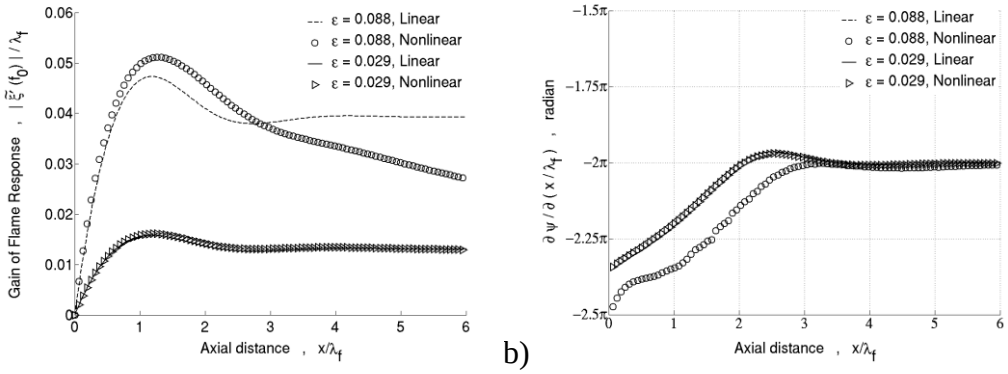

a) b)

Figure 5.8. Dependence of flame front fluctuation magnitude and effective convection speed of flame response a) gain, and b) slope of phase. Simulation with $u_{c,f}/u_{c,v}$=1.33, $\gamma\lambda_f$= 1.20.

These flame gain and phase characteristics can be seen to be very similar to the experimental results shown in Figure 5.9. For example, both experiment and theory

clearly show the nearly constant phase slope near the flame holder, followed by a gradual drift upward. Note that the experimental data does not appear to trend toward the theoretically predicted value of -2π. We believe that this is due to the assumed value of $u_{x,0}$ used here, a value based upon the measured average approach velocity at the bluff body lip.

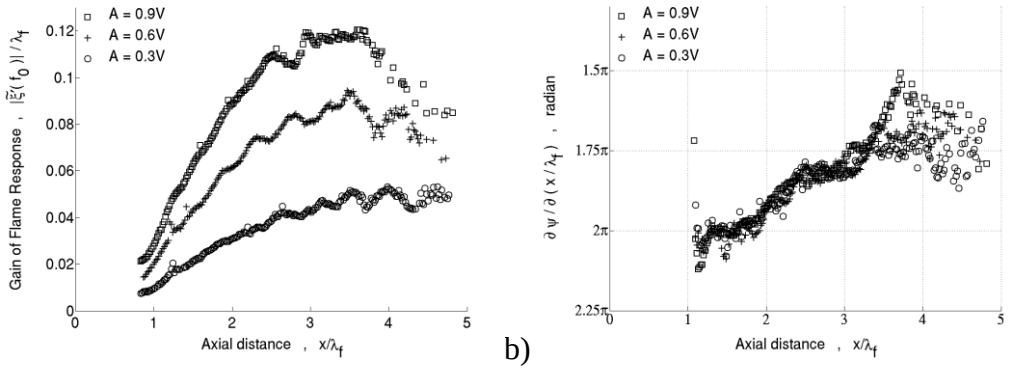

Figure 5.9. Dependence of flame front fluctuation magnitude and effective convection speed of flame response for circular bluff-body with 9.52mm diameter a) gain, and b) slope of phase (conditions: f_0=200hz, u_0=2.52m/s, β=4.3, A describes the excitation voltage to the loud speaker.. Reproduced from Shanbhogue et al. [72, 73])

This latter point is illustrative of the need for careful simultaneous measurements of the unsteady velocity characteristics and flame position to enable quantitative comparisons of measurement and theory. In the previous chapter in CHAPTER 4, efforts has been put along these lines for the near-attachment point region. Required measurements for theory validation farther downstream are more involved, however, requiring estimates of convection velocity (noting also the very significant sensitivity of the gain curves to $u_{c,v}$ noted in the context of Eq. (5.5)), decay rate, phase, and amplitude of simultaneously present acoustic and vortical disturbances. In another combustor

facility in the aerospace combustion lab, they measured simultaneous flow/flame conditions and has compared these results with model predictions [85, 86].

CHAPTER 6

FLAME WRINKLE DECAY PROCESSES IN A LAMINAR FLOW

This chapter describes numerical and theoretical analyses of the nonlinear dynamics of harmonically forced, stretch-sensitive premixed flames. A key objective of this work is to analyze the relative contributions of kinematic restoration and flame stretch upon the rate at which flame wrinkles, excited by harmonic forcing, are smoothed out. Kinematic restoration is an intrinsically nonlinear process with a two spatial-zone structure, whose amplitude dependence is fundamentally different near and far from the wrinkle excitation source. Flame stretch processes appear even in the small perturbation limit, and smooth out flame wrinkles in thermodiffusively stable mixtures. Which process dominates is a function of the perturbation amplitude, frequency, stretch sensitivity of the mixture, and spatial location. This chapter presents computed results illustrating the solution characteristics, as well as key dimensionless parameters controlling the solution based upon a third order perturbation analysis.

6.1 Decaying Mechanisms in the Laminar Flames

In a laminar flame, there are two mechanisms, one linear and the other nonlinear that lead to smoothing of flame wrinkles on individual flame branches. The first mechanism, which is inherently nonlinear, is kinematic restoration; i.e., the propagation of the flame normal to itself leads to smoothing of flame wrinkles [33, 87]. The second, which is linear, is flame stretch, which leads to smoothing of flame wrinkles in thermo-diffusively stable flames, i.e., flames with positive Markstein lengths [22, 88]. To

illustrate, Figure 6.1 depicts an experimental image of a harmonically excited, thermodiffusively stable flame, showing the smoothing of flame wrinkling by stretch effects. Note that for negative Markstein length flames, stretch effects cause amplification of flame wrinkles so that flame wrinkle destruction is controlled by kinematic restoration. While both kinematic restoration and flame stretch processes have been individually studied [22, 37, 88], their relative significance in anchored, harmonically forced flames has not yet been analyzed. The specific objective of this work is to analyze this problem in order to determine the conditions when the downstream decay of the flame is controlled by stretch or kinematic restoration within a constant density framework.

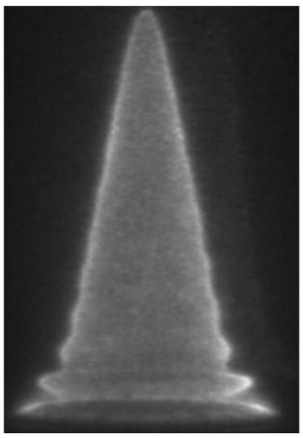

Figure 6.1. Visualization of a propane flame excited by a longitudinal acoustic disturbance at 190 Hz (ϕ = 0.7, $u_{x,0}$ = 0.8 m/s) [22].

In order to study this decaying mechanisms, we analyze an oscillating flame holder with no velocity fluctuations, emulating the study of Petersen and Emmons [36] shown in Figure 6.2. This is a useful problem for this study as the amplitude of flame wrinkling, within a stretch-free and linear analysis framework, is constant with axial location; i.e.,

$|L(x,\omega_0)| = |L(x=0,\omega_0)|$. In contrast, the velocity forced flame has a spatially modulated flame wrinkling character, as shown in Figure 2.7, leading to a complex modulation of nonlinear processes [69]. This oscillating flame holder problem allows us to develop relatively simple expressions for the key dimensionless parameters controlling the problem, and thus, to isolate the critical processes controlling the far field evolution of harmonically forced flames. We will show that the dominant wrinkle damping process depends upon the amplitude of excitation, Markstein length, frequency, and axial location.

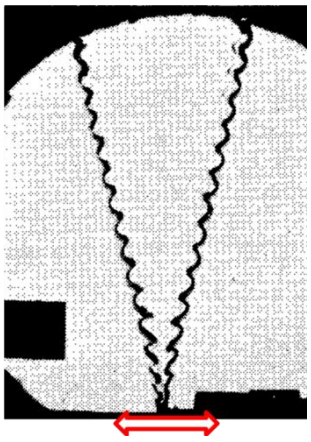

Figure 6.2. Visualization of a propane flame stabilized on a transversely oscillating flame holder at 625 Hz (ϕ = 1, u_0 = 4.8 m/s)[36].

6.2 Formulation

The investigated geometry is a 2D flame that is stabilized at a point as shown in Figure 6.3[iv]. The coordinate system is aligned with the unperturbed flame position, so that the *s*- and *n*-coordinates are tangential and normal to the unperturbed flame, respectively. The flow field is steady and the flame holder vibrates in the *n*-direction, creating wrinkles on the flame at *s*=0 which propagate downstream.

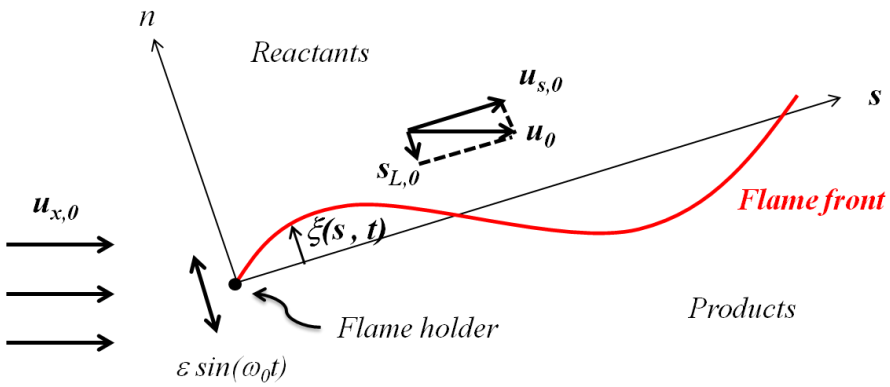

Figure 6.3. Diagram of flame/flow configuration and the coordinates (ξ: flame front location)

The principal assumptions made in this analysis are that: (i) the flame is a thin, two-dimensional interface, dividing reactants and products, (ii) the velocity (u_s ,u_n) is prescribed, (iii) the flame speed, S_L, is related to the flame curvature through the Markstein length, and (iv) the flame remains attached to the flame holder. The

---

[iv] The analysis in this chapter is limited to the 2D flames as opposed to the previous two chapters, where the analysis is also applied to axi-symmetric flames. This is because the curvature expressions are different between 2D and axi-symmetric cases.

instantaneous location of the flame front is determined from the *G*-equation [28], given by:

$$\frac{\partial G}{\partial t} + u_s \frac{\partial G}{\partial s} + u_n \frac{\partial G}{\partial n} = S_L \left[\left(\frac{\partial G}{\partial s} \right)^2 + \left(\frac{\partial G}{\partial n} \right)^2 \right]^{1/2} \tag{6.1}$$

For this problem, the flame front position is single-valued on the variables, *s* and *t*, suggesting the substitution $G=n-\xi(s,t)$ [89]. This substitution leads to the following explicit equation for the flame position, $\xi(s,t)$:

$$\frac{\partial \xi}{\partial t} + u_s \frac{\partial \xi}{\partial s} - u_n = S_L \left[\left(\frac{\partial \xi}{\partial s} \right)^2 + 1 \right]^{1/2} \tag{6.2}$$

The velocity field as shown in Figure 6.3 is given by:

$$\begin{aligned} u_s &= u_{s,0} \\ u_n &= -S_{L,0} \end{aligned} \tag{6.3}$$

It is assumed that there are no velocity fluctuations. Note that this assumption is rigorously valid in the limit of an iso-density flow, but neglects the influence that a finite density change across the flame has on the approach flow, as the oscillatory flame sheet would otherwise induce an oscillatory approach flow. Because of the mutual interaction between the flame position and the flow field, free boundary problems such as this are otherwise difficult to handle analytically. This issue has been discussed by Lee and Lieuwen [90] and Preetham et al. [22] who argue that the qualitative linear dynamics of the harmonically excited flame are captured by constant density analyses, although the quantitative accuracy of the results deteriorates as T_b/T_u increases. In contrast, the nonlinear dynamics of the flame are only correctly described by such analyses for lower T_b/T_u values, i.e., new dynamics appear for simultaneously high values of T_b/T_u and perturbation amplitude due to the appearance of a parametric flame instability [91-93].

Finally, we should note that the general legitimacy of using the iso-density approximation to understand the dynamics of real flames is well supported by the good agreement that has been achieved between analysis and experiment, such as demonstrated in, for example, Refs. [14-16, 33, 82].

Consider next the flame speed, which is related to the unstretched flame speed, the instantaneous curvature, and the hydrodynamic strain rate [37]. Since the hydrodynamic strain rate is zero (see Eq. (6.3)), the flame speed is only a function of the flame curvature, c [37]:

$$S_L/S_{L,0} = f(c) \tag{6.4}$$

where

$$c = -\frac{\partial^2 \xi / \partial s^2}{\left(1+\left(\partial \xi / \partial s\right)^2\right)^{3/2}} \tag{6.5}$$

The function $f(c)$ is expanded in a Taylor series as:

$$S_L/S_{L,0} = 1-\sigma c + A_1(\sigma c)^2 + A_2(\sigma c)^3 + \cdots \tag{6.6}$$

where σ is the Markstein length. The Markstein length is a familiar quantity in the combustion literature and has been extensively studied both theoretically and numerically [94]. The higher order correction terms, A_i, however are not as well understood. Poinsot et al. [41] suggested a flame speed expression, $S_{L,0}/(1+\sigma c)$, which matches the linear behavior for small c and ensures positive flame speed for large positive flame curvatures. Assuming $A_i \sim O(1)$, it can be shown that the higher order flame stretch corrections do not influence $\xi(s,\omega_0)$ for the third order asymptotic analysis presented here. Therefore, the analysis in the next section truncates Eq. (6.6) to the first order as the higher order terms are not needed for the asymptotic and this simplifies the presentation.

Two boundary conditions are needed for the governing, second order partial differential equation, Eq. (6.9). First, it is assumed that the flame is attached to the flame holder which is oscillating in the *n*-direction harmonically, which is expressed as:

$$\xi\left(s=0,t\right)=\varepsilon\cdot\cos\left(\omega_0 t\right) \tag{6.7}$$

where ε and ω_0 denote the magnitude and angular frequency of the flame holder oscillation. Second, a characteristic boundary condition is applied at the downstream end of the calculation domain to ensure that information travels only in the downstream axial direction.

Finally, the governing equation is non-dimensionalized, using the following scheme:

$$\begin{aligned}&\tilde{s}=s/\left(u_{s,0}/\omega_0\right),\quad \tilde{t}=\omega_0 t,\quad \tilde{S}_{L,0}=S_{L,0}/u_{s,0},\\&\tilde{\xi}=\xi/\left(u_{s,0}/\omega_0\right),\quad \tilde{\varepsilon}=\varepsilon/\left(u_{s,0}/\omega_0\right),\ \tilde{\sigma}=\sigma/\left(u_{s,0}/\omega_0\right)\end{aligned} \tag{6.8}$$

Thus, the flame front equation, Eq. (6.2), with the flame speed expression, Eq. (6.6), is re-written as:

$$\frac{\partial\tilde{\xi}}{\partial\tilde{t}}+\frac{\partial\tilde{\xi}}{\partial\tilde{s}}=\tilde{S}_{L,0}\left\{\sqrt{1+\left(\frac{\partial\tilde{\xi}}{\partial\tilde{s}}\right)^2}-1\right\}+\tilde{S}_{L,0}\tilde{\sigma}\frac{\partial^2\tilde{\xi}}{\partial\tilde{s}^2}\cdot\left[\left(\frac{\partial\tilde{\xi}}{\partial\tilde{s}}\right)^2+1\right]^{-1} \tag{6.9}$$

where the first term on the RHS is the nonlinearity associated with kinematic restoration and the second is the flame stretch term. The solution to this equation will be examined using computations as described by Section 3.4.1 and the third order asymptotic analysis in perturbation amplitude, which is described next.

6.2.1 Asymptotic Analysis

Asymptotic analyses of the governing equations were performed to obtain insight into key parameters controlling the flame wrinkle decay rate. The resulting explicit

solutions enable identification of the key dimensionless parameters controlling the problem, and the functional dependence of the solution upon them. Since the objective of this study is to analyze nonlinear corrections to the flame response at the forcing frequency, the analysis must, at minimum, obtain up to the third order in products of the parameters $\tilde{\varepsilon}$ and $\tilde{\sigma}$. Consequently, the flame position, $\tilde{\xi}$, is expanded as:

$$\begin{aligned}\tilde{\xi}\left(\tilde{s},\tilde{t}\right) = & \ \tilde{\xi}_0\left(\tilde{s}\right) + \tilde{\varepsilon}\cdot\tilde{\xi}_\varepsilon\left(\tilde{s},\tilde{t}\right) + \tilde{\sigma}\cdot\tilde{\xi}_\sigma\left(\tilde{s},\tilde{t}\right) \\ & + \tilde{\varepsilon}^2\cdot\tilde{\xi}_{\varepsilon\varepsilon}\left(\tilde{s},\tilde{t}\right) + \tilde{\varepsilon}\tilde{\sigma}\cdot\tilde{\xi}_{\varepsilon\sigma}\left(\tilde{s},\tilde{t}\right) + \tilde{\sigma}^2\cdot\tilde{\xi}_{\sigma\sigma}\left(\tilde{s},\tilde{t}\right) \\ & + \tilde{\varepsilon}^3\cdot\tilde{\xi}_{\varepsilon\varepsilon\varepsilon}\left(\tilde{s},\tilde{t}\right) + \tilde{\varepsilon}^2\tilde{\sigma}\cdot\tilde{\xi}_{\varepsilon\varepsilon\sigma}\left(\tilde{s},\tilde{t}\right) + \tilde{\varepsilon}\tilde{\sigma}^2\cdot\xi_{\varepsilon\sigma\sigma}\left(\tilde{s},\tilde{t}\right) + \tilde{\sigma}^3\cdot\tilde{\xi}_{\sigma\sigma\sigma}\left(\tilde{s},\tilde{t}\right) \\ & + O\left(\left(\tilde{\varepsilon},\tilde{\sigma}\right)^4\right)\end{aligned} \tag{6.10}$$

The corresponding boundary conditions for each function are

$$\tilde{\xi}_\Theta = \begin{cases}\tilde{\varepsilon}\cdot\cos\left(\tilde{t}\right) & \Theta = \varepsilon \\ 0 & \textit{otherwise}\end{cases} \tag{6.11}$$

After inserting the expansion in Eq. (6.10) into Eq. (6.9) and matching terms with the same order, we obtain a series of partial differential equations for each function, $\tilde{\xi}_\Theta$, which are listed in APPENDIX E. For example, the equation for $\tilde{\varepsilon}^2\tilde{\sigma}$ is:

$$O\left(\tilde{\varepsilon}^2\tilde{\sigma}\right):\ \frac{\partial\tilde{\xi}_{\varepsilon\varepsilon\sigma}}{\partial\tilde{t}} + \frac{\partial\tilde{\xi}_{\varepsilon\varepsilon\sigma}}{\partial\tilde{s}} = \tilde{S}_{L,0}\left(\frac{\partial^2\tilde{\xi}_{\varepsilon\varepsilon}}{\partial\tilde{s}^2} + \frac{\partial\tilde{\xi}_\varepsilon}{\partial\tilde{s}}\frac{\partial\tilde{\xi}_{\varepsilon\sigma}}{\partial\tilde{s}} + \frac{\partial\tilde{\xi}_{\varepsilon\varepsilon}}{\partial\tilde{s}}\frac{\partial\tilde{\xi}_\sigma}{\partial\tilde{s}}\right) \tag{6.12}$$

These equations are then solved sequentially with the boundary conditions in Eq. (6.11). For example, the first order solutions are:

$$\begin{aligned}\tilde{\xi}_\varepsilon &= \cos\left(\tilde{t}-\tilde{s}\right) \\ \tilde{\xi}_\sigma &= 0\end{aligned} \tag{6.13}$$

Thus, the flame wrinkle amplitude is constant at the first order; i.e., it does not decay. The solution, $\tilde{\xi}_\varepsilon$, mimics the forcing and describes a flame wrinkle of constant amplitude

that convects downstream as a traveling wave at the tangential velocity, $u_{s,0}$ $(= u_{c,f} / \cos\theta)$.

6.3 Results and Analysis

This section presents analyses of the computational and asymptotic flame response results to understand the factors controlling the downstream dissipation of the flame wrinkles. First, it presents results for kinematic restoration in isolation, then stretch effects in isolation, and finally considers their cumulative effects and the conditions under which one is dominant over the other.

6.3.1 Kinematic Restoration Effects

This section provides results illustrating the role of kinematic restoration in destroying flame wrinkles, in the absence of flame stretch effects (i.e., $\tilde{\sigma}$ is set to zero in Eq. (6.9)). The analysis will show that kinematic restoration exhibits a two-zone spatial structure. Near the oscillatory flame holder, the flame reponse is nonlinearly dependent on the flame wrinkling amplitude while far from the anchoring point, the response is independent of the amplitude.

Figure 6.4a plots a typical calculation for the instantaneous flame position at four instances during a forcing period. The plot clearly indicates the spatial distortion in the shape of the flame wrinkles, which start as sinusoidal wrinkles near $\tilde{s} = 0$ to sharply cusped fronts in the concave portion farther downstream. Also, note that as the flame wrinkle propagates downstream, the trailing edges shift upward while the leading edges

stay at the same height. This indicates that the time averaged flame position is shifting toward the reactants and that the magnitude of the wrinkling is decreasing. These points also can be seen in Figure 6.4b, which shows the corresponding spectral representation of the flame position, depicting the magnitude of flame wrinkling at the forcing frequency and its harmonics. This plot shows the monotonic reduction in magnitude at ω_0 and the monotonic rise in the time average flame position. The oscillations at $2\omega_0$ and $3\omega_0$ are excited in the near field and then decay farther downstream.

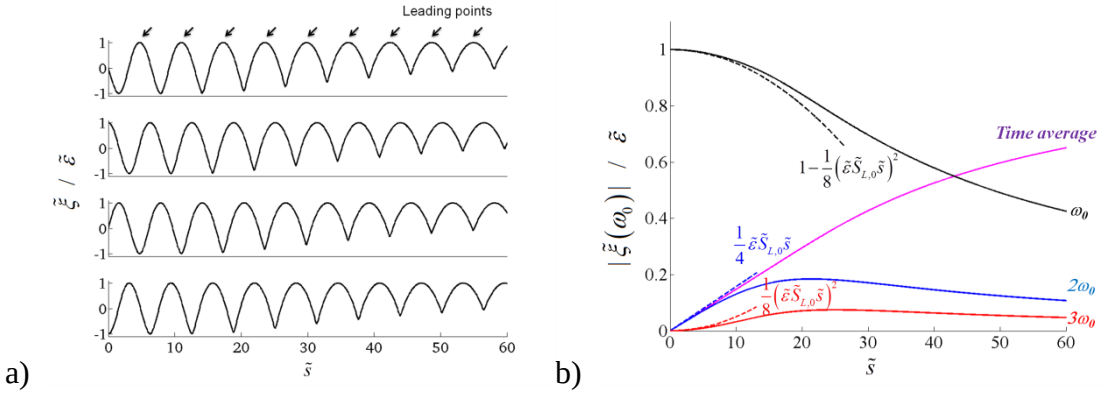

a) b)

Figure 6.4. a) Instantaneous computed flame front position, $\tilde{\xi}$, at four instances during a forcing period. b) Fourier coefficients of a flame front from the numerical solution (solid) and corresponding asymptotic solutions (dashed). Conditions are $\tilde{S}_{L,0}$ =0.1, $\tilde{\varepsilon}$ =0.63, $\tilde{\sigma}$ =0.

The asymptotic solutions for the flame position are given by:

$$\tilde{\xi}_{\varepsilon\varepsilon} = \frac{1}{4}\cdot\tilde{S}_{L,0}\cdot\left[\tilde{s}-\tilde{s}\cdot\cos\left(2\left(\tilde{t}-\tilde{s}\right)\right)\right]$$
$$\tilde{\xi}_{\varepsilon\varepsilon\varepsilon} = -\frac{1}{8}\cdot\tilde{S}_{L,0}{}^2\cdot\left[\tilde{s}^2\cos\left(\tilde{t}-\tilde{s}\right)-3\tilde{s}\sin\left(\tilde{t}-\tilde{s}\right)-\tilde{s}^2\cos\left(3\left(\tilde{t}-\tilde{s}\right)\right)+\tilde{s}\sin\left(3\left(\tilde{t}-\tilde{s}\right)\right)\right] \quad (6.14)$$

These solutions are also drawn into Figure 6.4b, where it can be seen that they closely follow the exact solution in the bluff body near field but diverge with downstream

distance. Thus, the asymptotic results are useful for analyzing the near field influence of kinematic restoration.

We next consider the amplitude dependence of the flame response at the forcing frequency. The asymptotic behavior of the flame response at the forcing frequency can be extracted from Eqs. (6.13) and (6.14) as:

$$\left|\tilde{\xi}\left(\omega=\omega_0\right)\right|/\,\tilde{\varepsilon}=1-\left(\tilde{\varepsilon}\tilde{S}_{L,0}\tilde{s}\right)^2/8+O\left(\tilde{\varepsilon}^3\right) \tag{6.15}$$

This solution shows that the leading order correction to the flame position scales as $\left(\tilde{\varepsilon}\tilde{S}_{L,0}\tilde{s}\right)^2$. The parameter, $\tilde{\varepsilon}\tilde{S}_{L,0}\tilde{s}$, indicates that the kinematic restoration effect is a quadratic function of disturbance amplitude, flame speed, and downstream distance. Note that this same parameter also naturally appears in calculations of, for example, cusp formation time, $\tilde{\varepsilon}\tilde{S}_{L,0}\tilde{t}=1$, in temporally evolving initial value problems where downstream distance is replaced with time [37].

Equation (6.15) can also be manipulated to show that the axial rate of decay in flame wrinkle size is given by:

$$\frac{d\left|\tilde{\xi}\left(\omega=\omega_0\right)\right|}{d\tilde{s}}=-\frac{\tilde{\varepsilon}^3\tilde{S}_{L,0}{}^2}{4}\tilde{s}+O\left(\tilde{\varepsilon}^4\right) \tag{6.16}$$

which can also be written in the following form which explicitly illustrates the nonlinear amplitude dependence of the wrinkle destruction rate:

$$\frac{d\left|\tilde{\xi}\left(\omega=\omega_0\right)\right|}{d\tilde{s}}=-\frac{\tilde{S}_{L,0}{}^2}{4}\left|\tilde{\xi}\left(\omega=\omega_0\right)\right|^3\tilde{s}+O\left(\tilde{\varepsilon}^4\right) \tag{6.17}$$

Insight into the flame dynamics farther downstream, where the asymptotic expressions in Eqs. (6.16) and (6.17) break down, can be obtained by expanding the

solution around its exact value at some nonzero $\tilde{s} = \tilde{s}'$ value. To see this, write the exact solution for the flame position at $\tilde{s} = \tilde{s}'$ as:

$$\tilde{\xi}(\tilde{s}', t) = \varepsilon \cdot \sum_{n=1}^{\infty} a_n \cos(n\omega_0 t) + b_n \sin(n\omega_0 t) \tag{6.18}$$

Without loss of generality, we can set b_1 =0 (which is equivalent to shifting the time coordinate) and, by following a similar perturbation procedure as outlined in Eqs. (6.10) and (6.11) (see APPENDIX G for detailed solution), we obtain:

$$\frac{|\tilde{\xi}(\tilde{s}, \omega_0)|}{\tilde{\varepsilon}} = a_1 + \frac{\tilde{\varepsilon}\tilde{S}_{L,0}\tilde{s}}{2} \sum_{n=1}^{\infty} n(n+1) \cdot (a_n a_{n+1} + b_n b_{n+1}) + O(\tilde{\varepsilon}^2) \tag{6.19}$$

The rate of change of the flame response can be obtained by differentiating Eq. (6.19) with respect to $\tilde{s}$. The expression for flame wrinkle magnitude is:

$$\frac{d\,|\tilde{\xi}(\tilde{s}, \omega_0)|}{d\tilde{s}} \approx \frac{\tilde{S}_{L,0}}{2} \sum_{n=1}^{\infty} n(n+1) \cdot \left|\tilde{\xi}(\tilde{s}, n\omega_0) \cdot \tilde{\xi}(\tilde{s}, (n+1)\omega_0)\right| \cos(\phi_n - \phi_{n+1} + \phi_1) \tag{6.20}$$

where ϕ_n is the phase of $\tilde{\xi}(\tilde{s}, n\omega_0)$.

A key difference between Eq. (6.15) and Eq. (6.19) is the presence of a term that is *linear* in $\tilde{s}$. This term is non-zero if the flame sheet contains oscillations at two frequencies, such as the forcing frequency and its harmonic. In contrast, $|\tilde{\xi}|$ only decays quadratically in $\tilde{s}$ if a single frequency component is present. This explains the slow initial decay of the flame response in Figure 6.4b. This result also shows the importance of the presence of harmonic content in the forcing signal, as it changes the axial decay rate from $O(\tilde{s}^2)$ to $O(\tilde{s})$. Given that unstable combustors generally have oscillations at multiple frequencies associated with different natural combustor modes, this analysis shows that the nonlinear interactions of these different frequencies on the flame sheet can have very important influences on its dynamics.

Having considered some basic features of the flame response, we next consider its amplitude dependence more explicitly. Figure 6.5a plots the magnitude of $\tilde{\xi}(\omega_0)$ as a function of scaled axial location for five different forcing amplitudes. The nonlinear character of the kinematic restoration process is clearly evident in this figure, as it shows the faster decay in flame wrinkling magnitude with increasing $\tilde{\varepsilon}$. This result can be expected from Eq. (6.15). Also interesting to note is the convergence of the unscaled $\tilde{\xi}(\omega_0)$ results to the same curve for large $\tilde{s}$, irrespective of initial forcing amplitudes. This behavior is a manifestation of the two-zone structure of kinematic restoration processes and is discussed further next. This result reflects the fact that at a sufficiently large distance downstream, the flame position is completely controlled by the leading points on the flame, indicated in Figure 6.4a. In other words, while the flame near field behavior is controlled by flame wrinkling wavelength and amplitude, the far field behavior is only a function of wrinkling wavelength. The reasons for this behavior are discussed in APPENDIX C, which also presents an approximate analysis showing that the flame wrinkling amplitude converges to the following result, which is independent of forcing amplitude:

$$\left|\tilde{\xi}(\tilde{s},\omega_0)\right| = \frac{2}{\tilde{S}_{L,0}\tilde{s}} \tag{6.21}$$

This expression can be rearranged to show:

$$\frac{d\left|\tilde{\xi}(\tilde{s},\omega_0)\right|}{d\tilde{s}} = -\frac{\tilde{S}_{L,0}}{2}\left|\tilde{\xi}(\tilde{s},\omega_0)\right|^2 \tag{6.22}$$

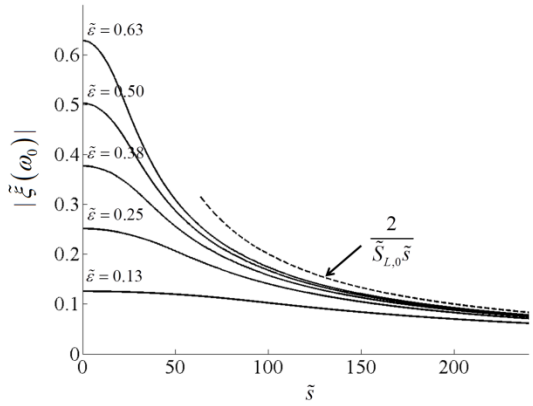

Figure 6.5. Computed dependence of flame position magnitude on downstream distance at different excitation amplitudes. ($\tilde{S}_{L,0}$=0.1 and $\tilde{\sigma}$=0).

This two-zone structure of kinematic restoration processes, and their different amplitude sensitivities, provides insights into the experimental data shown in Figure 2.7b. Downstream of the peak, all four different forcing amplitudes decay, with the highest amplitude decaying the fastest. Farther downstream, however, the curves converge towards a common asymptotic solution.

Finally, we note that all of the above results, whether in the near- or far field, show that kinematic restoration effects can be parameterized by the two quantities, $\tilde{\xi}(\tilde{s},\omega_0)/\tilde{\varepsilon}$ and $\tilde{\varepsilon}\tilde{S}_{L,0}\tilde{s}$. In order to illustrate the adequacy of this scaling, Figure 6.6 replots the calculation in Figure 6.5 using these two parameters. Note how all the different amplitudes converge to what is nearly a common line, with the largest deviations observed around $\tilde{\varepsilon}\tilde{S}_{L,0}\tilde{s} = 3$.

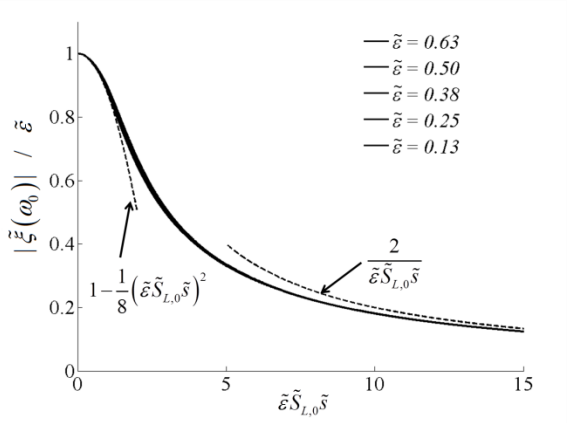

Figure 6.6. Results from Figure 6.5 replotted in scaled form.

6.3.2 Flame Stretch Effects

This section presents results illustrating the role of flame stretch in dissipating flame wrinkles. An exact linearized expression for $\tilde{\xi}$ is obtained by solving the linearized form of Eq. (6.9):

$$\frac{\tilde{\xi}\left(\tilde{s},\tilde{t}\right)}{\tilde{\varepsilon}} = Real\left\{ i \cdot \exp\left(\frac{1-\sqrt{1-i4\tilde{\sigma}\tilde{S}_{L,0}}}{2\tilde{\sigma}\tilde{S}_{L,0}}\,\tilde{s} - i\,\tilde{t} \right) \right\} \tag{6.23}$$

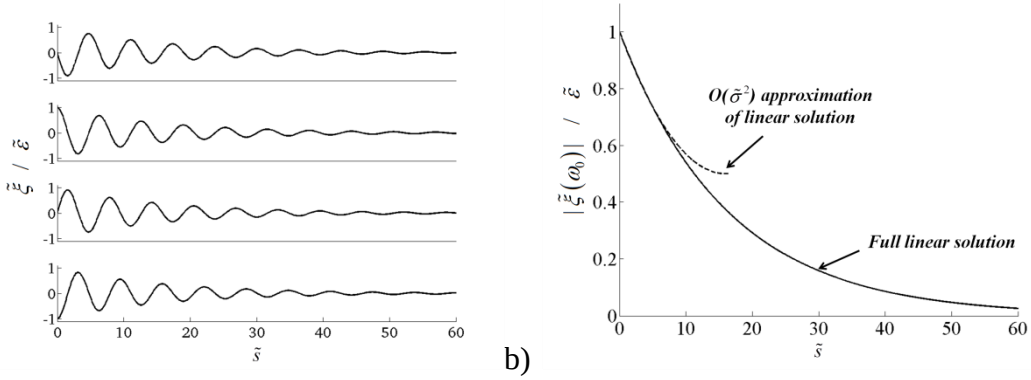

a) b)

Figure 6.7. a) Instantaneous flame front position, $\tilde{\xi}$, at four instances during a forcing period. b) Fourier coefficient of a flame front. (conditions: $\tilde{S}_{L,0}$ =0.1, $\tilde{\sigma}$ =0.63).

Figure 6.7a plots the spatial variation in the flame position at four instances during a forcing period. The plot clearly shows the dissipation of wrinkles with downstream distance. However, there are distinct differences between this result and Figure 6.4a. In this case, the flame wrinkles dissipate symmetrically about zero and the flame retains a smoothly varying slope with axial position. The magnitude of flame wrinkling as a function of axial distance at the forcing frequency is quantified in Figure 6.7b, showing a similar result - namely the asymptotic decay of flame wrinkling with downstream distance.

When Eq. (6.23) is expanded out in powers of $\tilde{\sigma}$, the solution is consistent with the results of the asymptotic expansion introduced in Eq. (6.10):

$$\begin{aligned} \tilde{\xi}_{\varepsilon\sigma} &= -\tilde{S}_{L,0}\tilde{s}\cdot\cos\left(\tilde{t}-\tilde{s}\right) \\ \tilde{\xi}_{\varepsilon\sigma\sigma} &= \tilde{S}_{L,0}{}^{2}\left[\frac{1}{2}\tilde{s}^{2}\cdot\cos\left(\tilde{t}-\tilde{s}\right)-2\tilde{s}\cdot\sin\left(\tilde{t}-\tilde{s}\right)\right] \end{aligned} \tag{6.24}$$

This solution is indicated in Figure 6.7b. A better approximation of Eq. (6.23), which also works for larger $\tilde{s}$ values, can be obtained by expanding the argument, but maintaining the structure of the exponential function:

$$\left|\tilde{\xi}\left(\tilde{s},\omega_0\right)\right|\Big/\varepsilon \approx \exp\left(-\tilde{\sigma}\tilde{S}_{L,0}\tilde{s}\right) \tag{6.25}$$

This equation indicates that stretch effects cause an exponential decay of flame wrinkles, with a rate given by $\tilde{\sigma}\tilde{S}_{L,0}\tilde{s}$, showing the faster destruction of flame wrinkles with increasing Markstein length values. Also, the exponential dependence indicates that the decay rate is proportional to the local magnitude of the flame response, which can be expressed for the general n^{th} harmonic of the forcing frequency as:

$$\frac{d\left|\tilde{\xi}\left(\tilde{s},n\omega_0\right)\right|}{d\tilde{s}} \approx -n\tilde{\sigma}\tilde{S}_{L,0}\left|\tilde{\xi}\left(\tilde{s},n\omega_0\right)\right| \qquad for \quad n=1,2,3,\cdots \tag{6.26}$$

This result will be returned to in analyzing coupled effects of stretch and kinematic restoration in the next section.

6.3.3 Stretch-Kinematic Restoration Coupling

The two previous sections have analyzed stretch and kinematic restoration effects in isolation. This section considers their coupled effects. Figure 6.8a presents a typical computed result showing four instantaneous flame locations when both effects are present. A key difference from the "kinematic restoration only" results is the smoothing out of the flame cusps by stretch effects. Figure 6.8b shows the flame response at the corresponding frequencies. It shows the decay of the response at ω_0 and slight increase of the mean flame position, as well as the excitation of higher harmonics.

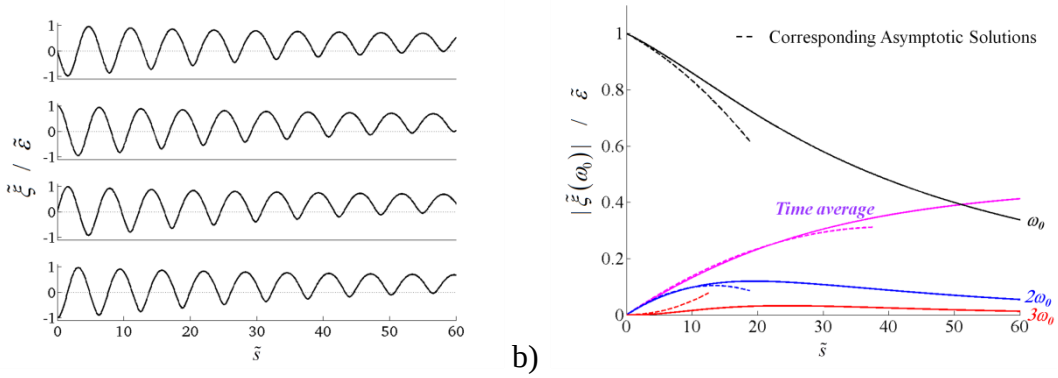

Figure 6.8. a) Instantaneous flame front position, $\tilde{\xi}$, at four instances during a forcing period from a numerical simulation. b) Fourier coefficients of flame front from a numerical solution and corresponding asymptotic solutions (conditions: $\tilde{S}_{L,0}$ =0.1, $\tilde{\varepsilon}$ =0.63, $\tilde{\sigma}$ =0.13).

An important result from the asymptotic analysis is that stretch and kinematic restoration effects are decoupled up to third order for the single frequency forcing case.

This can be seen from the perturbation solution for $\tilde{\xi}_{\varepsilon\varepsilon\sigma}$, which contains the only coupling term between the excitation and stretch:

$$\tilde{\xi}_{\varepsilon\varepsilon\sigma} = \tilde{S}_{L,0}{}^2 \cdot \left[-\frac{1}{4}\tilde{s}^2 - \frac{3}{2}\tilde{s}\sin\left(2\left(\tilde{t}-\tilde{s}\right)\right) + \frac{3}{4}\tilde{s}^2\cos\left(2\left(\tilde{t}-\tilde{s}\right)\right)\right] \tag{6.27}$$

In other words, coupling effects introduce corrections to the time-averaged flame response and harmonics, but not to the response at the forcing frequency itself, to this order of approximation. As a result, to this order, the decoupled flame response can be obtained from the linear sum of the flame responses associated with each isolated mechanism as:

$$\underbrace{1-\frac{|\tilde{\xi}(\tilde{\varepsilon},\tilde{\sigma},\tilde{s},\omega_0)|}{\tilde{\varepsilon}}}_{Decoupled\ Total\ Decay} = \underbrace{\left(1-\frac{|\tilde{\xi}(\tilde{\varepsilon},\tilde{\sigma},\tilde{s},\omega_0)|}{\tilde{\varepsilon}}\bigg|_{\tilde{\sigma}=0}\right)}_{Decay\ by\ Kinematic\ Restoration} + \underbrace{\left(1-\frac{|\tilde{\xi}(\tilde{\varepsilon},\tilde{\sigma},\tilde{s},\omega_0)|}{\tilde{\varepsilon}}\bigg|_{\tilde{\varepsilon}\sim 0}\right)}_{Decay\ by\ Flame\ Stretch} \tag{6.28}$$

However, this result is limited to the near field as the asymptotic solution in Eq. (6.27) quickly loses accuracy further downstream. A generalization of Eq. (6.19) that is valid at any spatial location and incorporates both effects is:

$$\frac{|\tilde{\xi}(\tilde{s},\omega_0)|}{\tilde{\varepsilon}} = a_1 + \frac{\tilde{\varepsilon}\tilde{S}_{L,0}\tilde{s}}{2}\sum_{n=1}^{\infty} n(n+1)\cdot\left(a_n a_{n+1} + b_n b_{n+1}\right) - \tilde{\sigma}\tilde{S}_{L,0}\tilde{s} + O\left(\tilde{\varepsilon}^2\right) \tag{6.29}$$

To further consider coupling effects, results are shown for three sets of parameter values in Figure 6.9a, b, and c, where kinematic restoration is dominant, flame stretch is dominant, and both effects are comparable, respectively. The solid black lines indicate the computed exact flame response and the two black dashed lines represent the flame response when the other mechanism is absent (i.e., results obtained from Section A and B). The red dashed lines indicate the linear superposition of the decoupled results, obtained from Eq. (6.28). Note the close correspondence between the decoupled solution and the exact solution in the near field, but their divergence further downstream.

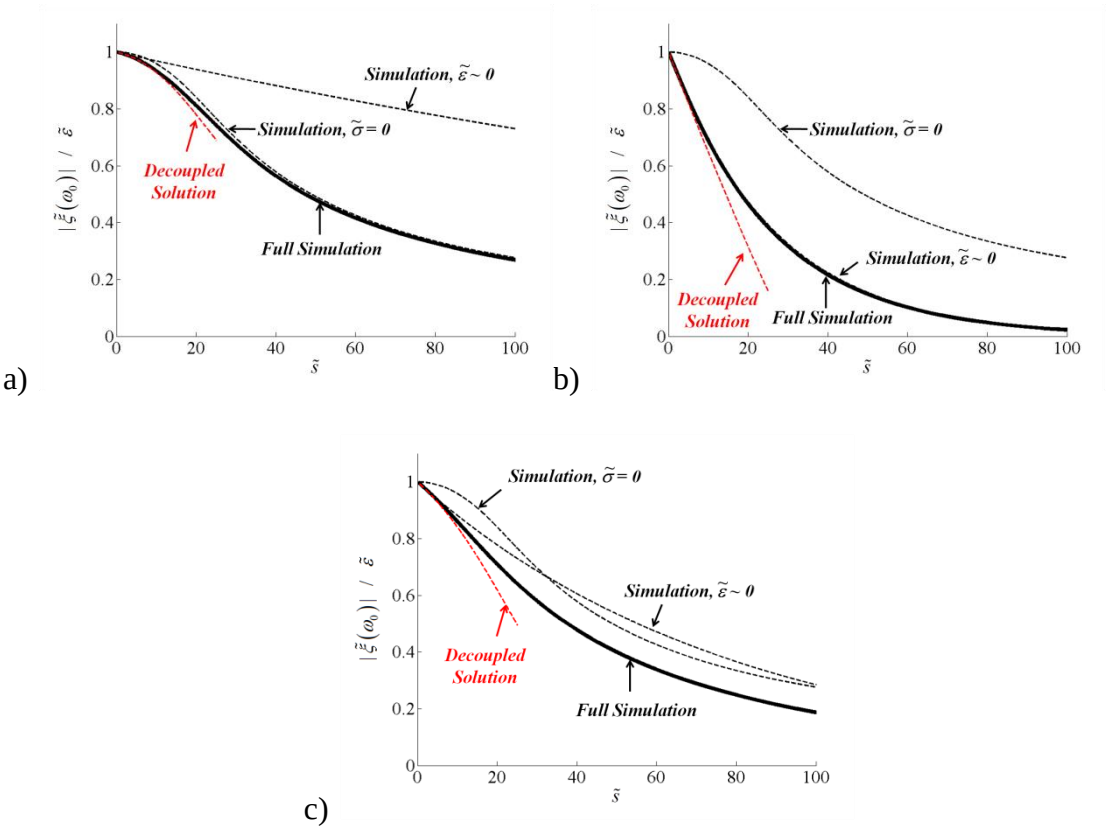

Figure 6.9. Gains of the flame responses at $\omega=\omega_0$ with full simulation, full simulation without kinematic restoration ($\tilde{\varepsilon}\sim 0$), full simulation without flame stretch ($\tilde{\sigma}=0$) and decoupled solution (i.e., using Eq. (6.28)) using values of $\tilde{S}_{L,0}=0.1$, $\tilde{\varepsilon}=0.63$, and (a) $\tilde{\sigma}=0.031$,(b) $\tilde{\sigma}=0.38$, and (c) $\tilde{\sigma}=0.13$.

Interestingly, both curves in Figure 6.9a and Figure 6.9b show that the exact solution converges to the solution obtained when only one effect is included in isolation. In other words, the result in Figure 6.9a converges to the $\tilde{\sigma}=0$ result, while in Figure 6.9b it converges to the $\tilde{\varepsilon}\sim 0$ result. Thus, this result shows that the decay in flame response is dominated by one mechanism in the far field - note that this does not occur in the near field. Only when both terms are of similar magnitude does the far field solution differ from both, as shown in Figure 6.9c.

The reasons for this behavior are different for the two limiting cases. For the stretch dominated flame response, stretch effects are increasingly efficient at smoothing out flame wrinkles associated with harmonics of the forcing frequency which are generated by nonlinearities associated with kinematic restoration effects, as can be seen from Eq. (6.29). However, as discussed in the context of Eq. (6.19), kinematic restoration effects are very weak in the absence of multiple interacting frequencies. For the kinematic restoration dominated case, flame stretch effects are locally very important at the trailing edge of the wrinkled flames. However, beyond just smoothing out this sharp cusp, stretch does little to decrease the amplitude of the flame wrinkle.

6.4 Discussion

6.4.1 Relative Significance of Kinematic Restoration and Stretch

In this section, we analyze the conditions under which flame wrinkle destruction is either negligible or nearly total, as well as the relative significance of kinematic restoration and stretch. Consider first the condition for negligible flame wrinkle destruction - i.e., the conditions under which both processes analyzed in this chapter are negligible.. We use a somewhat arbitrary threshold for this condition, defined as the point where the flame maintains 99% of its initial wrinkle. Using the perturbation analysis results from Eqs. (6.15) and (6.25) and noting that coupling effects are negligible, leads to the following condition:

$$\textit{Negligible Flame Wrinkle Destruction}\ \ (|\tilde{\xi}| > 0.99\tilde{\varepsilon}):$$
$$\frac{1}{8}\left(\tilde{\varepsilon}\tilde{S}_{L,0}\tilde{s}\right)^2 + \tilde{\sigma}\tilde{S}_{L,0}\tilde{s} < 0.01 \tag{6.30}$$

This line is indicated on the bottom left in Figure 6.10. We next consider the conditions under which the flame wrinkle is completely smoothed out. Again, we somewhat arbitrarily set the threshold for this point as the flame wrinkle amplitude dropping below 1% of its initial value. Thus, from Eqs. (6.21) and (6.25), we obtain:

$$\begin{aligned} &\textit{Flame Wrinkle Dissipated} \quad (|\tilde{\xi}| < 0.01\tilde{\varepsilon}): \\ &\qquad \tilde{\varepsilon}\tilde{S}_{L,0}\tilde{s} > 200 \quad \textit{or} \quad \tilde{\sigma}\tilde{S}_{L,0}\tilde{s} > ln(100) \end{aligned} \tag{6.31}$$

These two lines are also indicated in Figure 6.10.

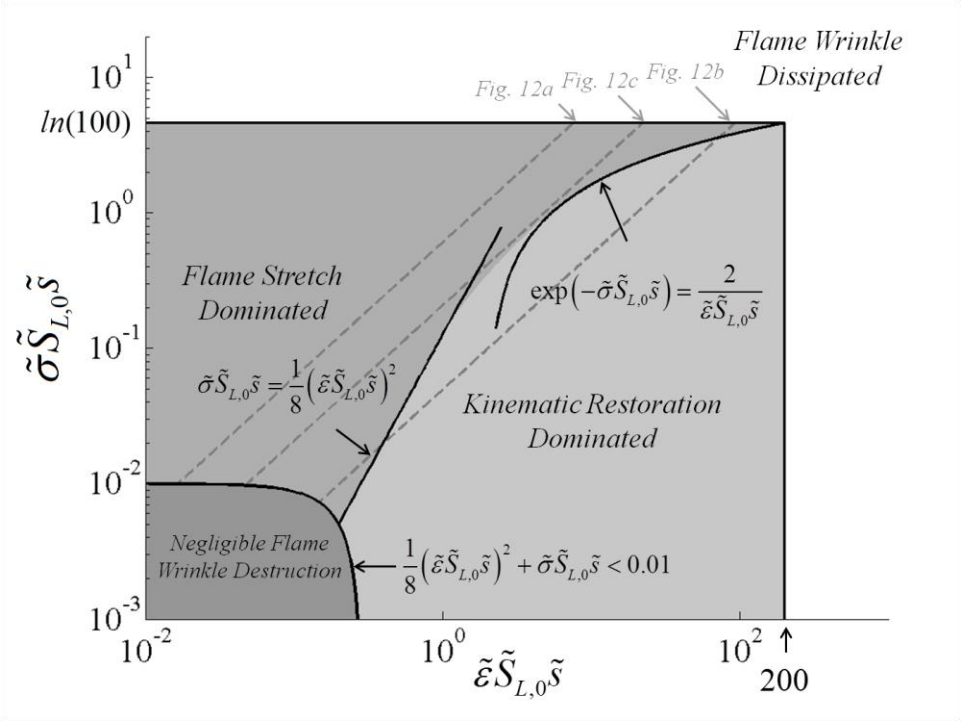

Figure 6.10. Summary of regions where flame wrinkle destruction is negligible, and when it is dominated by flame stretch or kinematic restoration.

We next consider the region between these two lines of negligible and near total dissipation of flame wrinkles. In this region, the important question is what is the dominant flame wrinkle dissipation process. Near the flame holder, coupling is negligible and the flame wrinkle amplitude given by:

$$\textit{Near Field}: \qquad \frac{\tilde{\xi}}{\tilde{\varepsilon}} = 1 - \frac{1}{8}\left(\tilde{\varepsilon}\tilde{S}_{L,0}\tilde{s}\right)^2 - \tilde{\sigma}\tilde{S}_{L,0}\tilde{s} \tag{6.32}$$

Equating the second and the third terms leads to following condition, also indicated by the line in Figure 6.10 that demarcates flame stretch vs. kinematic restoration dominated.

$$\frac{1}{8}\left(\tilde{\varepsilon}\tilde{S}_{L,0}\tilde{s}\right)^2 = \tilde{\sigma}\tilde{S}_{L,0}\tilde{s} \tag{6.33}$$

We next consider far downstream. As shown in Sec. 6.3.3, the flame response is dominated by one mechanism in this region. Thus, we can do a straightforward comparison of Eqs. (6.21) and (6.25) to obtain:

$$\textit{Far Field}: \quad \frac{\tilde{\xi}}{\tilde{\varepsilon}} = \begin{cases} \dfrac{2}{\tilde{\varepsilon}\tilde{S}_{L,0}\tilde{s}} & \textit{for} \quad \tilde{\sigma}\tilde{S}_{L,0}\tilde{s} << \ln\left(\tilde{\varepsilon}\tilde{S}_{L,0}\tilde{s}\right) \\ \exp\left(-\tilde{\sigma}\tilde{S}_{L,0}\tilde{s}\right) & \textit{for} \quad \tilde{\sigma}\tilde{S}_{L,0}\tilde{s} >> \ln\left(\tilde{\varepsilon}\tilde{S}_{L,0}\tilde{s}\right) \end{cases} \tag{6.34}$$

Equating these two expressions leads to:

$$\frac{2}{\tilde{\varepsilon}\tilde{S}_{L,0}\tilde{s}} = \exp\left(-\tilde{\sigma}\tilde{S}_{L,0}\tilde{s}\right) \tag{6.35}$$

which is also indicated in Figure 6.10. For reference, the points shown in Figure 6.9 are indicated as gray dashed lines in Figure 6.10. Thus, this figure provides a useful summary of conditions where wrinkles are negligibly or completed dissipated, as well as which mechanism is dominant.

6.4.2 Contributions of the Decay in the Bluff-Body Stabilized Flame

This section applies the analysis in Sec. 6.3 to bluff-body stabilized flames and quantifies the relative contributions of the flame stretch and the kinematic restoration effects in the decay of the flame response. The extended analysis in 6.3.1 and 6.3.2 indicates that the decay of the flame response is related with the local flame response, and Sec. 6.3.3 shows that the two mechanisms are decoupled up to the 3rd orders of the excitation amplitude (ε)

and Markstein length (σ). Equations (6.20) and (6.26) will be used to quantifies the individual contributions in the decay of the flame response.

Figure 6.11 shows the flame responses with harmonic frequencies. Harmonic contents are required because the kinematic restoration effect involves nonlinear interactions between fundamental and harmonic frequencies. In order to estimate the harmonic frequency contents, relative values of the spatial Fourier transform were used, which is described in the APPENDIX K. High harmonics contents ($\omega > 3\omega_0$) shown in Figure 6.11 seems to be higher than those of the laminar simulations shown in Figure K0.2b. This increased value in the high frequency is suspected to originate from the turbulent motion, whose influence is not quantified in APPENDIX K. All response are small near the flame holder (x/λ_0 = 0) and grow downstream, followed by the decrease after around x/λ_0 = 3.

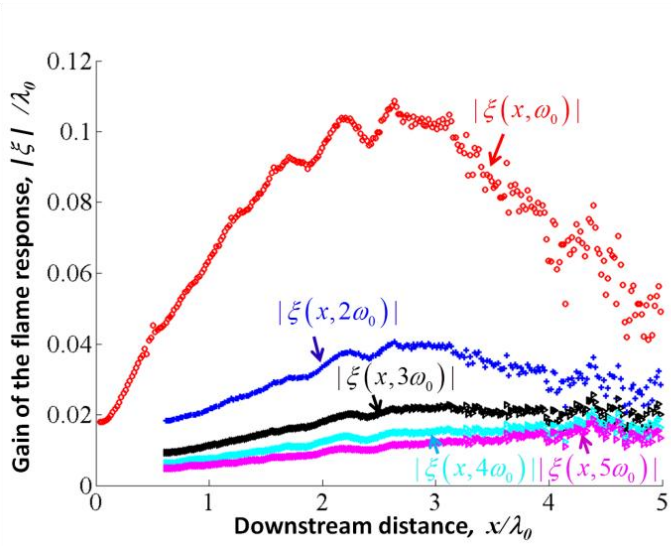

Figure 6.11. Dependence of flame front fluctuation spectrum, $|\xi(x,\omega)|/\lambda_0$ upon downstream distance. (u_0 = 2.27 m/s, f_0 = 200 Hz)

By applying Eqs. (6.20) and (6.26) from the results in Figure 6.11, the individual contributions to decay are estimated, and plotted in Figure 6.12. Different estimations are made for the kinematic restoration contribution because the suspiciously high values of high frequencies may cause over-prediction. These different estimations are done by adding different number of harmonics up to $4\omega_0$, as shown in Figure 6.12. As including more number of harmonic contents, the amount of the kinematic restoration contribution increases due to the positive summation. In this flame stretch contribution, the Markstein length is negative in this flame [95], meaning that the stretch effect excites the flame. In the near field, the actual change is quite different from the sum of flame stretch effect and the kinematic restoration because velocity fluctuation is significant in this region. This result also indicates that the kinematic restoration effect is stronger than the flame stretch effect in the entire region because of the small Markstein length and the high level of the harmonic contents as shown in Figure 6.11.

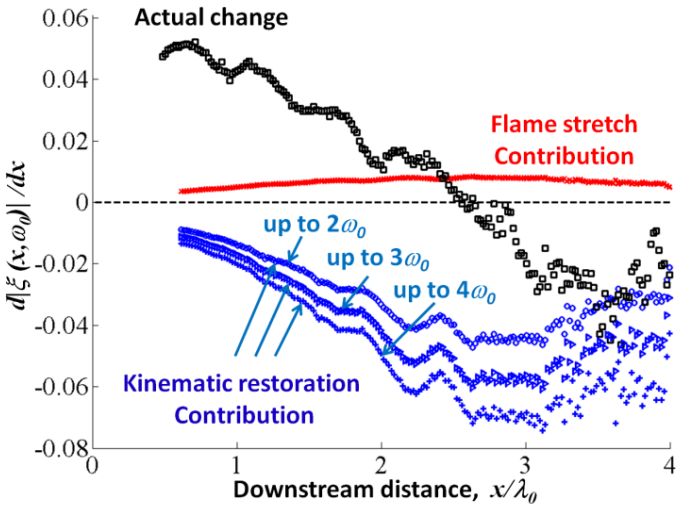

Figure 6.12. The rate of change of the flame response over the downstream distance, and the individual contributions from the flame stretch and the kinematic restoration. Conditions are same as the one shown in Figure 6.11.

The individual contributions shown in Figure 6.12 were added up cumulatively downstream in order to enable a comparison with the actual flame response, $|\xi(x,\omega_0)|$. This comparison was made starting from x=2.6λ_0 where the flame response starts to decrease. The regions upstream of this point are strongly influenced by the velocity fluctuations and were covered in CHAPTER 4 and CHAPTER 5. Figure 6.13 depicts the comparison between the actual flame response and the estimated flame responses. Different estimation was plotted by considering different number of harmonic content. They show good agreement with the estimation considering up to $2\omega_0$. This also indicates that the higher harmonic contents are over-estimated by the spatial Fourier transform. Since the kinematic restoration is the leading order effect in the decay, the estimated $|\xi(x,\omega_0)|$ also follows the trend of the kinematic restoration shown in Figure 6.12 – the estimated $|\xi(x,\omega_0)|$ has a sharp decrease near x=2.6λ_0, followed by its decay slowing down further downstream. Relative magnitudes shown in Figure 6.13 indicate that the decay in the far field is mainly driven by the kinematic restoration.

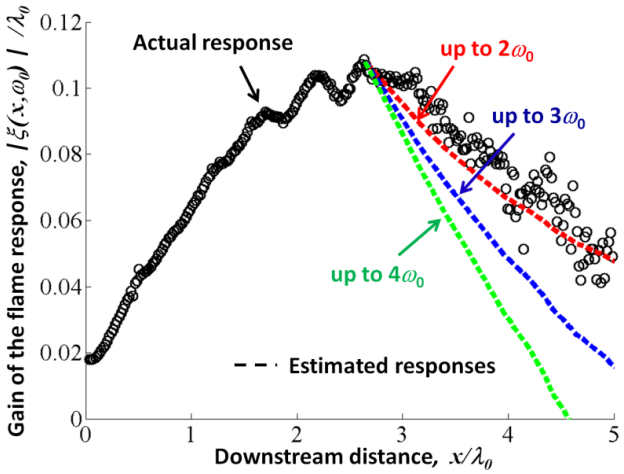

Figure 6.13. Comparison of the actual flame response and the estimated flame response by the kinematic restoration and the flame stretch. The estimation is done using Eqs. (6.20) and (6.26) . Conditions are same as the one shown in Figure 6.11.

CHAPTER 7

FLAME RESPONSE IN THE DECAYING DISTURBANCE FIELD – TURBULENT EFFECT VS. KINEMATIC RESTORATION

This chapter describes analyses of the nonlinear dynamics of harmonically forced, turbulent premixed flames. A key objective of this work is to analyze the relative contributions of deterministic and turbulent effects upon the ensemble averaged dynamics of the flame front position, $<\xi>$, with particular focus on the rate at which wrinkles excited by harmonic forcing are smoothed out and destroyed. This is done by forcing an anchored premixed flame with harmonic and stochastic oscillations, parameterized by the amplitudes, ε and μ, respectively. Low amplitude and/or near field effects are quantified by a third order perturbation analysis, while the more general case is analyzed computationally by solving the three-dimensional level set equation over long time intervals, and ensemble averaging the results. We show that different mechanisms contribute to smoothing in flame wrinkles, manifested as progress decay in the magnitude of $<\xi>$. Near the flame holder, random phase jitter effects dominate the smoothing of $<\xi>/\varepsilon$, scaling as $-\omega_0^{\,2}\mu^2 s^2 / 2u_{s,0}^{\,4}$, where ω_0, $u_{s,0}$, and s denote the radial forcing frequency, mean tangential velocity, and downstream distance, respectively. In addition, random modulation of the flame angle at the separation point and destruction of flame wrinkles by turbulent eddies also contribute, scaling as $-\omega_0^{\,2}\mu^2 S_L^{\,2} s^2 / 2u_{s,0}^{\,6}$ and $-5\pi\omega_0^{\,2}\mu^2 S_L^{\,2} s^4 / 48u_{s,0}^{\,6} L_{11}^{\,2}$, where S_L and L_{11} denote the laminar flame speed and longitudinal length scale. Farther downstream, two additional processes become

important. The first is the rise in time averaged turbulent burning velocity with μ, as expected. A second, new result is the demonstration that the ensemble averaged turbulent burning velocity is modulated by the harmonic forcing, with an inverse dependence upon ensemble averaged flame curvature. This effect is exactly analogous to positive Markstein length flames in the laminar flame case, but applies even to the ensemble averaged characteristics of stretch-insensitive turbulent flames. This result is shown to follow from basic geometry reasoning of flames with positive and negative curvatures. We show that, depending upon turbulence intensity, the far field evolution of $<\xi>$ can be dominated by either the $\overline{S_{T,eff}}$ or $S_{T,eff}{}'$, which lead to a quadratic and linear decay in $<\xi>$with s, respectively.

We consider stretch-free flame dynamics in flows with both harmonic and turbulent flow components. These disturbances nonlinearly interact and introduce new effects [55]. For example, both deterministic and stochastic processes contribute to smoothing of the ensemble averaged harmonic flame wrinkle [23, 87]. We will show in this chapter that this occurs through both stochastic kinematic restoration and phase jitter effects which do not average to zero.

To illustrate the problem of interest, Figure 7.1 illustrates experimental Mie scattering images of a harmonically excited, turbulent Bunsen flame, illustrating the simultaneous presence of the coherent and broadband wrinkling on the flame front. The four instantaneous images on the left show significant turbulent wrinkling of the flame front. The right figure overlays a number of flame edges extracted from these instantaneous images at the same phase, clearly showing the coherent wrinkling on the flame induced by the harmonic forcing. This coupling between harmonic and stochastic

processes on turbulent flames is not well understood [12, 96, 97]. The specific objective of this work is to analyze this problem and determine the interactions and relative significance of the deterministic and stochastic components of this problem in controlling the dynamics of harmonically excited flame wrinkles, such as their decay rate.

a) 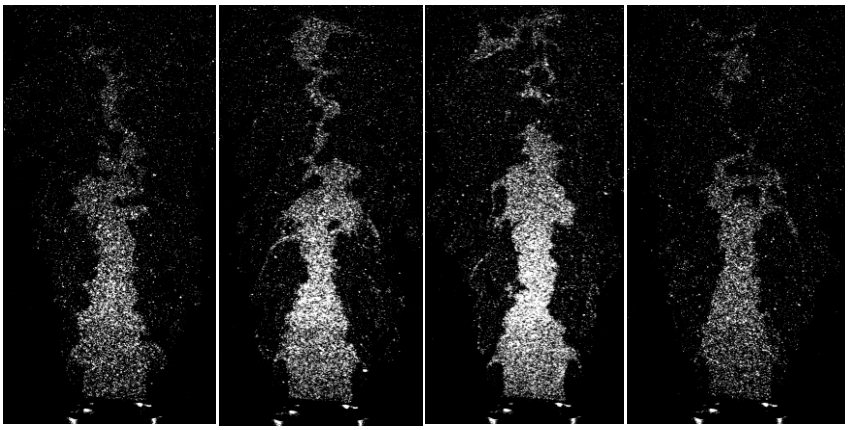 b) 

Figure 7.1. (a) Four instantaneous phase-locked Mie scattering images from a turbulent propane Bunsen flame excited by a longitudinal acoustic disturbance (b) Overlay of instantaneous flame edges showing flame brush and coherent wrinkling on the flame induced by the harmonic forcing [98].

7.1 Formulation

In this section we consider a harmonically oscillating flame holder, emulating the experimental study of Petersen and Emmons [36] shown in Figure 7.2, , in the presence of a stochastically oscillatory background flow. This is a useful problem for this study as the amplitude of flame wrinkling, within a stretch-free and linear analysis framework, is constant with axial location; i.e., $|\xi(x,\omega_0)|=|\xi(x=0,\omega_0)|$. In contrast, the harmonic velocity-forced flame has a spatially modulated flame wrinkling character, as shown in Figure 2.7, leading to a complex modulation of nonlinear processes [23, 99, 100]. This

oscillating flame holder problem allows us to develop relatively simple expressions for the key dimensionless parameters controlling the problem, and thus, to isolate the critical processes controlling the far field evolution of harmonically forced flames.

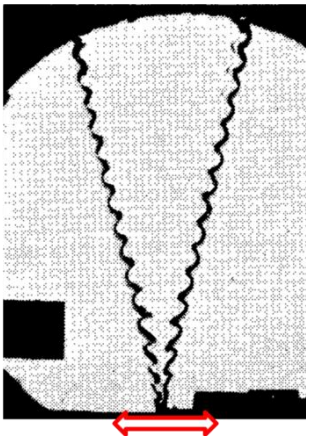

Figure 7.2. Visualization of a propane flame stabilized on a transversely oscillating flame holder at 625 Hz (ϕ = 1, $u_{x,0}$ = 4.8 m/s) [36].

The investigated geometry is shown in Figure 7.3. The coordinate system is aligned with the unperturbed flame position, so that the *s* and *n* coordinates are tangential and normal to the unperturbed flame, with the *z* coordinate pointing in the third orthogonal direction out of the page. The flow field is prescribed and the flame holder vibrates in the *n*-direction, creating wrinkles on the flame at *s* =0 which propagate downstream.

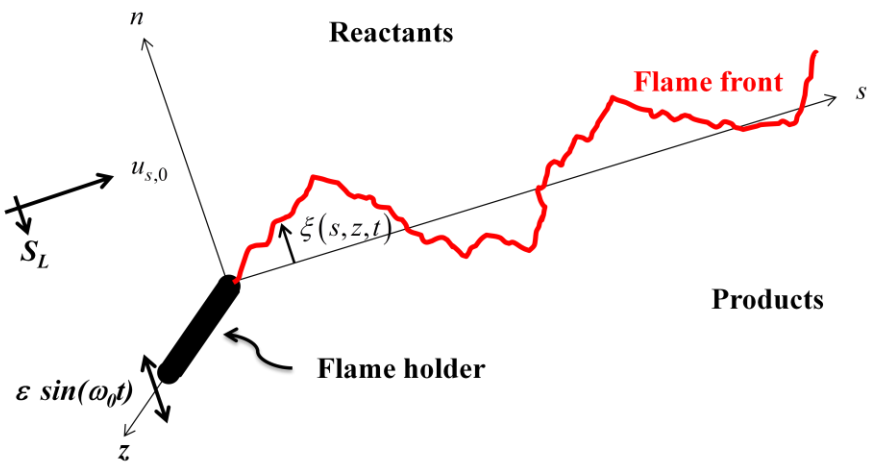

Figure 7.3. Diagram of flame/flow configuration and the coordinates (ξ: flame front location).

The principal assumptions made in this analysis are that: (i) the flame is a thin, two-dimensional interface, dividing reactants and products, (ii) the stochastic velocity fluctuations (u_s, u_n, u_z) are prescribed, (iii) the flame speed, S_L, is constant, (iv) the flame remains attached to the flame holder. Then, the instantaneous location of the flame front is determined from the *G*-equation [28], and *(s,n,z)*-coordinate version of Eq. (2.3) is:

$$\frac{\partial G}{\partial t} + u_s \frac{\partial G}{\partial s} + u_n \frac{\partial G}{\partial n} + u_z \frac{\partial G}{\partial z} = S_L \left[\left(\frac{\partial G}{\partial s} \right)^2 + \left(\frac{\partial G}{\partial n} \right)^2 + \left(\frac{\partial G}{\partial z} \right)^2 \right]^{1/2} \tag{7.1}$$

For small velocity fluctuations, the flame front position is single-valued, an approximation that breaks down at high amplitude fluctuations. In this low amplitude excitation case, a substitution, $G=n-\xi(s,z,t)$ leads to the following equation for the flame position, $\xi(s,z,t)$:

$$\frac{\partial \xi}{\partial t} + u_s \frac{\partial \xi}{\partial s} - u_n + u_z \frac{\partial \xi}{\partial z} = S_L \left[1 + \left(\frac{\partial \xi}{\partial s} \right)^2 + \left(\frac{\partial \xi}{\partial z} \right)^2 \right]^{1/2} \tag{7.2}$$

The velocity field shown in Figure 7.3 is written as mean and perturbation quantities as:

$$\begin{aligned} u_s &= u_{s,0} + \mu \cdot f_s(s,n,z,t)\big|_{n=\xi} \\ u_n &= -S_L + \mu \cdot f_n(s,n,z,t)\big|_{n=\xi} \\ u_z &= \mu \cdot f_z(s,n,z,t)\big|_{n=\xi} \end{aligned} \tag{7.3}$$

where μ and f_i denote the magnitude of the velocity fluctuation and the shape function, respectively. The turbulence intensity is $\sqrt{3}\mu$ with $\left\langle f_i^2 \right\rangle = 1$. Note that the velocity is prescribed *a priori*. The mean velocity of u_n is $-S_L$ because the unforced flame aligns with the *s*-coordinate. Note that this assumption is rigorously valid in the limit of an iso-density flow, but neglects the influence that a finite density change across the flame has on the approach flow, as the oscillatory flame sheet would otherwise induce an oscillatory approach flow. Because of the mutual interaction between the flame position and the flow field, free boundary problems such as this are otherwise difficult to handle analytically. This issue has been discussed by a number of prior workers [22, 90, 101-103].

With the velocity expression in Eq. (6.3), the single-valued flame dynamics equation in Eq. (6.2) is rewritten as:

$$\frac{\partial \xi}{\partial t} + u_{s,0}\frac{\partial \xi}{\partial s} = \underbrace{S_L\left\{\left[1+\left(\frac{\partial \xi}{\partial s}\right)^2+\left(\frac{\partial \xi}{\partial z}\right)^2\right]^{1/2}-1\right\}}_{Kinematic\ restoration} + \underbrace{\mu\cdot\left[-f_s\frac{\partial \xi}{\partial s}+f_n-f_z\frac{\partial \xi}{\partial z}\right]}_{Turbulent\ flow\ forcing} \tag{7.4}$$

Here, the first and the second terms on the RHS describe changes to the convecting flame wrinkle, $\xi\left(t-s/u_{s,0}\right)$, through kinematic restoration and turbulent flow forcing,

respectively. Because of nonlinearities associated with convection (e.g., $f_s \partial\xi / \partial s$) and kinematic restoration (e.g., $\left[1+\left(\partial\xi/\partial s\right)^2+\left(\partial\xi/\partial z\right)^2\right]^{1/2}$), these two terms interact.

Two boundary conditions are needed. First, it is assumed that the flame is attached to the flame holder which oscillates in the *n*-direction as:

$$\xi\left(s=0,z,t\right)=\varepsilon\cdot\sin\left(\omega_0 t\right) \tag{7.5}$$

where ε and ω_0 denote the magnitude and angular frequency of the flame holder oscillation, respectively. Second, a nonreflecting boundary condition is applied at the downstream end of the calculation domain, so that information only propagates along the flame in the flow direction.

The stochastic flow fluctuations in Eq. (7.3) are assumed to be (i) isotropic, (ii) Gaussian distributed, (iii) propagating with the flow as per Taylor's hypothesis, and (iv) have Eulerian space/time correlations that decay exponentially over a longitudinal length scale, L_{11} as [53, 54]:

$$\left\langle f_s\left(s,n,z,t\right)\cdot f_s\left(s+r,n,z,t\right)\right\rangle=\exp\left(-\frac{\pi}{4}\left(\frac{r}{L_{11}}\right)^2\right) \tag{7.6}$$

The Taylor's hypothesis with the specified velocities in Eq. (6.3) implies:

$$f_i\left(s,n,z,t+\Delta t\right)=f_i\left(s-u_{s,0}\Delta t,n+S_L\Delta t,z,t\right)\qquad \textit{for } i=s,n,z \tag{7.7}$$

Based on Eqs. (7.6) and (7.7), all two point correlations can be derived from isotropy relations [104] as listed in APPENDIX . For Gaussian random variables, all higher order correlations can be derived from sum and products of two point correlations and all odd order correlations are zero [105, 106]. Lastly, the following non-dimensionalization scheme is used for simplification:

$$
\begin{aligned}
&\tilde{s} = s/\left(u_{s,0}/\omega_0\right), \quad \tilde{z} = z/\left(u_{s,0}/\omega_0\right), \qquad \tilde{n} = n/\left(u_{s,0}/\omega_0\right), \\
&\tilde{\xi} = \xi/\left(u_{s,0}/\omega_0\right), \quad \tilde{L}_{11} = L_{11}/\left(u_{s,0}/\omega_0\right), \quad \tilde{\varepsilon} = \varepsilon/\left(u_{s,0}/\omega_0\right), \\
&\tilde{t} = \omega_0 t, \quad \tilde{S}_L = S_L/u_{s,0}, \qquad \tilde{\mu} = \mu/u_{s,0}
\end{aligned}
\tag{7.8}
$$

The solutions to the full *G*-equation in Eq. (3.1) are analyzed computationally. Solutions of the single-valued ξ-equation in Eq. (7.4) are analyzed asymptotically. This asymptotic analysis is performed up to third order in the oscillating amplitude, $\tilde{\varepsilon}$, and the turbulence intensity, $\tilde{\mu}$. The computational procedure is described in Sec. 3.4.2.

7.2 Asymptotic Analysis

Asymptotic analyses of the governing equations were performed to obtain insight into key parameters controlling the flame wrinkle decay rate. Since the objective of this analysis is to analyze nonlinear corrections to the flame response at the forcing frequency, the analysis must be obtained up to the third order in $\tilde{\varepsilon}$ and $\tilde{\mu}$. The flame position, $\tilde{\xi}$, is expanded using the following two parameter expansion in harmonic excitation amplitude, $\tilde{\varepsilon}$, and turbulence intensity, $\tilde{\mu}$, as:

$$
\begin{aligned}
\tilde{\xi}\left(\tilde{s},\tilde{z},\tilde{t}\right) = \;& \tilde{\varepsilon}\cdot\tilde{\xi}_{\varepsilon}\left(\tilde{s},\tilde{z},\tilde{t}\right) + \tilde{\mu}\cdot\tilde{\xi}_{\mu}\left(\tilde{s},\tilde{z},\tilde{t}\right) \\
&+ \tilde{\varepsilon}^2\cdot\tilde{\xi}_{\varepsilon\varepsilon}\left(\tilde{s},\tilde{z},\tilde{t}\right) + \tilde{\varepsilon}\tilde{\mu}\cdot\tilde{\xi}_{\varepsilon\mu}\left(\tilde{s},\tilde{z},\tilde{t}\right) + \tilde{\mu}^2\cdot\tilde{\xi}_{\mu\mu}\left(\tilde{s},\tilde{z},\tilde{t}\right) \\
&+ \tilde{\varepsilon}^3\cdot\tilde{\xi}_{\varepsilon\varepsilon\varepsilon}\left(\tilde{s},\tilde{z},\tilde{t}\right) + \tilde{\varepsilon}^2\tilde{\mu}\cdot\tilde{\xi}_{\varepsilon\varepsilon\mu}\left(\tilde{s},\tilde{z},\tilde{t}\right) + \tilde{\varepsilon}\tilde{\mu}^2\cdot\xi_{\varepsilon\mu\mu}\left(\tilde{s},\tilde{z},\tilde{t}\right) + \tilde{\mu}^3\cdot\tilde{\xi}_{\mu\mu\mu}\left(\tilde{s},\tilde{z},\tilde{t}\right) \\
&+ O\left(\left(\tilde{\varepsilon},\tilde{\mu}\right)^4\right)
\end{aligned}
\tag{7.9}
$$

The corresponding boundary conditions for each function are:

$$
\tilde{\xi}_{\Theta}\left(\tilde{s}=0,\tilde{z},\tilde{t}\right) = \begin{cases} \sin\left(\tilde{t}\right) & \Theta = \varepsilon \\ 0 & \textit{otherwise} \end{cases}
\tag{7.10}
$$

After inserting the expansion in Eq. (7.9) into Eq. (7.4) and matching terms with the same order, we obtain a series of partial differential equations for each function, $\tilde{\xi}_{\Theta}$ (see APPENDIX F). For example, the equation for $\tilde{\xi}_{\varepsilon\mu\mu}$ is:

$$\begin{aligned}
&\frac{\partial \tilde{\xi}_{\varepsilon\mu\mu}}{\partial \tilde{t}} + \frac{\partial \tilde{\xi}_{\varepsilon\mu\mu}}{\partial \tilde{s}} = \tilde{S}_L \left(\frac{\partial \tilde{\xi}_{\mu}}{\partial \tilde{s}} \frac{\partial \tilde{\xi}_{\varepsilon\mu}}{\partial \tilde{s}} + \frac{\partial \tilde{\xi}_{\mu}}{\partial \tilde{z}} \frac{\partial \tilde{\xi}_{\varepsilon\mu}}{\partial \tilde{z}} + \frac{\partial \tilde{\xi}_{\varepsilon}}{\partial \tilde{s}} \frac{\partial \tilde{\xi}_{\mu\mu}}{\partial \tilde{s}} + \frac{\partial \tilde{\xi}_{\varepsilon}}{\partial \tilde{z}} \frac{\partial \tilde{\xi}_{\mu\mu}}{\partial \tilde{z}} \right) \\
&- f_s \frac{\partial \tilde{\xi}_{\varepsilon\mu}}{\partial \tilde{s}} - \frac{\partial f_z}{\partial \tilde{n}} \frac{\partial \tilde{\xi}_{\varepsilon}}{\partial \tilde{z}} \tilde{\xi}_{\mu} - \frac{\partial f_z}{\partial \tilde{n}} \frac{\partial \tilde{\xi}_{\mu}}{\partial \tilde{z}} \tilde{\xi}_{\varepsilon} - \frac{\partial f_s}{\partial \tilde{n}} \frac{\partial \tilde{\xi}_{\varepsilon}}{\partial \tilde{s}} \tilde{\xi}_{\mu} - \frac{\partial f_s}{\partial \tilde{n}} \frac{\partial \tilde{\xi}_{\mu}}{\partial \tilde{s}} \tilde{\xi}_{\varepsilon} \\
&- f_z \frac{\partial \tilde{\xi}_{\varepsilon\mu}}{\partial \tilde{z}} + \frac{\partial \tilde{f}_n}{\partial \tilde{n}} \tilde{\xi}_{\varepsilon\mu} + \frac{\partial^2 \tilde{f}_n}{\partial \tilde{n}^2} \tilde{\xi}_{\varepsilon} \tilde{\xi}_{\mu}
\end{aligned} \tag{7.11}$$

Then, these equations are solved sequentially with the boundary condition in Eq. (7.10). For example, the first order solutions are:

$$\begin{aligned}
\tilde{\xi}_{\varepsilon} &= \sin\left(\tilde{t} - \tilde{s}\right) \\
\left\langle \tilde{\xi}_{\mu} \right\rangle &= 0
\end{aligned} \tag{7.12}$$

where, $\langle\ \rangle$ represents the ensemble average. Thus, the flame wrinkle amplitude is constant at the first order; i.e., it does not decay in the absence of stretch or nonlinear effects, as discussed earlier. The solution, $\tilde{\xi}_{\varepsilon}$, mimics the forcing and convects downstream as a traveling wave at the tangential velocity, $u_{s,0}$.

The full solutions of these equations are quite lengthy, but can be developed using standard techniques and are presented in Sec. 3.3. The particular focus of this study is in the ensemble averaged dynamics of $\tilde{\xi}$. Solutions for the ensemble averaged flame position are:

$$\left\langle \tilde{\xi}_{\varepsilon\varepsilon} \right\rangle = \frac{1}{4} \cdot \tilde{S}_L \cdot \left[\tilde{s} + \tilde{s} \cdot \cos\left(2\left(\tilde{t} - \tilde{s}\right)\right) \right] \tag{7.13}$$

$$\left\langle \tilde{\xi}_{\varepsilon\varepsilon\varepsilon} \right\rangle = -\frac{1}{8} \cdot \tilde{S}_L{}^2 \cdot \left[\tilde{s}^2 \sin\left(\tilde{t} - \tilde{s}\right) + 3\tilde{s} \cos\left(\tilde{t} - \tilde{s}\right) + \tilde{s}^2 \sin\left(3\left(\tilde{t} - \tilde{s}\right)\right) + \tilde{s} \cos\left(3\left(\tilde{t} - \tilde{s}\right)\right) \right] \tag{7.14}$$

$$\left\langle \tilde{\xi}_{\varepsilon\mu} \right\rangle = \left\langle \tilde{\xi}_{\varepsilon\varepsilon\mu} \right\rangle = \left\langle \tilde{\xi}_{\mu\mu\mu} \right\rangle = 0 \tag{7.15}$$

$$\left\langle \tilde{\xi}_{\mu\mu} \right\rangle = \left(\frac{\tilde{S}_L}{2} - \frac{5}{\tilde{S}_L} \right) \tilde{s} + \left(\frac{3\tilde{L}_{11}}{\tilde{S}_L{}^2} + \frac{\pi \tilde{s}^2}{\tilde{L}_{11}} \right) \cdot erf\left(\frac{\sqrt{\pi}}{2} \frac{\tilde{S}_L \tilde{s}}{\tilde{L}_{11}} \right) + \frac{2\tilde{s}}{\tilde{S}_L} \exp\left(-\frac{\pi}{4} \left(\frac{\tilde{S}_L \tilde{s}}{\tilde{L}_{11}} \right)^2 \right) \tag{7.16}$$

$$\begin{aligned} \left\langle \tilde{\xi}_{\varepsilon\mu\mu} \right\rangle = & \left\{ \begin{array}{l} \left(-\frac{2}{3}\tilde{s}^2 - \frac{2}{3\pi} \left(\frac{\tilde{L}_{11}}{\tilde{S}_L} \right)^2 \right) \exp\left(-\frac{\pi}{4} \left(\frac{\tilde{S}_L \tilde{s}}{\tilde{L}_{11}} \right)^2 \right) \\ -\left(\frac{\pi}{3} \frac{\tilde{S}_L \tilde{s}^3}{\tilde{L}_{11}} + \frac{\tilde{L}_{11} \tilde{s}}{\tilde{S}_L} \right) erf\left(\frac{\sqrt{\pi}}{2} \frac{\tilde{S}_L \tilde{s}}{\tilde{L}_{11}} \right) + \left(1 - \frac{1}{2}\tilde{S}_L{}^2 \right) \tilde{s}^2 + \frac{2}{3\pi} \frac{\tilde{L}_{11}{}^2}{\tilde{S}_L{}^2} \end{array} \right\} \sin\left(\tilde{t} - \tilde{s} \right) \\ & + \left\{ -4\tilde{s} \exp\left(-\frac{\pi}{4} \left(\frac{\tilde{S}_L \tilde{s}}{\tilde{L}_{11}} \right)^2 \right) - \left(\frac{2\pi \tilde{S}_L \tilde{s}^2}{\tilde{L}_{11}} + \frac{\tilde{L}_{11}}{\tilde{S}_L} \right) erf\left(\frac{\sqrt{\pi}}{2} \frac{\tilde{S}_L \tilde{s}}{\tilde{L}_{11}} \right) + 4\tilde{s} - \frac{3}{2}\tilde{S}_L{}^2 \tilde{s} \right\} \cos\left(\tilde{t} - \tilde{s} \right) \end{aligned} \tag{7.17}$$

As shown in Eq. (7.15), the ensemble average of several of the terms in the expansion is zero. The terms contributing to either the ensemble or time average are $\left\langle \tilde{\xi}_{\varepsilon} \right\rangle$, $\left\langle \tilde{\xi}_{\varepsilon\varepsilon} \right\rangle$, $\left\langle \tilde{\xi}_{\mu\mu} \right\rangle$, $\left\langle \tilde{\xi}_{\varepsilon\varepsilon\varepsilon} \right\rangle$, and $\left\langle \tilde{\xi}_{\varepsilon\mu\mu} \right\rangle$. Note that the non-zero time averaged terms reflect a shift in flame position from its unperturbed location, due to the augmentation of the turbulent burning velocity by flow fluctuations, both narrowband and stochastic. This solution is discussed further and compared with computations in the next section.

7.3 Results and Analysis

This section presents analyses of the computational and asymptotic flame results to understand the factors controlling the ensemble averaged dynamics of flame wrinkles. Figure 7.4a and Figure 7.4b show a typical sequence of instantaneous computational results at two turbulence intensities. They show the presence of randomly distributed flame wrinkles with variation in both *s*- and *z*-directions; variations in the *z*-direction disappear with ensemble averaging. Also evident in the images is the progressive decay in the coherent, sinuous flame sheet fluctuations with downstream distance. As we will

show in this section, these wrinkles decay even in the absence of turbulence, but the decay rate is accelerated by turbulent fluctuations.

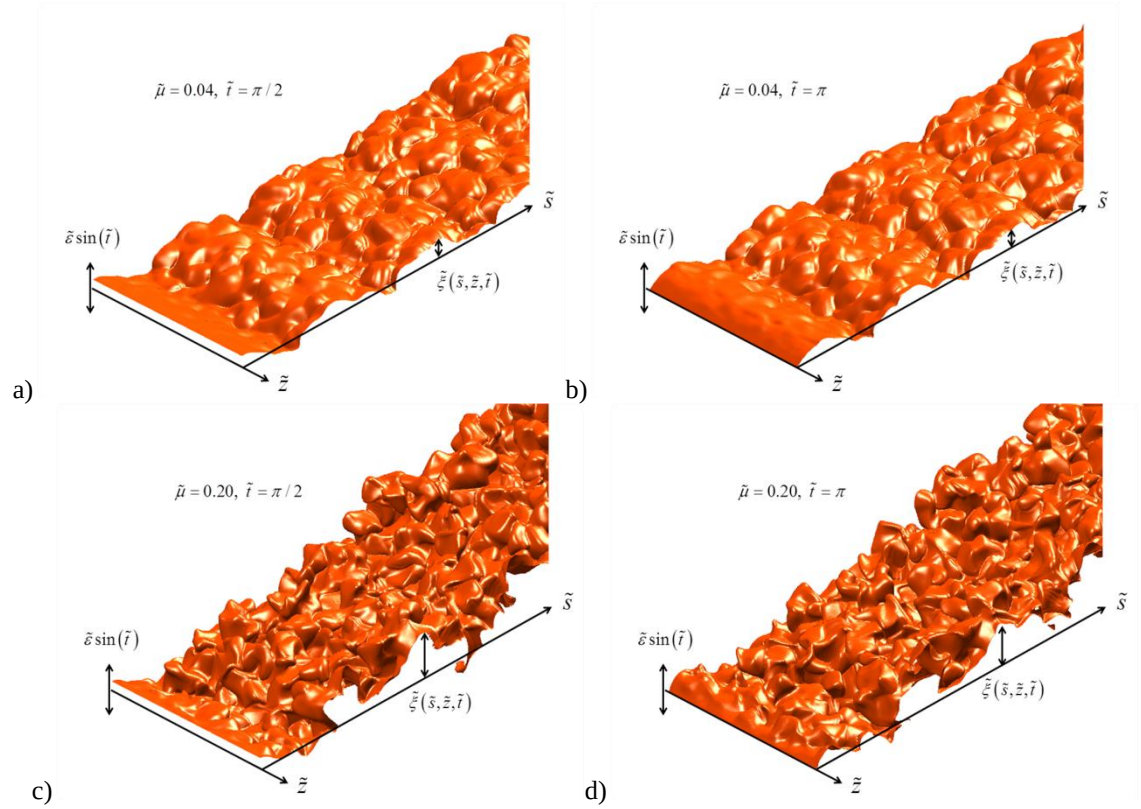

Figure 7.4. Instantaneous realizations of the flame sheet extracted from solution of full level set equation, Eq. (6.1). a,b) $\tilde{\mu}$ =0.04, c,d) $\tilde{\mu}$ =0.20 ($\tilde{S}_L$ =0.25, $\tilde{\varepsilon}$ =0.65, $\tilde{L}_{11}$ = 0.65).

7.3.1 Ensemble Averaged Near Field Characteristics

This section presents results illustrating the role of turbulent fluctuations in smoothing the excited flame wrinkles near the flame holder, where the asymptotic results can also be used. These results are a generalization of those shown in Figure 6.6, that illustrated the role of kinematic restoration in evolving the flame wrinkle shape in a laminar flow.

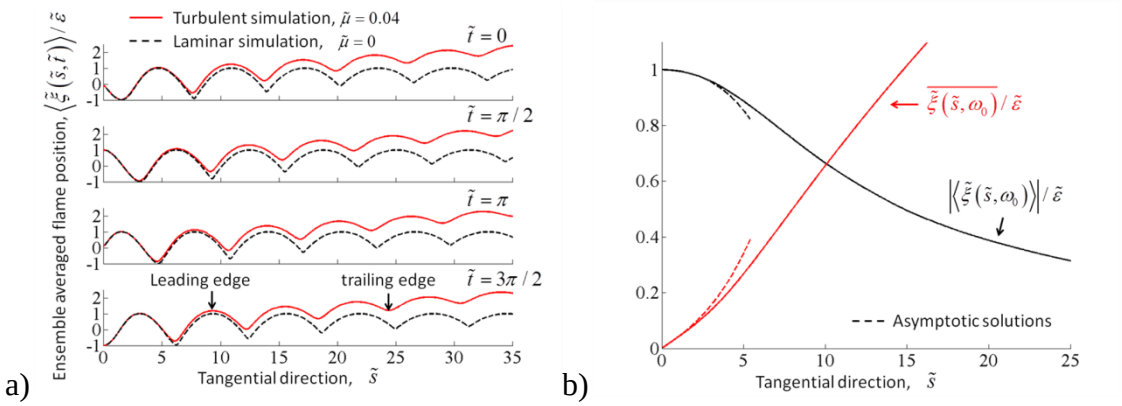

Figure 7.5. a) Ensemble averaged flame position, $\left\langle\tilde{\xi}\left(\tilde{s},\tilde{t}\right)\right\rangle$, at four times during a forcing period obtained from level set computations b) Corresponding Fourier coefficients of ensemble averaged flame front (solid) and corresponding asymptotic solutions (dashed). Conditions are $\tilde{S}_L$ =0.25, $\tilde{\varepsilon}$ =0.65, $\tilde{\mu}$ =0.04, $\tilde{L}_{11}$ = 0.65.

Figure 7.5a plots the ensemble averaged flame position at four phases during a forcing period. For reference, the laminar case (i.e., $\tilde{\mu}$ =0) is also indicated by the dashed lines. Several observations can be made from this first. First, it shows that harmonically oscillating flame wrinkles convect downstream while decaying as damped sinusoids. Second, note that the overall turbulent flame position shifts upward relative to the laminar one with downstream distance, due to the increase of the turbulent burning velocity by the random fluctuations [64]. Third, the ensemble average of the turbulent case shows a smoothing of the trailing edges, in contrast to the discontinuity in slope of the laminar case. This smoothing of the very short wavelength trailing edge resembles the effect of stretch in laminar flames with positive Markstein lengths, an observation that will be quantified and fleshed out later. Finally, the peak-to-peak amplitude of the flame wrinkle is clearly different between the two curves (solid and dash), showing the accelerating smoothing of the flame wrinkle in the turbulent case.

These observations are further quantified in Figure 7.5b, which plots the axial dependence of the ensemble averaged flame response at the forcing frequency, ω_0, and the time averaged position. The figure shows the monotonic decay in flame wrinkle amplitude, as well as the shift outward in average flame position, due to the rise in turbulent burning velocity. The asymptotic solutions, presented in Eqs. (7.12)-(7.17) are also indicated in Figure 7.5b by the dashed lines, which show good agreement in the near field. These asymptotic solutions can be interpreted more easily by being expanded in powers of tangential coordinate, $\tilde{s}$, as:

$$\overline{\tilde{\xi}\left(\tilde{s},\tilde{t}\right)} = \tilde{\mu}^2\left(\frac{\tilde{S}_L}{2}\tilde{s} + \frac{\pi}{4}\frac{\tilde{S}_L}{\tilde{L}_{11}{}^2}\tilde{s}^3 + O\left(\tilde{s}^5\right)\right) + \frac{1}{4}\tilde{\varepsilon}^2\tilde{S}_L\tilde{s} + O\left(\left(\tilde{\mu},\tilde{\varepsilon}\right)^4\right) \tag{7.18}$$

$$\frac{\left|\left\langle\tilde{\xi}\left(\tilde{s},\omega_0\right)\right\rangle\right|}{\tilde{\varepsilon}} = 1 - \frac{1}{8}\tilde{\varepsilon}^2\tilde{S}_L{}^2\tilde{s}^2 - \frac{1}{2}\tilde{\mu}^2\tilde{s}^2 - \frac{1}{2}\tilde{\mu}^2\tilde{S}_L{}^2\tilde{s}^2 - \frac{5\pi}{48}\frac{\tilde{\mu}^2\tilde{S}_L{}^2}{\tilde{L}_{11}{}^2}\tilde{s}^4 + O\left(\tilde{s}^5,\tilde{\mu}^3\right) \tag{7.19}$$

where, the overbar, $\overline{(\ )}$, represents the time average. Note that the second term in Eq. (7.19) describes the decrease in laminar flame wrinkle size due to kinematic restoration, which was covered in the previous study [107]. We will next focus on the remaining terms that are multiplied by $\tilde{\mu}^2$ and, thus, are due to stochastic forcing effects. This equation shows that the flame wrinkle size decays quadratically with downstream distance, $\tilde{s}^2$, and turbulence intensity, $\tilde{\mu}^2$, in the near field. There are two terms, $-\tilde{\mu}^2\tilde{s}^2/2$ and $-\tilde{\mu}^2\tilde{S}_L{}^2\tilde{s}^2/2$, due to two fundamentally different processes, leading to this smoothing effect in the leading order terms. The first of these terms, $-\tilde{\mu}^2\tilde{s}^2/2$, is independent of burning velocity or equivalently, kinematic restoration effects. Since, $\tilde{S}_L$ <<1 in high velocity flows, this term is actually the dominant near-field effect.

This dominant smoothing effect ($-\tilde{\mu}^2\tilde{s}^2/2$) is due to phase jitter associated with the $\mu f_s \cdot \partial\xi/\partial s$ term on the right side of Eq. (7.4); i.e., fluctuations in tangential flow velocity cause the axial position of the flame wrinkle to fluctuate randomly. As shown in Figure 7.6, this leads to a reduction in ensemble averaged flame wrinkle amplitude, as the ensemble average of a harmonic quantity subjected to phase jitter is reduced in magnitude.

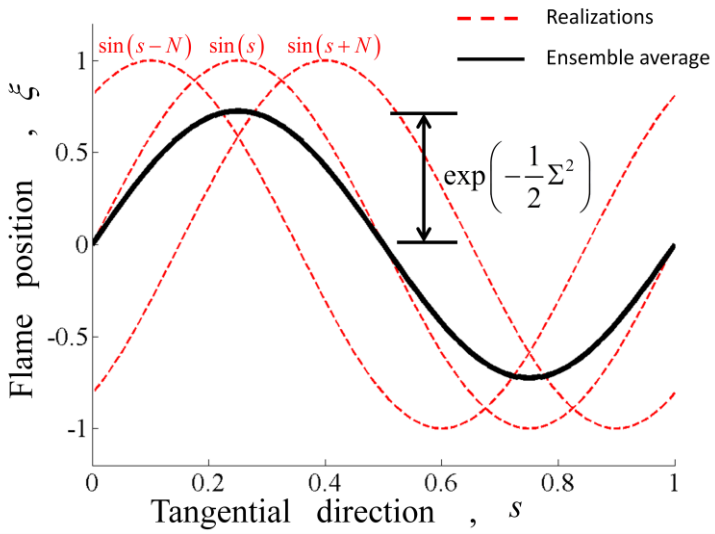

Figure 7.6. Illustration of the reduction of ensemble averaged flame wrinkle size by random tangential motions of the flame wrinkle, or "phase jitter".

To illustrate, consider the ensemble average of a harmonically oscillating disturbance, $\sin(2\pi s)$, subjected to a Gaussian phase noise, *N(t)*, with a mean of zero and a variance of Σ^2. The ensemble average of the disturbance is written as:

$$\left\langle \sin\left(2\pi s + N(t)\right)\right\rangle = \sin(2\pi s)\cdot\left\langle \cos\left(N(t)\right)\right\rangle + \cos(2\pi s)\cdot\left\langle \sin\left(N(t)\right)\right\rangle \qquad (7.20)$$

Note that $\left\langle \cos\left(N(t)\right)\right\rangle = \exp\left(-\Sigma^2/2\right)$ and $\left\langle \sin\left(N(t)\right)\right\rangle = 0$ for Gaussian noise. Therefore, Eq. (7.20) becomes as:

$$\left\langle \sin\left(2\pi s + N(t)\right)\right\rangle = \exp\left(-\Sigma^2/2\right)\cdot\sin\left(2\pi s\right) \tag{7.21}$$

This equation indicates that the ensemble average of the disturbance decreases exponentially in magnitude with increases in variance, Σ^2, of the noise. Note that this effect is only due to tangential velocity fluctuations, u_s'. In contrast, velocity fluctuations normal to the flame, u_n', do not alter the ensemble average by convection effects. This is analogous to additive noise addition to a harmonic disturbance:

$$\left\langle \sin\left(2\pi s\right) + N(t)\right\rangle = \sin\left(2\pi s\right) \tag{7.22}$$

Related effects have been well documented in the general turbulent flow and flame literature [74, 108, 109].

Returning to Eq. (7.19), consider the next quadratic term, $-\tilde{\mu}^2\tilde{S}_L{}^2\tilde{s}^2/2$. The fact that it is proportional to $\tilde{\mu}\tilde{S}_L$ indicates that it is influenced by kinematic restoration and stochastic forcing, but note that it is completely independent of turbulent length scale, $\tilde{L}_{11}$. This term reflects the effects of random flame angle changes at the attachment point by the stochastic velocity fluctuation normal to the front. To see this, note that the kinematic restoration term in Eq. (7.4) can be rewritten as $\left(S_L/\cos\theta(t) - S_L\right)$ by using the equality, $\sqrt{1+\left(\partial\xi/\partial s\right)^2+\left(\partial\xi/\partial z\right)^2} = 1/\cos\theta(t)$, where $\theta(t)$ is the instantaneous local flame angle measured relative to the *s*-*z* plane. Since the flame angle (θ) consists of deterministic (θ_D) and random (θ_N) parts, i.e., $\theta = \theta_D + \theta_N$, the kinematic restoration effect is expanded for small θ_D and θ_N as:

$$\frac{S_L}{\cos\left(\theta_D+\theta_N\right)} - S_L = S_L\cdot\left(\theta_D+\theta_N\right)^2/2 + O\left(\left(\theta_D,\theta_N\right)^3\right) \tag{7.23}$$

Ensemble averaging this expression:

$$\left\langle \frac{S_L}{\cos\left(\theta_D+\theta_N\right)}-S_L \right\rangle = \frac{S_L{\theta_D}^2}{2}+\frac{S_L\left\langle {\theta_N}^2\right\rangle}{2}+O\left(\left(\theta_D,\theta_N\right)^3\right) \tag{7.24}$$

This equation indicates the leading order effects of kinematic restoration. The first term, $S_L{\theta_D}^2/2$, is the laminar kinematic restoration term, corresponding to the $-\tilde{\varepsilon}^2{\tilde{S}_L}^2\tilde{s}^2/8$ in Eq. (7.19). Similarly, the second term, $S_L\left\langle {\theta_N}^2\right\rangle/2$, corresponds to $-\tilde{\mu}^2{\tilde{S}_L}^2\tilde{s}^2/2$ in Eq. (7.19).

Lastly, kinematic restoration effects associated with random wrinkles excited in the domain itself first appear in the expansion in Eq. (7.19) at fourth order in distance, but second order in turbulence intensity, through the term, $\frac{5\pi}{48}\frac{\tilde{\mu}^2{\tilde{S}_L}^2}{{\tilde{L}_{11}}^2}\tilde{s}^4$. Note that this term includes terms proportional to $\tilde{S}_L$ and $\tilde{L}_{11}$, indicating that it is influenced by kinematic restoration and turbulence length scale. This is the leading order near field term describing the turbulent destruction of wrinkles in the domain itself. It shows that turbulent fluctuations of shorter length scale lead to more rapid dissipation of flame wrinkles, scaling as $1/{\tilde{L}_{11}}^2$, an effect which would be expected given the scale-dependent nature of kinematic restoration.

This asymptotic expansion shows how three fundamentally different effects come to play in the near field, with completely different dependencies on location (e.g., $\tilde{s}^2$ or $\tilde{s}^4$), flame propagation (e.g., 1 or ${\tilde{S}_L}^2$), and turbulence characteristics (e.g., $\tilde{L}_{11}$). However, as shown in Figure 7.5b, this expansion loses validity with downstream distance, $\tilde{s} > \sim 3$ in this example, where the coupled effects of kinematic restoration and stochastic excitation must be studied numerically.

An additional important result from the asymptotic analysis is that the deterministic and stochastic effects are decoupled up to third order, as $\left\langle \tilde{\xi}_{\varepsilon\varepsilon\mu} \right\rangle = 0$ in Eq. (7.15). As a result, to this order, the leading order correction to the flame response can be obtained from the following linear sum of deterministic and stochastic effects in isolation:

$$\textit{Near field}: \quad \frac{\left|\left\langle \tilde{\xi}(\omega_0) \right\rangle\right|}{\tilde{\varepsilon}} = 1 - \frac{1}{8}\left(\tilde{\varepsilon}\tilde{S}_L\tilde{s}\right)^2 - \frac{\tilde{\mu}^2}{2}\left(1+\tilde{S}_L{}^2\right)\tilde{s}^2 + O\left(\tilde{s}^4, (\tilde{\varepsilon},\tilde{\mu})^4\right) \quad (7.25)$$

However, this result is limited to the near field as the asymptotic solution in Eqs. (7.15) to (6.23) quickly loses accuracy further downstream.

In order to illustrate the combined effects of harmonic and stochastic excitation, Figure 7.7 plots the results of several computations showing the axial dependence of the flame wrinkle fluctuation at the forcing frequency at several turbulence intensities. The $\tilde{\mu}$ =0 curve shows the laminar result, showing the monotonic decay in flame wrinkle amplitude with downstream distance, for reasons discussed previously. In addition, curves are shown at $\tilde{\mu}$ =0.04 and 0.10 values, showing the increased decay rate of $\left|\left\langle \tilde{\xi}(\tilde{s},\omega_0) \right\rangle\right|$ with increasing turbulence intensity. The plot clearly shows how both deterministic and stochastic processes lead to a decay in flame wrinkle size. Their relative significance is a function of the values of $\tilde{\varepsilon}$ and $\tilde{\mu}$.

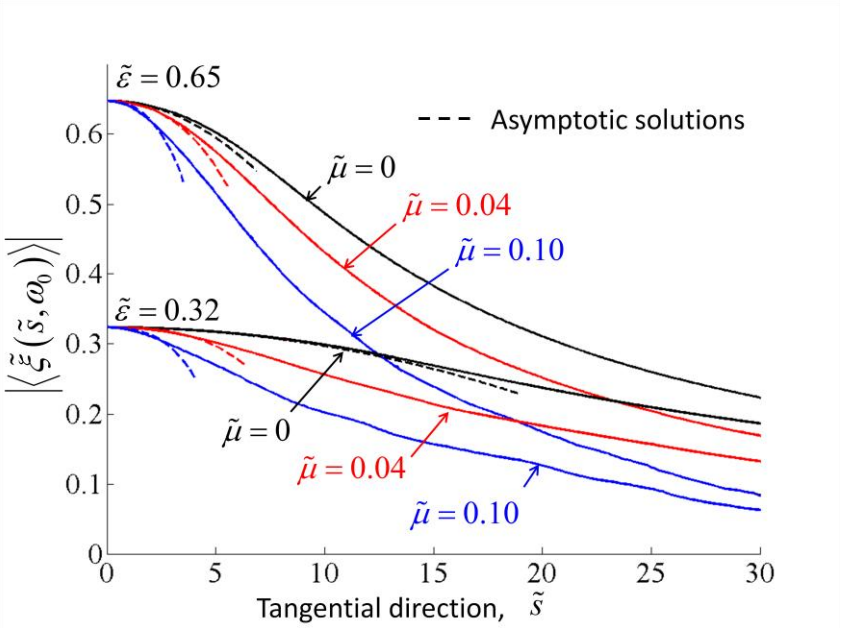

Figure 7.7. Comparison of the flame responses at different turbulence intensities ($\tilde{S}_L$ =0.25 and $\tilde{L}_{11}$ = 0.65).

The rest of this chapter considers these downstream characteristics in more detail. In order to understand the factors controlling the far field region, it is first necessary to understand the effects of stochastic forcing on the ensemble averaged, time varying turbulent burning velocity, which is treated next.

7.3.2 Ensemble Averaged Turbulent Burning Velocity

In the laminar case, it is the propagation of the flame normal to itself that leads to smoothing of flame wrinkles, as illustrated in Figure 6.6 - thus the wrinkle decay rate is directly proportional to the laminar burning velocity, S_L , as shown in Eq. (6.21). Important insights into the turbulent case can be obtained by considering analogies to the laminar problem and considering the ensemble averaged turbulent burning velocity. An important generalization from the laminar problem, however, is that even in the case

where the flame has no stretch sensitivity, the turbulent burning velocity is time varying and modulated harmonically.

To follow this point, consider the following equation for the ensemble averaged flame dynamics, similar to expressions proposed heuristically by several prior studies [25, 71, 110].

$$\frac{\partial\langle\tilde{\xi}\rangle}{\partial\tilde{t}}+\langle\tilde{u}_s\rangle\frac{\partial\langle\tilde{\xi}\rangle}{\partial\tilde{s}}-\langle\tilde{u}_n\rangle+\langle\tilde{u}_z\rangle\frac{\partial\langle\tilde{\xi}\rangle}{\partial\tilde{z}}=\tilde{S}_{T,eff}\cdot\left[1+\left(\frac{\partial\langle\tilde{\xi}\rangle}{\partial\tilde{s}}\right)^2+\left(\frac{\partial\langle\tilde{\xi}\rangle}{\partial\tilde{z}}\right)^2\right]^{1/2} \tag{7.26}$$

where, $(\tilde{\ })$ represents a non-dimensional variable same as defined in Eq. (7.8) – velocities, lengths, and time are normalized by $u_{s,0}$, $u_{s,0}/\omega_0$, and ω_0, respectively. Note that Eq. (7.26) is essentially a definition of $\tilde{S}_{T,eff}$, which is then given by:

$$\tilde{S}_{T,eff}\left(\tilde{s},\tilde{z},\tilde{t}\right)\equiv\frac{\frac{\partial\langle\tilde{\xi}\rangle}{\partial\tilde{t}}+\langle\tilde{u}_s\rangle\frac{\partial\langle\xi\rangle}{\partial\tilde{s}}-\langle\tilde{u}_n\rangle+\langle\tilde{u}_z\rangle\frac{\partial\langle\tilde{\xi}\rangle}{\partial\tilde{z}}}{\left[1+\left(\partial\langle\tilde{\xi}\rangle/\partial\tilde{s}\right)^2+\left(\partial\langle\tilde{\xi}\rangle/\partial\tilde{z}\right)^2\right]^{1/2}} \tag{7.27}$$

It is important to note that the turbulent flame speed can be defined in different ways, leading to different results. The typical definition of displacement flame speed, $\tilde{S}_{T,disp}$, used in flows without harmonic forcing is [49]:

$$\tilde{S}_{T,disp}\left(\tilde{s},\tilde{z}\right)\equiv\frac{\bar{\tilde{u}}_s\cdot\partial\bar{\tilde{\xi}}/\partial\tilde{s}-\bar{\tilde{u}}_n+\bar{\tilde{u}}_z\cdot\partial\bar{\tilde{\xi}}/\partial\tilde{z}}{\left[1+\left(\partial\bar{\tilde{\xi}}/\partial\tilde{s}\right)^2+\left(\partial\bar{\tilde{\xi}}/\partial\tilde{z}\right)^2\right]^{1/2}} \tag{7.28}$$

The time average of $\tilde{S}_{T,eff}$, $\overline{\tilde{S}_{T,eff}}$, differs from $\tilde{S}_{T,disp}$ because of the non-zero time average produced by the multiplication of two harmonically oscillating terms. For example, $\bar{\tilde{u}}_s\cdot\partial\bar{\tilde{\xi}}/\partial\tilde{s}$ does not equal $\overline{\tilde{u}_s\cdot\partial\tilde{\xi}/\partial\tilde{s}}$ in the presence of harmonic flow

perturbations. This difference can be explicitly shown from the asymptotic solutions for $\overline{\tilde{S}_{T,eff}}$ and $\tilde{S}_{T,disp}$ at $\tilde{s}$=0:

$$\frac{\overline{\tilde{S}_{T,eff}}\left(\tilde{s}=0\right)}{\tilde{S}_L}=1+\frac{\tilde{\mu}^2}{2}+O\left(\left(\tilde{\varepsilon},\tilde{\mu}\right)^4\right) \tag{7.29}$$

$$\frac{\tilde{S}_{T,disp}\left(\tilde{s}=0\right)}{\tilde{S}_L}=1+\frac{1}{4}\tilde{\varepsilon}^2+\frac{1}{2}\tilde{\mu}^2+O\left(\left(\tilde{\varepsilon},\tilde{\mu}\right)^4\right) \tag{7.30}$$

Note that these equations converge to the same result when $\tilde{\varepsilon}$=0, but otherwise, $\tilde{S}_{T,disp}$ has an $\tilde{\varepsilon}$ sensitivity while $\overline{\tilde{S}_{T,eff}}$ does not. Similar points can be seen more generally in Figure 7.8a and Figure 7.8b, which plot the computed dependence of $\overline{\tilde{S}_{T,eff}}$ and $\tilde{S}_{T,disp}$ upon downstream distance, $\tilde{s}$, for different $\tilde{\varepsilon}$ and $\tilde{\mu}$ values.

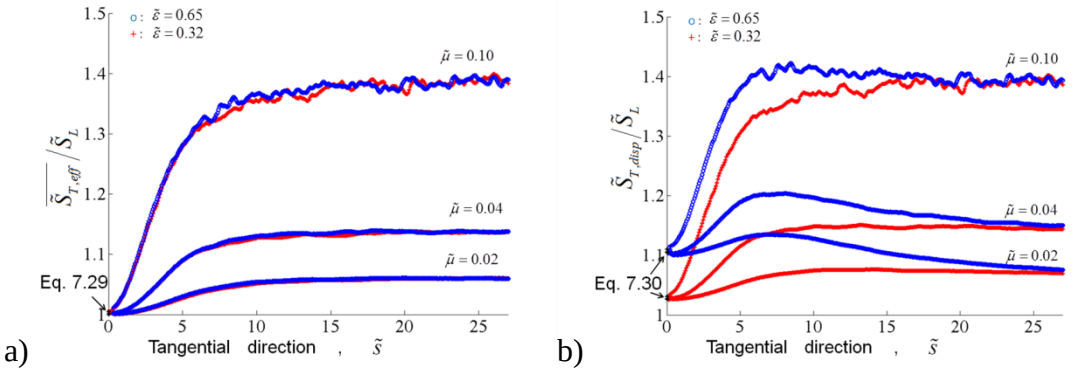

Figure 7.8. a) Dependence of $\overline{\tilde{S}_{T,eff}}$ on downstream distance. b) Dependence of $\tilde{S}_{T,disp}$ on downstream distance ($\tilde{S}_L$ =0.25 and $\tilde{L}_{11}$ = 0.65).

At a fixed axial location, both $\overline{\tilde{S}_{T,eff}}$ and $\tilde{S}_{T,disp}$ are an increasing function of $\tilde{\mu}$, as might be expected. However, $\overline{\tilde{S}_{T,eff}}$ is essentially independent of harmonic forcing amplitude, $\tilde{\varepsilon}$, for all cases shown, as suggested by Eq. (7.29).

Having discussed some basic differences of $\tilde{S}_{T,eff}$ from typical definitions used in the turbulent combustion literature in the absence of harmonic forcing, we next consider its characteristics further. The space-time dependence of $\tilde{S}_{T,eff}$ can be directly extracted from computed results using Eq. (7.27). To illustrate, Figure 7.9 plots the extracted dependence of $\tilde{S}_{T,eff}$ at two time instants for the same calculation shown in Figure 7.5a, where the instantaneous flame position is also plotted for ease of comparison.

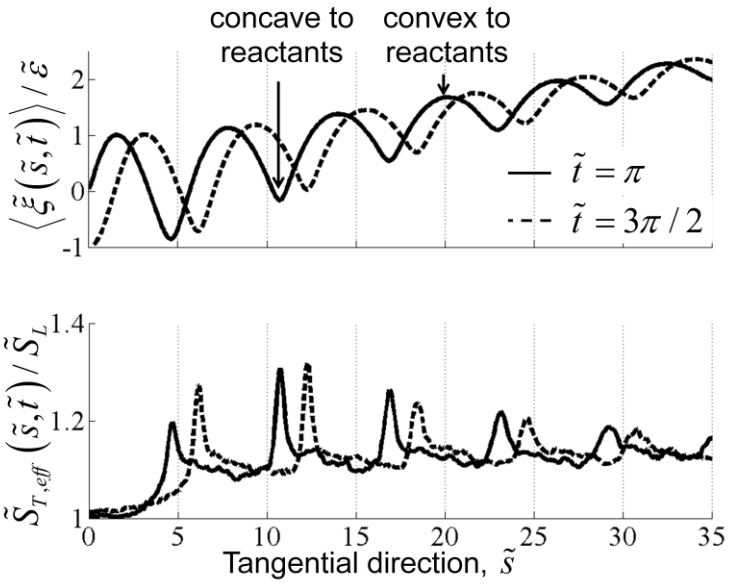

Figure 7.9. Dependence of ensemble averaged flame position (top) and extracted $\tilde{S}_{T,eff}$ value (bottom) on downstream distance at two time instants($\tilde{S}_L$ =0.25, $\tilde{\varepsilon}$ =0.65, $\tilde{L}_{11}$ = 0.65, $\tilde{\mu}$ =0.04).

This figure shows that $\tilde{S}_{T,eff}$ is a function of both space and time. The rest of this section briefly revisit its time averaged characteristics, and then focuses on its time-varying features. The axial evolution of $\overline{\tilde{S}_{T,eff}}$ shown in Figure 7.8a indicates an initial

development in the near field followed by the saturation far from the flame holder, similar to other observations in spatially or temporally evolving flames [111, 112]. The fact that $\overline{\tilde{S}_{T,eff}}$ exceeds $\tilde{S}_L$, such as shown in Figure 7.8a, is important and directly responsible for the increasing decay rate of flame wrinkles shown in Figure 7.7. The results in Figure 7.7 show that increasing $\tilde{\mu}$ at a fixed $\tilde{\varepsilon}$ leads to a monotonically increasing smoothing rate of flame wrinkles. In other words, a faster averaged burning rate leads to faster smoothing of the ensemble averaged flame wrinkles, directly analogous to the sensitivity of laminar flames to $\tilde{S}_L$. This point can also be seen by noting that Eqs. (6.2) and (7.26) are identical if $\tilde{S}_{T,eff}$ is a constant, and replacing $\tilde{\xi}$ and $\tilde{S}_L$ with $\left\langle \tilde{\xi} \right\rangle$ and $\tilde{S}_{T,eff}$, respectively.

Having considered the effects of $\overline{\tilde{S}_{T,eff}}$ upon the decay rate of flame wrinkles, we next consider its space-time modulation, illustrated in Figure 7.9. In comparing the top and bottom figures, note how $\tilde{S}_{T,eff}$ instantaneously rises at points where the ensemble averaged front is concave to the reactants and falls at points that are convex. This point is quantified inFigure 7.10a which plot values of $\tilde{S}_{T,eff}$ extracted from calculations at points through the harmonic forcing cycle, as a function of ensemble averaged radius of curvature of the flame, $\tilde{c}$, defined as:

$$\tilde{c} = \frac{\partial^2 \left\langle \tilde{\xi}\left(\tilde{s},\tilde{t}\right)\right\rangle / \partial \tilde{s}^2}{\left[1+\left(\partial \left\langle \tilde{\xi}\left(\tilde{s},\tilde{t}\right)\right\rangle / \partial \tilde{s}\right)^2\right]^{3/2}} \tag{7.31}$$

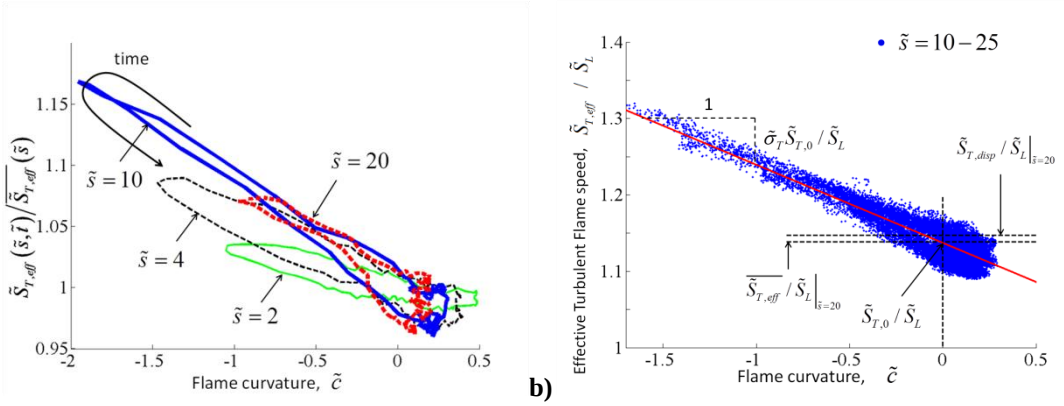

Figure 7.10. Correlation of the curvature of the ensemble averaged flame front and the turbulent flame speed defined in Eq. (7.27). (a) Scaled by by $\overline{\tilde{S}_{T,eff}}(\tilde{s})$ at selected downstream locations and (b) scaled by the laminar flame speed at downstream locations where $\overline{\tilde{S}_{T,eff}}$ has approached a constant value. Values of $\overline{\tilde{S}_{T,eff}}/\tilde{S}_L|_{\tilde{s}=20}$, $\tilde{S}_{T,disp}/\tilde{S}_L|_{\tilde{s}=20}$, $\tilde{S}_{T,0}/\tilde{S}_L$, and $\tilde{\sigma}_T\tilde{S}_{T,0}/\tilde{S}_L$ are indicated for reference, whose values are 1.14, 1.15, 1.14, and -0.102, respectively (conditions are $\tilde{\varepsilon}$ =0.65, $\tilde{\mu}$ =0.04, $\tilde{L}_{11}$ =0.65, $\tilde{S}_L$ =0.25).

Note the clear negative correlation of burning velocity with ensemble averaged curvature. In other words, locations with ensemble averaged negative curvatures are associated with augmentation of the unsteady, ensemble averaged burning velocity and vice-versa. This behavior is analogous to stretch sensitive flames with positive Markstein lengths; i.e., where σ>0. In the laminar case, this stretch sensitivity is due to convective-diffusive flux imbalances in the finite thickness flame [113], while the analogous behavior in the turbulent case is due to the effect of stochastic flame wrinkling on the ensemble averaged flame wrinkle position. However, it is important to emphasize that while the Markstein length concept applies instantaneously in the laminar case, this turbulent analogue applies only to the ensemble average.

The fact that the curves trace out an ellipse indicates that the relationship between instantaneous curvature and $\tilde{S}_{T,eff}$ is not quasi-steady; i.e. there is a phase lag between the two, but this lag is not large for this condition. Note also how $\tilde{S}_{T,eff}$ and $\tilde{c}$ correlation becomes nearly independent of position at $\tilde{s}$ =10 and 20, which corresponds to locations where $\overline{\tilde{S}_{T,eff}}$ has approached a constant value.

For the rest of this section, we focus on this relationship at downstream locations downstream where $\overline{\tilde{S}_{T,eff}}$ is approximately spatially constant. Figure 7.10b plots $\tilde{S}_{T,eff}$ at a range of such positions, showing that we can write the following approximate expression for $\tilde{S}_{T,eff}$ in the far field as:

$$\tilde{S}_{T,eff} = \tilde{S}_{T,0}\left(1-\tilde{\sigma}_T \cdot \tilde{c}\right) \tag{7.32}$$

where, $\tilde{S}_{T,0}$, and $\tilde{\sigma}_T$ are the effective turbulent flame speed at zero curvature and the "turbulent Markstein length", respectively. Note that $\tilde{S}_{T,0}$ and $\overline{\tilde{S}_{T,eff}}$ have different definitions in general, but are similar in value as shown by Figure 7.10b. Also, a more accurate representation of the ensemble averaged burning velocity would be to include the phase delay between $\tilde{S}_{T,eff}$ and $\tilde{c}$, which we will not include for simplicity here. A more detailed characterization of the effects of harmonic modulation on $\tilde{S}_{T,eff}$ is outside the scope of this study.

The same behavior was observed for all computed cases. To illustrate, Figure 7.11 plots similar calculation results for several turbulence intensities, showing that $\tilde{\sigma}_T$ is an increasing function of turbulence intensity, as might be expected. The larger scatter in the $\tilde{\mu}$ =0.1 case is primarily a reflection of noise introduced in calculation of the second

derivative of flame position, needed for the curvature. Although the 160 ensemble averages are sufficient for calculation of $\langle \tilde{\xi} \rangle$, the small amount of noise present in these ensemble average estimates are amplified significantly in estimates of the second derivative. Results are shown for two $\tilde{\varepsilon}$ values, showing the larger range of ensemble averaged flame curvatures that are present with increased harmonic forcing amplitude. Note also the diminished range of negative curvature values for the highest $\tilde{\mu}$ case, a reflection of the very rapid destruction of high curvature regions by stochastic flame wrinkling.

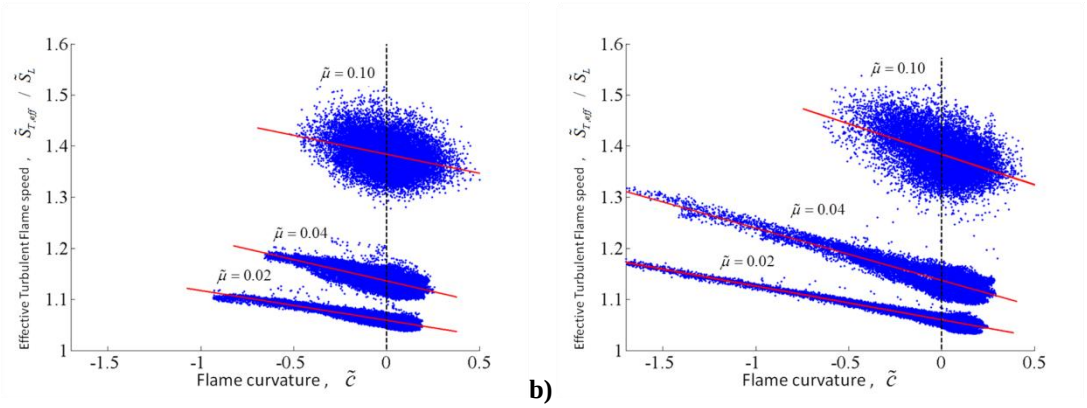

Figure 7.11. Correlation of the curvature of the ensemble averaged flame front and the turbulent flame speed defined in Eq. (7.27). a) $\tilde{\varepsilon}$ =0.32, b) $\tilde{\varepsilon}$ =0.65 (other conditions are $\tilde{L}_{11}$ =0.65, $\tilde{S}_L$ =0.25).

While the Markstein length analogy has been quantified in Figure 7.10 based on post-processing calculations, the physical reasons why this behavior occurs can be understood from consideration of Huygens propagation. To illustrate, Figure 7.12 illustrates three instantaneous notational images of flames with ensemble averaged positive, negative, and zero curvature, with superposed wrinkles. As shown in Figure 7.12, the effect of kinematic restoration is most prominent at the trailing edges of the

flame, where the two opposing flame branches propagate into each other and annihilate each other. As the trailing edges are destroyed, the flame shifts toward the reactants sides, which also manifests itself as an increase in turbulent flame speed. This flame-flame interaction and annihilation process is strongly dependent upon the ensemble averaged curvature of the flame, as it is suppressed in outwardly propagating, positively curved flames (see the different degrees of change of mean flame position from *t=0* to *t=dt* marked by dash lines in Figure 7.12). It is augmented in inwardly propagating, negatively curved flames.

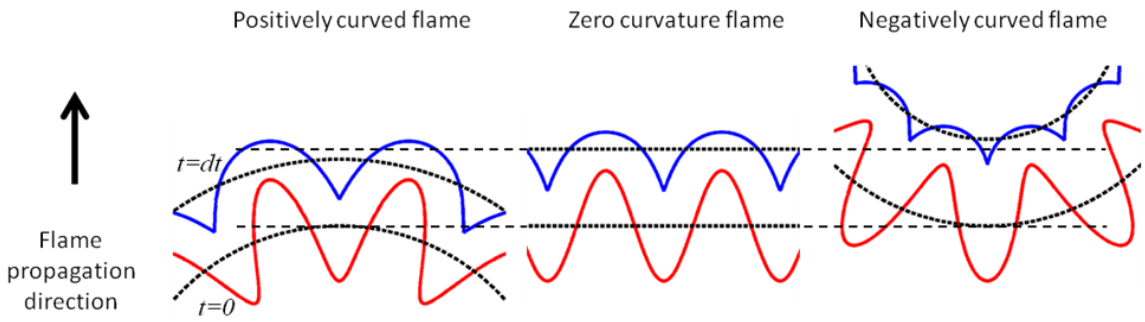

Figure 7.12. Illustration of change of curvatures on trailing edges of the flames with different large scale curvatures.

To summarize then, $\tilde{S}_{T,eff}$ can be written as $\tilde{S}_{T,eff} = \overline{\tilde{S}_{T,eff}} + \tilde{S}_{T,eff}{}'$, where $\tilde{S}_{T,eff}{}'$ is a periodic function of time, that can also be approximately parameterized as a function of the local curvature; i.e.,

$$\tilde{S}_{T,eff} = \overline{\tilde{S}_{T,eff}}\left(1-\tilde{\sigma}_T \cdot \tilde{c}\right) \tag{7.33}$$

Following from the analogies of the solution to the laminar flame problem, this latter effect has a term that is *linear* in harmonic perturbation amplitude, $\left|\left\langle \tilde{\xi}\left(\tilde{s},\omega_0\right)\right\rangle\right|$, i.e., expanding the curvature in Eq. (7.31) in a Taylor series, the leading order term is given

by $\tilde{c} = \partial^2 \left\langle \tilde{\xi}\left(\tilde{s},\omega_0\right)\right\rangle / \partial s^2 + O\left(\left\langle \tilde{\xi}\left(\tilde{s},\omega_0\right)\right\rangle^2\right)$. This point has important implications on the functional dependence of $\tilde{\xi}$ upon downstream distance, as elaborated on in the next section.

7.3.3 Ensemble Averaged Far Field Characteristics

In this section, we analyze the flame response in the far field, using results from the level set computations. Figure 7.7 clearly shows the faster smoothing of ensemble averaged flame wrinkles in the far field with increasing $\tilde{\mu}$ values. As discussed in the context of Figure 7.8, this observation is expected based upon the increasing value of $\overline{S_{T,eff}}$ with turbulence intensity, leading to faster propagation of the ensemble averaged flame front normal to itself.

While this qualitative behavior is expected, we can use the results from Section 7.3.2 to better understand the functional dependence of $\left|\left\langle \tilde{\xi}\left(\tilde{s},\omega_0\right)\right\rangle\right|$ upon downstream distance. To illustrate, we briefly return to the laminar flame problem where, as discussed in CHAPTER 6, two processes lead to flame wrinkle decay; kinematic restoration and flame stretch.

Consider first the decay rate of laminar flames dominated by kinematic restoration effects, using the $\tilde{s}$ >>1 solution from Eq. (6.15). This equation can be differentiated and rewritten in the following form that eliminates the explicit dependence on downstream distance, by replacing downstream distance with its local magnitude as:

$$\frac{\partial |\tilde{\xi}\left(\tilde{s},\omega_0\right)|}{\partial \tilde{s}} = -\frac{\tilde{S}_L}{2} |\tilde{\xi}\left(\tilde{s},\omega_0\right)|^2 \tag{7.34}$$

This equation quantifies the decay rate in flame wrinkle amplitude in terms of the local magnitude, showing that the ratio, $-\dfrac{\partial|\tilde{\xi}(\tilde{s},\omega_0)|/\partial\tilde{s}}{|\tilde{\xi}(\tilde{s},\omega_0)|^2}$, reaches a constant value in the far field, where this expression is valid. To illustrate, Figure 7.13 plots the results of a calculation for $\tilde{\mu}$=0, i.e., a laminar flame, confirming this result. This plot also indicates that this ratio varies with distance in the near field due to the two zone behavior of laminar flame as pointed earlier (Eq. (6.15) indicates that it varies as $\tilde{\varepsilon}\tilde{S}_L{}^2\tilde{s}/4$).

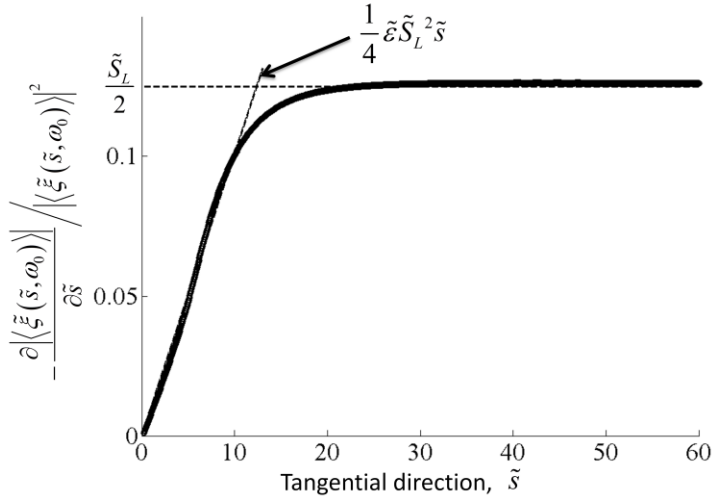

Figure 7.13. Downstream dependence of scaled slope in flame position, illustrating laminar flame scaling (conditions are $\tilde{\varepsilon}$ =0.65, $\tilde{\mu}$ = 0, and $\tilde{S}_L$ =0.25).

In a similar manner, the decay rate of stretch dominated laminar flames can be obtained from Eq. (6.25) and written as:

$$\frac{\partial|\tilde{\xi}(\tilde{s},\omega_0)|}{\partial\tilde{s}} = -\tilde{\sigma}\tilde{S}_L|\xi(\tilde{s},\omega_0)| \tag{7.35}$$

Therefore, this ratio is proportional to the product of the flame speed and normalized Markstein length, $\tilde{\sigma}$.

These laminar solutions can be used to understand the functional dependence of $\partial\left|\left\langle\tilde{\xi}\left(\tilde{s},\omega_0\right)\right\rangle\right|/\partial\tilde{s}$ upon $\left|\left\langle\tilde{\xi}\left(\tilde{s},\omega_0\right)\right\rangle\right|$, since the laminar instantaneous and ensemble averaged turbulent flame characteristics are described by analogous equations in the far field; i.e.,

Laminar instantaneous equation:

$$\frac{\partial\tilde{\xi}}{\partial\tilde{t}}+\tilde{u}_s\frac{\partial\tilde{\xi}}{\partial\tilde{s}}-\tilde{u}_n+\tilde{u}_z\frac{\partial\tilde{\xi}}{\partial\tilde{z}}=\tilde{S}_L\left(1-\tilde{\sigma}\tilde{c}\right)\cdot\left[1+\left(\frac{\partial\tilde{\xi}}{\partial\tilde{s}}\right)^2+\left(\frac{\partial\tilde{\xi}}{\partial\tilde{z}}\right)^2\right]^{1/2} \tag{7.36}$$

Turbulent ensemble averaged equation:

$$\frac{\partial\left\langle\tilde{\xi}\right\rangle}{\partial\tilde{t}}+\left\langle\tilde{u}_s\right\rangle\frac{\partial\left\langle\tilde{\xi}\right\rangle}{\partial\tilde{s}}-\left\langle\tilde{u}_n\right\rangle+\left\langle\tilde{u}_z\right\rangle\frac{\partial\left\langle\tilde{\xi}\right\rangle}{\partial\tilde{z}}=\overline{\tilde{S}_{T,eff}}\cdot\left(1-\tilde{\sigma}_T\left\langle\tilde{c}\right\rangle\right)\cdot\left[1+\left(\frac{\partial\left\langle\tilde{\xi}\right\rangle}{\partial\tilde{s}}\right)^2+\left(\frac{\partial\left\langle\tilde{\xi}\right\rangle}{\partial\tilde{z}}\right)^2\right]^{1/2} \tag{7.37}$$

Increases in turbulence intensity, $\tilde{\mu}$, lead to two effects - increases in $\overline{\tilde{S}_{T,eff}}$ and the magnitude of $\tilde{S}_{T,eff}{}'$, because of the increases in "turbulent Markstein length". Again, using the previously developed laminar flame solutions as a guide, both effects lead to destruction of flame wrinkles. However, the first effect is nonlinear in harmonic disturbance amplitude, $\left|\left\langle\tilde{\xi}\left(\tilde{s},\omega_0\right)\right\rangle\right|$, while the second has a leading order linear term in $\left|\left\langle\tilde{\xi}\left(\tilde{s},\omega_0\right)\right\rangle\right|$. Thus, the dependence of the far field solution characteristics upon $\left|\left\langle\tilde{\xi}\left(\tilde{s},\omega_0\right)\right\rangle\right|$ are a nonlinear function of $\tilde{\mu}$. In other words, consider the case where $\tilde{\mu}$=0 and $\tilde{\varepsilon}$ is nonzero. In this limit, only deterministic kinematic restoration processes lead to flame wrinkle destruction, with a decay rate that is a nonlinear function of $\tilde{\varepsilon}$, as quantified in Eq. (6.25). As $\tilde{\mu}$ increases, increases in $\overline{\tilde{S}_{T,eff}}$ augment this effect, causing even faster increases in flame wrinkle decay rate, as shown by Figure 7.7. In order to

illustrate that the same basic scaling described in Eq. (7.34) applies in the low turbulence intensity case as well, Figure 7.14 plots the axial dependence of both $-\frac{\partial\left|\left\langle\tilde{\xi}(\tilde{s},\omega_0)\right\rangle\right|/\partial\tilde{s}}{\left|\left\langle\tilde{\xi}(\tilde{s},\omega_0)\right\rangle\right|^2}$ and $-\frac{\partial\left|\left\langle\tilde{\xi}(\tilde{s},\omega_0)\right\rangle\right|/\partial\tilde{s}}{\left|\left\langle\tilde{\xi}(\tilde{s},\omega_0)\right\rangle\right|}$. In the low turbulent intensity case ($\tilde{\mu}$=0.02 in Figure 7.14a), the ratio, $-\frac{\partial\left|\left\langle\tilde{\xi}(\tilde{s},\omega_0)\right\rangle\right|/\partial\tilde{s}}{\left|\left\langle\tilde{\xi}(\tilde{s},\omega_0)\right\rangle\right|^2}$ (the solid line) approaches a roughly constant value, while the ratio, $-\frac{\partial\left|\left\langle\tilde{\xi}(\tilde{s},\omega_0)\right\rangle\right|/\partial\tilde{s}}{\left|\left\langle\tilde{\xi}(\tilde{s},\omega_0)\right\rangle\right|}$, continues to evolve with downstream distance. For reference, note from Figure 7.14a that $\overline{\tilde{S}_{T,eff}}$ approaches a spatially constant value for $\tilde{s}$ >~10.

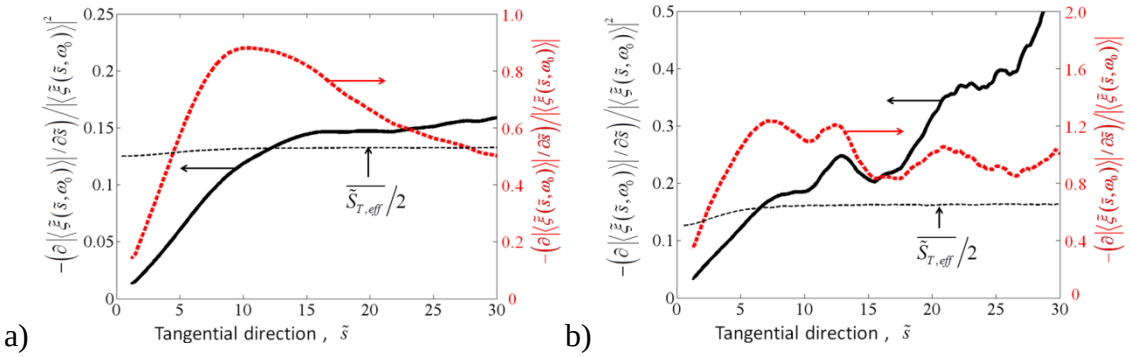

a) b)

Figure 7.14. Ratios of ensemble averaged flame slope and position, using two different scalings derived from kinematic restoration and stretch dominated solutions a) $\tilde{\mu}$=0.02 and b) $\tilde{\mu}$ =0.08 (Conditions are $\tilde{\varepsilon}$ =0.65, $\tilde{S}_L$ =0.25, and $\tilde{L}_{11}$ =0.65).

However, these increases in $\tilde{\mu}$ introduce the additional modulated flame speed effect as well, an effect that, in isolation, has a completely different amplitude scaling. Moreover,

this effect is also a function of $\tilde{\varepsilon}$, as larger modulations in $\tilde{c}$ occur as $\tilde{\varepsilon}$ increases. This dependence of $\tilde{S}_{T,eff}$ upon ensemble averaged curvature leads to wrinkle smoothing term that is linear in $\left|\left\langle \tilde{\xi}\left(\tilde{s},\omega_0\right)\right\rangle\right|$, as opposed to the nonlinear mechanism through which $\tilde{S}_{T,eff}$ exerts an influence. For $\left|\left\langle \tilde{\xi}\left(\tilde{s},\omega_0\right)\right\rangle\right|/\tilde{\varepsilon} \ll 1$ then, this linear effect dominates the nonlinear effect for large enough $\tilde{\mu}$. This can be seen from $\tilde{\mu}$=0.08 result in Figure 7.14b, where the axial dependence of the ratio $-\dfrac{\partial\left|\left\langle \tilde{\xi}\left(\tilde{s},\omega_0\right)\right\rangle\right|/\partial\tilde{s}}{\left|\left\langle \tilde{\xi}\left(\tilde{s},\omega_0\right)\right\rangle\right|^2}$ looks quite different from Figure 7.14a. Rather, than approaching a roughly constant value, it increases monotonically with downstream distance, even at location where $\overline{\tilde{S}_{T,eff}}$ is nearly constant. In contrast, the ratio, $-\dfrac{\partial\left|\left\langle \tilde{\xi}\left(\tilde{s},\omega_0\right)\right\rangle\right|/\partial\tilde{s}}{\left|\left\langle \tilde{\xi}\left(\tilde{s},\omega_0\right)\right\rangle\right|}$, which would be expected to approach a constant for the stretch dominated scaling approaches a nearly constant value.

In either the $\tilde{\mu}$=0.02 or 0.08 case, the scaling is not perfect as increases in $\tilde{\mu}$ influences both processes. However, the basic argument can be made more precise by replotting these same data. Specifically, Figure 7.15 plots the far field dependence of $-\partial\left|\left\langle \tilde{\xi}\left(\tilde{s},\omega_0\right)\right\rangle\right|/\partial\tilde{s}$ upon $\left|\left\langle \tilde{\xi}\left(\tilde{s},\omega_0\right)\right\rangle\right|$ for several $\tilde{\mu}$ values, where downstream distance is used as a parameter. Because $\left|\left\langle \tilde{\xi}\left(\tilde{s},\omega_0\right)\right\rangle\right|$ monotonically decreases with downstream distance, axial location decreases in the positive axial direction.

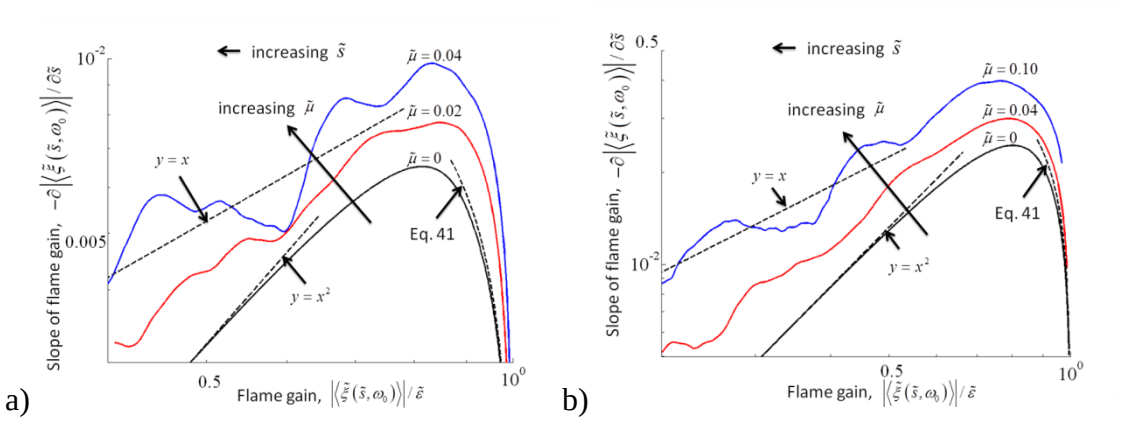

Figure 7.15. Relationship between local flame position and slope, illustrating transition from kinematic restoration dominated to "stretch" dominated with increasing turbulence intensity. a) $\tilde{\varepsilon}$ =0.32, b) $\tilde{\varepsilon}$ =0.65 ($\tilde{S}_L$ =0.25, and $\tilde{L}_{11}$ =0.65).

In the near field, Eq. (7.34) shows that for $\tilde{\mu}$ =0, the relationship between slope and position is described by the asymptotic result from Eqs. (6.15) and (7.34), which is given by:

$$\frac{\partial\left|\left\langle\tilde{\xi}(\tilde{s},\omega_0)\right\rangle\right|}{\partial\tilde{s}} \approx \tilde{S}_L\left|\left\langle\tilde{\xi}(\tilde{s},\omega_0)\right\rangle\right|^2\sqrt{\left(1-\left|\left\langle\tilde{\xi}(\tilde{s},\omega_0)\right\rangle\right|\right)/2} \tag{7.38}$$

In the far field, the variation in functional dependence of $-\partial\left|\left\langle\tilde{\xi}(\tilde{s},\omega_0)\right\rangle\right|/\partial\tilde{s}$ upon $\left|\left\langle\xi(\omega_0)\right\rangle\right|$ clearly transitions from the quadratic "kinematic restoration dominated" scaling (i.e., dominated by the $\tilde{S}_{T,eff}$ effect) to the linear stretch dominated scalings (i.e., dominated by the time varying $\tilde{S}_{T,eff}{}'$). Thus, these results show that the downstream decay of ensemble averaged flame wrinkling in the high turbulence intensity case is dominated by the modulation in the turbulent burning velocity, a result that is analogous to that associated with smoothing of thermodiffusively laminar flames.

CHAPTER 8

CONCLUSIONS AND FUTURE WORK

This chapter summarizes the results of this thesis and illustrates the key contributions to combustion research. Then, several suggestions are remarked for future work to better understand flame dynamics.

8.1 Concluding Remarks

Overall, this thesis focuses on the spatio/temporal dynamics of the flame response. Analytical and numerical analyses were performed to study excitations and dissipations of wrinkles on the flame front. These analyses identify key dimensionless parameters and provide insights in the complex problems. New findings were presented from chapter 4 through chapter 7.

Chapter 4 described the excitation of the flame response near the flame base. In this chapter, the asymptotic analysis was performed on the unsteady flame position motion, and the explicit form for the unsteady flame position was obtained. Two mechanisms exciting the flame response were studied. The first mechanism is the effect of the unsteady motion of the flame base. The analysis identifies that the flame wrinkle is generated by this unsteady motion of the flame base and then propagates downstream with the tangential velocity while maintaining the oscillation magnitude downstream. The second mechanism is the effect of the velocity fluctuations. The analysis indicates that the flame response increases linearly downstream by either harmonic or stochastic velocity fluctuations. Furthermore, the growth rate of the flame response is proportional

to the ratio of normal velocity disturbance to the tangential velocity. This relationship was verified with measurements from bluff-body stabilized flames.

Then, the study on the excitation was extended to further downstream with detailed velocity disturbance model in chapter 5. This chapter has described the features and parameters that control the spatio-temporal dynamics of flame front fluctuations of a harmonically excited flame. It has been shown that the magnitude of the flame response grows, reaches a peak or multiple peaks, and then decays with axial distance. The key point of this analysis was to demonstrate the important role of interference on the flame response, which is caused by multiple disturbances propagating in the same direction but at different velocities. Interference between waves propagating along the flame sheet is controlled by a ratio of two characteristic velocities; natural flame propagation speed and velocity disturbance speed. However, this interference can change by dissipations of the velocity disturbances. With high dissipation of a velocity fluctuation, the corresponding wave cannot invoke the interference, but rather renders the other wave to dominate. This domination leads to the constant magnitude of the flame response. Depending upon the relative values of these interference and dissipation parameters, the far field response can be categorized as "Interference dominated" or "Dissipation dominated". In the interference dominant regime, the flame response is oscillatory and possesses local maxima and minima. In the dissipation dominant regime, the flame response monotonically grows or exhibits no recognizable peak with the effective convection speed to flame convection speed.

In the following sections, analyses cover the dissipation mechanisms for the excited flame response, i.e., smoothing-out action of flame wrinkles. Chapter 6 is

devoted to the smooth-out of flame wrinkles in the laminar flames; the effects of flame stretch and kinematic restoration. This analysis identifies the key dimensionless parameters controlling stretch and kinematic restoration processes, as well as the conditions when one or the other is dominant. Kinematic restoration, an intrinsically nonlinear process, shows a two zone behavior in smoothing the flame wrinkle. The wrinkle on a flame excited with a single frequency decays quadratically in the near field at an amplitude dependent rate. The presence of multiple frequencies in the excitation, such as an additional harmonic, leads to a linear decay in near field amplitude. Thus, the harmonic content of the excitation plays an important role in the decay rate of flame wrinkles. In the far field, the wrinkle decays inversely with downstream distance at a rate that is independent of forcing amplitude. The smoothing of flame wrinkles by stretch effects in positive Markstein length reactants can be understood from linear analysis, which shows that the wrinkle decay rate is an exponential function of Markstein length and downstream distance.

Lastly, chapter 7 has described the relative contributions of deterministic and turbulent effects upon the dynamics of ensemble-averaged flame front with particular focus on the rate at which wrinkles excited by harmonic forcing are smoothed out and destroyed. In the near field, asymptotic results show the three leading order contributors, with phase jitter associated with random tangential convection of flame wrinkles being the leading order effect. Farther downstream, additional processes become important. First, the time averaged turbulent burning velocity, increases with downstream distance and turbulence intensity. This faster average displacement velocity of the front lead to increases in destruction of flame wrinkles.

In addition, the ensemble averaged turbulent burning velocity is modulated by the harmonic forcing, with an inverse dependence upon ensemble averaged flame curvature, i.e., the turbulent burning velocity changes in time. This effect is exactly analogous to positive Markstein length flames in the laminar flame case, but applies even to the ensemble averaged characteristics of stretch-insensitive turbulent flames. The degree of modulation of the effective turbulent flame speed is a function of the modulation amplitude in the flame curvature and, thus, is a function of wrinkle amplitude. It is also a function of turbulence intensity, as the effect disappears in the laminar case. This analysis shows that, depending upon turbulence intensity, the far field evolution of the ensemble-averaged flame response can be dominated by either mean and fluctuation parts of the effective turbulent flame speed. These two characteristics are analogous to that of stretch-sensitive laminar flames, whose downstream wrinkle decay rate can be controlled by either kinematic restoration of stretch effects.

8.2 Summary of Key Contributions

This thesis describes the local response of premixed flames subject to harmonic velocity disturbance. The analyses were performed in various angles. Hopf-Lax formula was used in providing an exact explicit solution for a nonlinear problem. Overall, the third order asymptotic analysis was performed to capture the effect of nonlinearities. For the highly nonlinear and stochastic processes, numerical calculation was implemented for the exact solutions. These numerical solutions along with asymptotic analysis provide in-depth insights to the dynamics of the flame. Also, models developed with the asymptotic analysis were validated with the measurements.

The first key finding is identifying the fundamental relationship between the velocity excitation and the flame response. When the flame wrinkle is excited by the unsteady velocity fluctuation, the growth rate of the flame response is proportional to the ratio of the normal velocity fluctuation to the mean tangential velocity. This relationship is validated with several flame measurements.

The second finding is identifying the role of interference and dissipation effects on the flame response. It was found out that if the velocity fluctuation persists further downstream, the flame response shows oscillatory gain due to the interference between different disturbance waves. This interference pattern helps to find the axial location of the maximum flame response, which is proven by the measurement. On the contrary, if the velocity fluctuation dissipates quickly further downstream, the interference pattern disappears. Rather, the flame response shows constant magnitude. Furthermore, this thesis provides criteria indicating the importance of either interference and dissipation effect.

Last set of findings are related with the dissipation of the flame response. This thesis studied three mechanisms in smoothing out the wrinkles on flames, and identified key dimensionless parameters. Importantly, the analyses provide simple illustrations in understanding the role of individual mechanisms. Dissipation mechanisms include the kinematic restoration, the flame stretch, and the turbulent flow effects. We found the role of the leading edges of the flame front by the kinematic restoration. Next, positive Markstein length effect is the linear effect and it was compared against the kinematic restoration effect. The turbulent flow effect was the most challenging problem. The third order asymptotic analysis identifies the leading order effect on the dynamics of the

ensemble-averaged flame front. The phase jitter effect is found out to be the leading order effect, which is different from previous speculation. As moving downstream, the concept of the effective turbulent flame speed is introduced to simplify the dynamics of the ensemble-averaged flame front. This effective turbulent flame speed is higher than the laminar flame speed, and produces the modulation by the harmonic excitation. This modulation is found to have a linear relationship with the curvatures of the ensemble averaged flame front.

8.3 Recommendations for Future Work

First, it is important to develop an approach which can handle multi-valued flame position analytically. A Flame front easily becomes multi-valued because of strong vortices which wind up the flame front. Furthermore, the strong turbulent flow increases occurrence of the multi-valued flame front; pocket formations and detached flame front occur frequently in the turbulent combustion. However, the incapability in capturing multi-valued flame front can plague the prediction capability of the heat release. For example, if a flame front is rolled up by a strong vortex, the single valued flame front analysis cannot capture major amount of heat release produced by rolling-up. Therefore it is crucial to develop analytic tools to capture multi-valued flame front.

The next suggestion is to obtain sufficient amounts of measurements to validate the G-equation approach. G-equation is very promising tool to understand the dynamics of the flame. However, this approach should be thoroughly validated under real applications. G-equation relates the motion of the flame fronts with the laminar flame

speed and velocities right at the flame front. Therefore, it is crucial to obtain the high space/time resolved flame measurement along with simultaneous velocity measurement.

Thirdly, this thesis used a dynamic equation for the ensemble averaged flame front. From the numerical results, it was suggested that the effective turbulent flame speed has a strong correlation with the curvature of the ensemble-averaged flame fronts. However, this correlation shows a scattered ellipsoid. This suggests that the effective turbulent flame speed shows a certain phase lag. This phase lag might originate from the nonlinear convective operators. Therefore, there will be a correction to the ensemble average equation including this correction by the phase lag.

Lastly, this analysis suggested that the effective flame speed has curvature dependence, and this curvature dependency increases with the turbulent intensity. It will be ideal to perform a thorough analysis to quantify the effect of the turbulent intensity, as well as other parameters such as integral length scales, and magnitudes of harmonic forcing.

APPENDIX A

The example in the Section 3.2 analyzed the flame response to a step-increase in flow velocity and showed that this leads to a cusp, or "shock" on the flame. Here, we will consider a step decrease in flow velocity, which leads to an "expansion wave" type solution. The boundary condition and initial condition for *g* are following:

$$g = \begin{cases} g_{init} = \dfrac{S_L}{\sqrt{{u_{x,a}}^2 - S_L}} & x \geq 0, \;\; t = 0 \\ g_{bound} = \dfrac{S_L}{\sqrt{{u_{x,b}}^2 - S_L}} & x = 0, \;\; t \geq 0 \end{cases} \tag{A.1}$$

where g_{init} and g_{bound} represents the initial condition and boundary condition, respectively. The governing equation is:

$$\frac{\partial g}{\partial t} + \left(u_{x,b} - \frac{S_L \cdot g}{\sqrt{1+g^2}} \right) \frac{\partial g}{\partial y} = 0 \tag{A.2}$$

Eq. (A.2) can be solved by the method of characteristics to yield the solution:

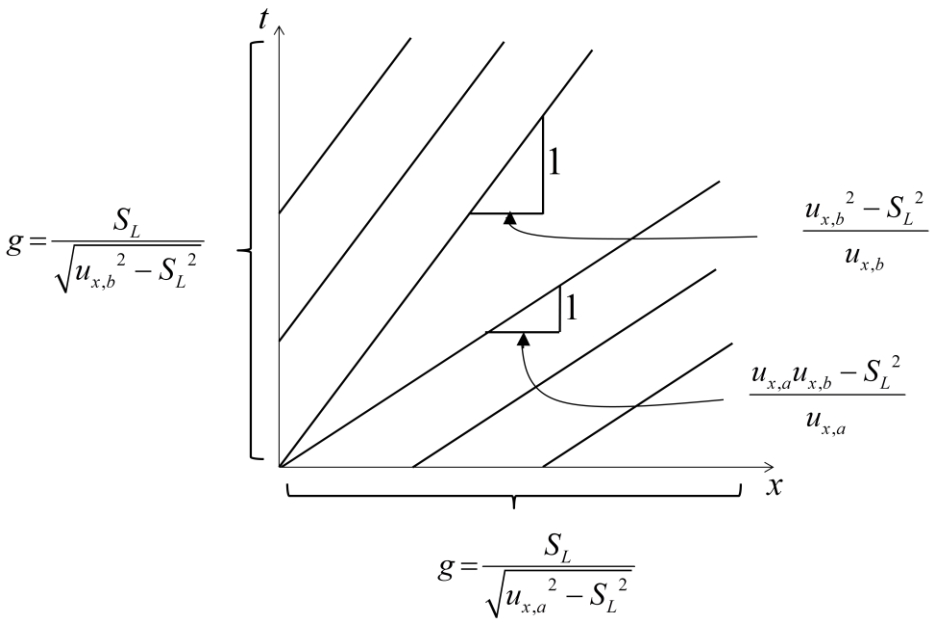

Figure A0.1 Illustration of space-time evolution of solution characteristics

$$g=\begin{cases}\dfrac{S_L}{\sqrt{u_{x,b}^2-S_L^2}} & x<\dfrac{u_{x,b}^2-S_L^2}{u_{x,b}}\cdot t \\ \dfrac{S_L}{\sqrt{u_{x,a}^2-S_L^2}} & \dfrac{u_{x,a}u_{x,b}-S_L^2}{u_{x,a}}\cdot t<x\end{cases} \tag{A.3}$$

To complete the solution, we must solve for the "expansion wave region", $t\cdot\left(u_{x,b}^2-S_L^2\right)/u_{x,b}\le x\le t\cdot\left(u_{x,a}u_{x,b}-S_L^2\right)/u_{x,a}$. The solution in this region is non-unique (in reality, the finite thickness of the flame would cause this discontinuity to be smoothed out, rendering the solution unique). Following an analogous procedure to expansion fan solutions to the Burger's equation [56], a smooth solution can be obtained assuming $g=F\left(y/t\right)$. For this exercise only, we use $\eta=x/t$:

$$\eta=\frac{x}{t},\ g=F\left(\eta\right) \tag{A.4}$$

Then, derivatives of g can be written in terms of F as:

$$\frac{\partial g}{\partial t} = \left(-\frac{\eta}{t}\right) \times \frac{dF}{d\eta}, \frac{\partial g}{\partial x} = t \times \frac{dF}{d\eta} \tag{A.5}$$

Substitute Eq. (A.4) and (A.5) into Eq. (A.2) leads to:

$$\left(-\frac{\eta}{t}\right) \times \frac{dF}{d\eta} + \left(u_{x,b} - \frac{S_L \cdot F}{\sqrt{1+F^2}}\right) \cdot \frac{1}{t} \cdot \frac{dF}{d\eta} = 0 \tag{A.6}$$

Eq. (A.6) is re-arranged as following:

$$\frac{1}{t}\frac{dF}{d\eta} \times \left[-\eta + u_{x,b} - \frac{S_L \cdot F}{\sqrt{1+F^2}}\right] = 0 \tag{A.7}$$

One possible solution of Eq. (A.7) is $dF/d\eta = 0$. However this is not a smooth continuous solution in the entire domain. The other possible solution is:

$$\frac{S_L \cdot F}{\sqrt{1+F^2}} = u_{x,b} - \eta \tag{A.8}$$

Solving Eq. (A.8) results in:

$$F = \frac{u_{x,b} - \eta}{\sqrt{{S_L}^2 - \left(u_{x,b} - \eta\right)^2}} \tag{A.9}$$

Express Eq. (A.9) in terms of x, t, and g resulting in:

$$g = \frac{u_{x,b} \cdot t - x}{\sqrt{\left(S_L \cdot t\right)^2 + \left(u_{x,b} \cdot t - x\right)^2}} \tag{A.10}$$

Therefore combining Eq. (A.1), (A.3) and (A.10), the solution is:

$$g = \begin{cases} \dfrac{S_L}{\sqrt{{u_{x,b}}^2 - {S_L}^2}} & x < \dfrac{{u_{x,b}}^2 - {S_L}^2}{u_{x,b}} \cdot t \\ \dfrac{u_{x,b} \cdot t - x}{\sqrt{\left(S_L \cdot t\right)^2 + \left(u_{x,b} \cdot t - x\right)^2}} & \dfrac{{u_{x,b}}^2 - {S_L}^2}{u_{x,b}} \cdot t \le x \le \dfrac{u_{x,a}u_{x,b} - {S_L}^2}{u_{x,a}} \cdot t \\ \dfrac{S_L}{\sqrt{{u_{x,a}}^2 - {S_L}^2}} & \dfrac{u_{x,a}u_{x,b} - {S_L}^2}{u_{x,a}} \cdot t < x \end{cases} \tag{A.11}$$

APPENDIX B

The Lax Friedrich Flux scheme [60] is derived for the flame kinematic equation. For the simple illustration, use a 2D version of Eq. (3.2), which is written as:

$$\frac{\partial \xi}{\partial t} + \underbrace{u_x \frac{\partial \xi}{\partial x} - u_y - S_L \sqrt{1+\left(\frac{\partial \xi}{\partial x}\right)^2}}_{\equiv H\left(\frac{\partial \xi}{\partial x}\right)} = 0 \tag{B.1}$$

For convenience, define a function, *H*, as:

$$H\left(\frac{\partial \xi}{\partial x}\right) = u_x \frac{\partial \xi}{\partial x} - u_y - S_L \sqrt{1+\left(\frac{\partial \xi}{\partial x}\right)^2} \tag{B.2}$$

Then, the Local Lax Friedrich flux, $\hat{H}^{LLF}$, is:

$$\hat{H}^{LLF}\left(\frac{\partial \xi^+}{\partial x}, \frac{\partial \xi^-}{\partial x}\right) = H\left(\frac{1}{2}\left(\frac{\partial \xi^+}{\partial x} + \frac{\partial \xi^-}{\partial x}\right)\right) - \alpha\left(\frac{\partial \xi^+}{\partial x}, \frac{\partial \xi^-}{\partial x}\right) \cdot \frac{1}{2}\left(\frac{\partial \xi^+}{\partial x} + \frac{\partial \xi^-}{\partial x}\right) \tag{B.3}$$

where the superscript '+' and '-' represent the derivate evaluated using the right and left stencils, respectively. The function, α, is defined as:

$$\alpha\left(\frac{\partial \xi^+}{\partial x}, \frac{\partial \xi^-}{\partial x}\right) = \max\left(\left|H_1\left(\frac{\partial \xi^+}{\partial x}\right)\right|, \left|H_1\left(\frac{\partial \xi^-}{\partial x}\right)\right|\right) \tag{B.4}$$

where, H_1 is defined as:

$$H_1\left(\frac{\partial \xi}{\partial x}\right) = u_x - S_L \frac{\partial \xi}{\partial x} \Bigg/ \sqrt{1+\left(\frac{\partial \xi}{\partial x}\right)^2} \tag{B.5}$$

Note that we used the property that H_1 does not have local maxima inside the domain in order to arrive at the simple expression as in Eq. (B.4).

APPENDIX C

This section analyzes the far field behavior of the flame wrinkles due to kinematic restoration effects. This is done most easily by considering the initial value problem illustrated in Figure C0.1. This initial value problem closely simulates the boundary value problem of interest to this section for an observer in a reference frame moving at a speed of $u_{s,0}$ along the flame, as long as wrinkles decay over a length scale that is long relative to their wavelength.

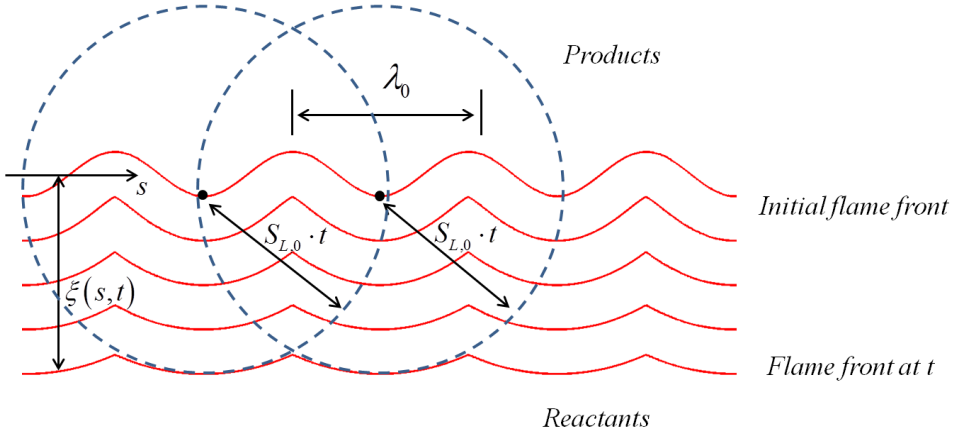

Figure C0.1. Initial value problem showing a constant burning velocity, sinusoidal flame propagating into a quiescent flow.

The governing equation for the flame position is:

$$\frac{\partial \xi}{\partial t} + S_{L,0}\sqrt{1+\left(\frac{\partial \xi}{\partial s}\right)^2} = 0 \qquad \text{(C.1)}$$

The general solution of Eq. (C.1) with the initial value, ξ_{init}, is described by the Hopf-Lax formula [114]:

$$\xi(s,t) = \min_{s-S_{L,0}t \,<\, s^* \,<\, s+S_{L,0}t} \left(\xi_{init}(s^*) - \sqrt{(S_{L,0}t)^2 - (s-s^*)^2} \right) \qquad \text{(C.2)}$$

This solution shows that the flame position is defined by the leading edge of a series of arcs originating from the initial flame front (i.e., Huygen's propagation [57]). After an initial transient, the flame asymptotes to a far field solution that is controlled by the leading edges of the flame, and has a shape which equals the arcs radiating out from these leading edges as shown in Figure C0.1. The position of the periodic arcs are given by:

$$\xi(s,t) = \sqrt{\left(S_{L,0}t\right)^2 - s^2} \tag{C.3}$$

The corresponding spatial Fourier transform of a periodic array of these arcs is given by:

$$\left|\xi\left(k = 2\pi / \lambda_0\right)\right| \approx \frac{{\lambda_0}^2}{2\pi^2 \cdot S_{L,0}t} \tag{C.4}$$

This temporal problem can be converted into a spatial one by substituting the wavelength, λ_0 and the time, *t*, with $u_{s,0} / f_0$ and $s / u_{s,0}$ which results in the following expression:

$$\left|\tilde{\xi}\left(\omega = \omega_0\right)\right| \approx \frac{2}{\tilde{S}_{L,0}\tilde{s}} \tag{C.5}$$

APPENDIX D

Let consider 1D flame front dynamics. ξ is random variable representing a flame position in one dimension (x-coordinate) with a PDF of $f(\xi)$ and c is a progress variable defined as:

$$\begin{aligned} c_x(\xi) &= \begin{cases} 1 & x \le \xi \\ 0 & x > \xi \end{cases} \\ &= 1 - H(x-\xi) \end{aligned} \tag{D.1}$$

Mean of the progress variable is defined as

$$\bar{c}(x) = \int_0^\infty c_x(\xi) \cdot f(\xi) d\xi \;\; = \int_0^\infty \left[1 - H(x-\xi)\right] \cdot f(\xi) d\xi \tag{D.2}$$

where, H is a Heaviside function. Since the Heaviside function can be expressed as an integral form of Dirac delta function as following:

$$H(x-\xi) = \int_0^x \delta(\sigma - \xi) d\sigma \tag{D.3}$$

After plugging Eq. (D.3) into Eq. (D.2), it results into:

$$\begin{aligned} \bar{c}(x) = & \int_0^\infty \left[1 - \int_0^x \delta(\sigma-\xi) d\sigma\right] \cdot f(\xi) d\xi \\ &= \int_0^\infty f(\xi) d\xi - \int_0^\infty \int_0^x \delta(\sigma-\xi) d\sigma \cdot f(\xi) d\xi \\ &= 1 - \int_0^\infty \int_0^x \delta(\sigma-\xi) d\sigma \cdot f(\xi) d\xi \end{aligned} \tag{D.4}$$

The second term in RHS of Eq. (D.4) can be rewritten as following:

$$\begin{aligned} \int_0^\infty \int_0^x \delta(\sigma-\xi) d\sigma \cdot f(\xi) d\xi \;\; &= \int_0^\infty \int_0^x \delta(\sigma-\xi) f(\xi) d\sigma d\xi \\ &= \int_0^x \left[\int_0^\infty \delta(\sigma-\xi) f(\xi) d\xi \right] d\sigma \\ &= \int_0^x f(\sigma) \; d\sigma \end{aligned} \tag{D.5}$$

As a result, combining Eq. (D.4) and Eq. (D.5) and switch dummy variable σ into ξ, then we get following:

$$\overline{c}\left(x\right) = 1 - \int_0^x f\left(\xi\right) d\xi \tag{D.6}$$

Therefore, the mean of a progress variable at *x* represents the cumulative density function.

APPENDIX E

Asymptotic expansion give series of partial differential equation in terms of ε and σ as following:

$$O(\varepsilon):\ \frac{\partial \xi_{\varepsilon}}{\partial t} + u_0 \frac{\partial \xi_{\varepsilon}}{\partial x} = 0 \tag{E.1}$$

$$O(\sigma):\ \frac{\partial \xi_{\sigma}}{\partial t} + u_0 \frac{\partial \xi_{\sigma}}{\partial x} = 0 \tag{E.2}$$

$$O(\varepsilon^2):\ \frac{\partial \xi_{\varepsilon\varepsilon}}{\partial t} + u_0 \frac{\partial \xi_{\varepsilon\varepsilon}}{\partial x} = \frac{s_{L,0}}{2}\left(\frac{\partial \xi_{\varepsilon}}{\partial x}\right)^2 \tag{E.3}$$

$$O(\varepsilon\sigma):\ \frac{\partial \xi_{\varepsilon\sigma}}{\partial t} + u_0 \frac{\partial \xi_{\varepsilon\sigma}}{\partial x} = s_{L,0} \frac{\partial^2 \xi_{\varepsilon}}{\partial x^2} + s_{L,0} \frac{\partial \xi_{\varepsilon}}{\partial x}\frac{\partial \xi_{\sigma}}{\partial x} \tag{E.4}$$

$$O(\sigma^2):\ \frac{\partial \xi_{\sigma\sigma}}{\partial t} + u_0 \frac{\partial \xi_{\sigma\sigma}}{\partial x} = s_{L,0} \frac{\partial^2 \xi_{\sigma}}{\partial x^2} + \frac{s_{L,0}}{2}\left(\frac{\partial \xi_{\sigma}}{\partial x}\right)^2 \tag{E.5}$$

$$O(\varepsilon^3):\ \frac{\partial \xi_{\varepsilon\varepsilon\varepsilon}}{\partial t} + u_0 \frac{\partial \xi_{\varepsilon\varepsilon\varepsilon}}{\partial x} = s_{L,0} \frac{\partial \xi_{\varepsilon}}{\partial x}\frac{\partial \xi_{\varepsilon\varepsilon}}{\partial x} \tag{E.6}$$

$$O(\varepsilon^2\sigma):\ \frac{\partial \xi_{\varepsilon\varepsilon\sigma}}{\partial t} + u_0 \frac{\partial \xi_{\varepsilon\varepsilon\sigma}}{\partial x} = s_{L,0} \frac{\partial^2 \xi_{\varepsilon\varepsilon}}{\partial x^2} + s_{L,0} \frac{\partial \xi_{\varepsilon}}{\partial x}\frac{\partial \xi_{\varepsilon\sigma}}{\partial x} + s_{L,0} \frac{\partial \xi_{\varepsilon\varepsilon}}{\partial x}\frac{\partial \xi_{\sigma}}{\partial x} \tag{E.7}$$

$$O(\varepsilon\sigma^2):\ \frac{\partial \xi_{\varepsilon\sigma\sigma}}{\partial t} + u_0 \frac{\partial \xi_{\varepsilon\sigma\sigma}}{\partial x} = s_{L,0} \frac{\partial^2 \xi_{\varepsilon\sigma}}{\partial x^2} + s_{L,0} \frac{\partial \xi_{\sigma}}{\partial x}\frac{\partial \xi_{\varepsilon\sigma}}{\partial x} + s_{L,0} \frac{\partial \xi_{\varepsilon}}{\partial x}\frac{\partial \xi_{\sigma\sigma}}{\partial x} \tag{E.8}$$

$$O(\sigma^3):\ \frac{\partial \xi_{\sigma\sigma\sigma}}{\partial t} + u_0 \frac{\partial \xi_{\sigma\sigma\sigma}}{\partial x} = s_{L,0} \frac{\partial \xi_{\sigma}}{\partial x}\frac{\partial \xi_{\sigma\sigma}}{\partial x} + s_{L,0} \frac{\partial^2 \xi_{\sigma\sigma}}{\partial x^2} \tag{E.9}$$

In addition, higher order expansions for ε are:

$$O(\varepsilon^4):\ \frac{\partial \xi_{\varepsilon\varepsilon\varepsilon\varepsilon}}{\partial t} + u_0 \frac{\partial \xi_{\varepsilon\varepsilon\varepsilon\varepsilon}}{\partial x} = s_{L,0}\left(\frac{\partial \xi_{\varepsilon}}{\partial x}\frac{\partial \xi_{\varepsilon\varepsilon\varepsilon}}{\partial x} + \frac{1}{2}\left(\frac{\partial \xi_{\varepsilon\varepsilon}}{\partial x}\right)^2 - \frac{1}{8}\left(\frac{\partial \xi_{\varepsilon}}{\partial x}\right)^4\right) \tag{E.10}$$

$$O\left(\varepsilon^5\right):\ \frac{\partial \xi_{\varepsilon\varepsilon\varepsilon\varepsilon\varepsilon}}{\partial t}+u_0\frac{\partial \xi_{\varepsilon\varepsilon\varepsilon\varepsilon\varepsilon}}{\partial x}=\ s_{L,0}\left(\frac{\partial \xi_\varepsilon}{\partial x}\frac{\partial \xi_{\varepsilon\varepsilon\varepsilon\varepsilon}}{\partial x}+\frac{\partial \xi_{\varepsilon\varepsilon}}{\partial x}\frac{\partial \xi_{\varepsilon\varepsilon\varepsilon}}{\partial x}-\frac{1}{2}\left(\frac{\partial \xi_\varepsilon}{\partial x}\right)^3\frac{\partial \xi_{\varepsilon\varepsilon}}{\partial x}\right) \tag{E.11}$$

Then, each solutions are solved sequentially with the flame boundary condition of:

$$\xi\left(x=0,t\right)=\varepsilon\cdot\cos\left(\omega_0 t\right) \tag{E.12}$$

Then, the solutions are:

$$\xi_\varepsilon=\cos\left(\omega_0\left(t-x/u_0\right)\right) \tag{E.13}$$

$$\xi_\sigma=0 \tag{E.14}$$

$$\xi_{\varepsilon\varepsilon}=\frac{s_{L,0}\omega_0}{4{u_0}^2}\cdot\left[\frac{\omega_0 x}{u_0}+\frac{\omega_0 x}{u_0}\cdot\cos\left(2\omega_0\left(t-x/u_0\right)\right)\right] \tag{E.15}$$

$$\xi_{\varepsilon\varepsilon}=\frac{s_{L,0}\omega_0}{4{u_0}^2}\cdot\left[\frac{\omega_0 x}{u_0}+\frac{\omega_0 x}{u_0}\cdot\cos\left(2\omega_0\left(t-x/u_0\right)\right)\right] \tag{E.16}$$

$$\xi_{\varepsilon\sigma}=-\left(\frac{s_{L,0}\omega_0}{{u_0}^2}\right)\left(\frac{\omega_0 x}{u_0}\right)\cdot\sin\left(\omega\left(t-x/u_0\right)\right) \tag{E.17}$$

$$\xi_{\sigma\sigma}=0 \tag{E.18}$$

$$\xi_{\varepsilon\varepsilon\varepsilon}=-\frac{1}{8}\left(\frac{s_{L,0}}{u_0}\frac{\omega_0}{u_0}\right)^2\times\left[\begin{array}{l}3\frac{\omega_0 x}{u_0}\cos\left(\omega_0\left(t-\frac{x}{u_0}\right)\right)+\left(\frac{\omega_0 x}{u_0}\right)^2\sin\left(\omega_0\left(t-\frac{x}{u_0}\right)\right)\\+\frac{\omega_0 x}{u_0}\cos\left(3\omega_0\left(t-\frac{x}{u_0}\right)\right)+\left(\frac{\omega_0 x}{u_0}\right)^2\sin\left(3\omega_0\left(t-\frac{x}{u_0}\right)\right)\end{array}\right] \tag{E.19}$$

$$\xi_{\varepsilon\varepsilon\sigma}=\left(\frac{s_{L,0}}{u_0}\frac{\omega_0}{u_0}\right)^2\cdot\left[\begin{array}{l}-\frac{1}{4}\left(\frac{\omega_0 x}{u_0}\right)^2+\ \frac{3}{2}\frac{\omega_0 x}{u_0}\sin\left(2\omega_0\left(t-x/u_0\right)\right)\\-\frac{3}{4}\left(\frac{\omega_0 x}{u_0}\right)^2\cos\left(2\omega_0\left(t-x/u_0\right)\right)\end{array}\right] \tag{E.20}$$

$$\xi_{\varepsilon\sigma\sigma}=\left(\frac{s_{L,0}}{u_0}\frac{\omega_0}{u_0}\right)^2\left[2\frac{\omega_0 x}{u_0}\cdot\cos\left(\omega_0\left(t-x/u_0\right)\right)+\frac{1}{2}\left(\frac{\omega_0 x}{u_0}\right)^2\cdot\sin\left(\omega_0\left(t-x/u_0\right)\right)\right] \tag{E.21}$$

$$\xi_{\sigma\sigma\sigma} = 0 \tag{E.22}$$

$$\begin{aligned}
\xi_{\varepsilon\varepsilon\varepsilon\varepsilon} &= -\frac{3}{64} S_{L,0} x + \frac{15}{64} {S_{L,0}}^3 x \\
&+ \left(\frac{1}{16} S_{L,0} x + \frac{1}{12} {S_{L,0}}^3 x^3 - \frac{5}{16} {S_{L,0}}^3 x \right) \cos\left(2\omega_0 \left(t - x/u_0\right)\right) \\
&- \frac{3}{8} {S_{L,0}}^3 x^2 \sin\left(2\omega_0 \left(t - x/u_0\right)\right) \\
&+ \left(-\frac{1}{64} S_{L,0} x + \frac{5}{64} {S_{L,0}}^3 x - \frac{1}{12} {S_{L,0}}^3 x^3 \right) \cos\left(4\omega_0 \left(t - x/u_0\right)\right) \\
&+ \frac{3}{16} {S_{L,0}}^3 x^2 \sin\left(4\omega_0 \left(t - x/u_0\right)\right)
\end{aligned} \tag{E.23}$$

$$\begin{aligned}
\xi_{\varepsilon\varepsilon\varepsilon\varepsilon\varepsilon} &= \left(-\frac{15}{64} {S_{L,0}}^2 x - \frac{3}{32} {S_{L,0}}^4 x^3 + \frac{35}{16} {S_{L,0}}^4 x \right) \sin\left(\omega_0 \left(t - x/u_0\right)\right) \\
&+ \left(\frac{1}{192} {S_{L,0}}^4 x^4 + \frac{1}{16} {S_{L,0}}^2 x^2 - \frac{29}{64} {S_{L,0}}^4 x^2 \right) \cos\left(\omega_0 \left(t - x/u_0\right)\right) \\
&+ \left(\frac{27}{64} {S_{L,0}}^4 x^3 - \frac{35}{128} {S_{L,0}}^4 x + \frac{15}{128} {S_{L,0}}^2 x \right) \sin\left(3\omega_0 \left(t - x/u_0\right)\right) \\
&+ \left(-\frac{9}{128} {S_{L,0}}^4 x^4 - \frac{3}{32} {S_{L,0}}^2 x^2 + \frac{87}{128} {S_{L,0}}^4 x^2 \right) \cos\left(3\omega_0 \left(t - x/u_0\right)\right) \\
&+ \left(-\frac{3}{128} {S_{L,0}}^2 x - \frac{15}{64} {S_{L,0}}^4 x^3 + \frac{7}{128} {S_{L,0}}^4 x \right) \sin\left(5\omega_0 \left(t - x/u_0\right)\right) \\
&+ \left(\frac{1}{32} {S_{L,0}}^2 x^2 + \frac{25}{384} {S_{L,0}}^4 x^4 - \frac{29}{128} {S_{L,0}}^4 x^2 \right) \cos\left(5\omega_0 \left(t - x/u_0\right)\right)
\end{aligned} \tag{E.24}$$

APPENDIX F

Asymptotic expansions give series of partial differential equation in terms of ε and σ as following:

$$O(\varepsilon):\ \frac{\partial \xi_\varepsilon}{\partial t} + u_0 \frac{\partial \xi_\varepsilon}{\partial x} = 0 \tag{F.1}$$

$$O(\mu):\ \frac{\partial \xi_\mu}{\partial t} + u_0 \frac{\partial \xi_\mu}{\partial x} = v \tag{F.2}$$

$$O(\varepsilon^2):\ \frac{\partial \xi_{\varepsilon\varepsilon}}{\partial t} + u_0 \frac{\partial \xi_{\varepsilon\varepsilon}}{\partial x} = \frac{S_{L,0}}{2}\left(\left(\frac{\partial \xi_\varepsilon}{\partial x}\right)^2 + \left(\frac{\partial \xi_\varepsilon}{\partial z}\right)^2\right) \tag{F.3}$$

$$O(\varepsilon\mu):\ \frac{\partial \xi_{\varepsilon\mu}}{\partial t} + u_0 \frac{\partial \xi_{\varepsilon\mu}}{\partial x} = S_{L,0}\left(\frac{\partial \xi_\varepsilon}{\partial z}\frac{\partial \xi_\mu}{\partial z} + \frac{\partial \xi_\varepsilon}{\partial x}\frac{\partial \xi_\mu}{\partial x}\right) - u\frac{\partial \xi_\varepsilon}{\partial x} + \frac{\partial v}{\partial y}\xi_\varepsilon - w\frac{\partial \xi_\varepsilon}{\partial z} \tag{F.4}$$

$$O(\mu^2):\ \frac{\partial \xi_{\mu\mu}}{\partial t} + u_0 \frac{\partial \xi_{\mu\mu}}{\partial x} = \frac{S_{L,0}}{2}\left(\left(\frac{\partial \xi_\mu}{\partial z}\right)^2 + \left(\frac{\partial \xi_\mu}{\partial x}\right)^2\right) - u\frac{\partial \xi_\mu}{\partial x} + \frac{\partial v}{\partial y}\xi_\mu - w\frac{\partial \xi_\mu}{\partial z} \tag{F.5}$$

$$O(\varepsilon^3):\ \frac{\partial \xi_{\varepsilon\varepsilon\varepsilon}}{\partial t} + u_0 \frac{\partial \xi_{\varepsilon\varepsilon\varepsilon}}{\partial x} = S_{L,0}\left(\frac{\partial \xi_\varepsilon}{\partial x}\frac{\partial \xi_{\varepsilon\varepsilon}}{\partial x} + \frac{\partial \xi_\varepsilon}{\partial z}\frac{\partial \xi_{\varepsilon\varepsilon}}{\partial z}\right) \tag{F.6}$$

$$\begin{aligned} O(\varepsilon^2\mu):\ &\frac{\partial \xi_{\varepsilon\varepsilon\mu}}{\partial t} + u_0 \frac{\partial \xi_{\varepsilon\varepsilon\mu}}{\partial x} = S_{L,0}\left(\frac{\partial \xi_\varepsilon}{\partial x}\frac{\partial \xi_{\varepsilon\mu}}{\partial x} + \frac{\partial \xi_\mu}{\partial x}\frac{\partial \xi_{\varepsilon\varepsilon}}{\partial x} + \frac{\partial \xi_\varepsilon}{\partial z}\frac{\partial \xi_{\varepsilon\mu}}{\partial z} + \frac{\partial \xi_\mu}{\partial z}\frac{\partial \xi_{\varepsilon\varepsilon}}{\partial z}\right) \\ &-\frac{\partial u'}{\partial y}\xi_\varepsilon\frac{\partial \xi_\varepsilon}{\partial x} - \frac{\partial w'}{\partial y}\xi_\varepsilon\frac{\partial \xi_\varepsilon}{\partial z} + \frac{\partial v'}{\partial y}\xi_{\varepsilon\varepsilon} + \frac{1}{2}\frac{\partial^2 v'}{\partial y^2}(\xi_\varepsilon)^2 - w'\frac{\partial \xi_{\varepsilon\varepsilon}}{\partial z} - u'\frac{\partial \xi_{\varepsilon\varepsilon}}{\partial x} \end{aligned} \tag{F.7}$$

$$\begin{aligned} O(\varepsilon\mu^2):\ &\frac{\partial \xi_{\varepsilon\mu\mu}}{\partial t} + u_0 \frac{\partial \xi_{\varepsilon\mu\mu}}{\partial x} = S_{L,0}\left(\frac{\partial \xi_\mu}{\partial x}\frac{\partial \xi_{\varepsilon\mu}}{\partial x} + \frac{\partial \xi_\varepsilon}{\partial x}\frac{\partial \xi_{\mu\mu}}{\partial x} + \frac{\partial \xi_\mu}{\partial z}\frac{\partial \xi_{\varepsilon\mu}}{\partial z} + \frac{\partial \xi_\varepsilon}{\partial z}\frac{\partial \xi_{\mu\mu}}{\partial z}\right) \\ &+\frac{\partial v'}{\partial y}\xi_{\varepsilon\mu} + \frac{\partial^2 v'}{\partial y^2}\xi_\varepsilon\xi_\mu - \frac{\partial w'}{\partial y}\xi_\mu\frac{\partial \xi_\varepsilon}{\partial z} - \frac{\partial w'}{\partial y}\xi_\varepsilon\frac{\partial \xi_\mu}{\partial z} - w'\frac{\partial \xi_{\varepsilon\mu}}{\partial z} - \frac{\partial u'}{\partial y}\xi_\mu\frac{\partial \xi_\varepsilon}{\partial x} - \frac{\partial u'}{\partial y}\xi_\varepsilon\frac{\partial \xi_\mu}{\partial x} - u'\frac{\partial \xi_{\varepsilon\mu}}{\partial x} \end{aligned} \tag{F.8}$$

$$O\left(\mu^3\right):\ \frac{\partial \xi_{\mu\mu\mu}}{\partial t}+u_0\frac{\partial \xi_{\mu\mu\mu}}{\partial x}=S_{L,0}\left(\frac{\partial \xi_\mu}{\partial x}\frac{\partial \xi_{\mu\mu}}{\partial x}+\frac{\partial \xi_\mu}{\partial z}\frac{\partial \xi_{\mu\mu}}{\partial z}\right)-\frac{\partial u'}{\partial y}\xi_\mu\frac{\partial \xi_\mu}{\partial x}+\frac{1}{2}\frac{\partial^2 v'}{\partial y^2}\left(\xi_\mu\right)^2 \\ +\frac{\partial v'}{\partial y}\xi_{\mu\mu}-\frac{\partial w'}{\partial y}\xi_\mu\frac{\partial \xi_\mu}{\partial z}-w'\frac{\partial \xi_{\mu\mu}}{\partial z}-u'\xi_\mu\frac{\partial \xi_{\mu\mu}}{\partial x} \tag{F.9}$$

APPENDIX G

With the specified boundary condition in Eq. (6.18), the flame position is obtained as:

$$\begin{aligned}\frac{\tilde{\xi}(\tilde{s},t)}{\tilde{\varepsilon}} = &\left[a_1 + \frac{\tilde{\varepsilon}\tilde{S}_{L,0}\tilde{s}}{2}\sum_{n=1}^{\infty} n(n+1)\cdot\left(a_n a_{n+1} + b_n b_{n+1}\right)\right]\cdot\cos\left(\tilde{t}-\tilde{s}\right)\\ &\left[b_1 + \frac{\tilde{\varepsilon}\tilde{S}_{L,0}\tilde{s}}{2}\sum_{n=1}^{\infty} n(n+1)\cdot\left(a_n b_{n+1} - b_n a_{n+1}\right)\right]\cdot\sin\left(\tilde{t}-\tilde{s}\right)\\ &+\left[a_2 - \frac{1}{4}\tilde{\varepsilon}\tilde{S}_{L,0}\tilde{s}\left(a_1^{\,2} - b_1^{\,2}\right) + \frac{\tilde{\varepsilon}\tilde{S}_{L,0}\tilde{s}}{2}\sum_{n=1}^{\infty} n(n+2)\cdot\left(a_n a_{n+2} + b_n b_{n+2}\right)\right]\cdot\cos\left(2\tilde{t}-2\tilde{s}\right) \qquad \text{(G.1)}\\ &+\left[b_2 - \frac{1}{2}\tilde{\varepsilon}\tilde{S}_{L,0}\tilde{s}\left(a_1 b_1\right) \quad + \frac{\tilde{\varepsilon}\tilde{S}_{L,0}\tilde{s}}{2}\sum_{n=1}^{\infty} n(n+2)\cdot\left(a_n b_{n+2} - b_n a_{n+2}\right)\right]\cdot\sin\left(2\tilde{t}-2\tilde{s}\right)\\ &+ \ldots + O\left(\tilde{\varepsilon}^2\right)\end{aligned}$$

APPENDIX H

In the case of isotropic turbulence, based on the longitudinal $f(r,t)$ and transverse correlation function, $g(r,t)$, all corelation function can be reconstructed using the following [Pope page 196.]

$$R_{u_i u_j}(\vec{r},\tau) \equiv g(r,t)\delta_{ij} + \left[f(r,t) - g(r,t) \right] \frac{r_i r_j}{r^2} \tag{H.1}$$

$$g(r,t) = f(r,t) + \frac{1}{2} r \frac{\partial}{\partial r} f(r,t) \tag{H.2}$$

Then, applying

$$\begin{aligned} R_{u_i u_j}(s_1,s_2,s_3,\tau) &\equiv \frac{\left\langle f_i(x_1,x_2,x_3,t)\, f_j(x_1+s_1,x_2+s_2,x_3+s_3,t+\tau) \right\rangle}{\sqrt{\left\langle f_i^{\,2} \right\rangle \left\langle f_j^{\,2} \right\rangle}} \\ &= \left(\frac{\pi}{4} \frac{\sigma_i \sigma_j}{L_{11}^{\,2}} + \left(1 - \frac{\pi}{4} \left(\frac{\boldsymbol{r}}{L_{11}} \right)^2 \right) \delta_{ij} \right) \cdot \exp\left(-\frac{\pi}{4} \left(\frac{\boldsymbol{r}}{L_{11}} \right)^2 \right) \end{aligned} \tag{H.3}$$

From Eqs. (7.6) and (7.7) the full correlation functions can be derived as:

$$\begin{aligned} R_{u_i u_j}(\chi_1,\chi_2,\chi_3,\tau) &\equiv \frac{\left\langle f_i(x_1,x_2,x_3,t)\, f_j(x_1+\chi_1,x_2+\chi_2,x_3+\chi_3,t+\tau) \right\rangle}{\sqrt{\left\langle f_i^{\,2} \right\rangle \left\langle f_j^{\,2} \right\rangle}} \\ &= \left(\frac{\pi}{4} \frac{\sigma_i \sigma_j}{L_{11}^{\,2}} + \left(1 - \frac{\pi}{4} \left(\frac{\boldsymbol{r}}{L_{11}} \right)^2 \right) \delta_{ij} \right) \cdot \exp\left(-\frac{\pi}{4} \left(\frac{\boldsymbol{r}}{L_{11}} \right)^2 \right) \end{aligned} \tag{H.4}$$

where,

$$\begin{aligned} &(\ )_1 : s-direction, \quad (\ )_2 : n-direction, \quad (\ )_3 : z-direction, \\ &\sigma_1 = \chi_1 - u_{s,0}\tau, \quad \sigma_2 = \chi_2 + S_L \tau, \quad \sigma_3 = \chi_3, \\ &\boldsymbol{r} = \sqrt{\sigma_1^{\,2} + \sigma_2^{\,2} + \sigma_3^{\,2}} \end{aligned} \tag{H.5}$$

APPENDIX I

Figure I0.1 illustrates $\tilde{S}_{T,eff}$ over a cycle at selected locations over a normalized curvature.

All collection of different downstream distance is shown in Figure 7.11b.

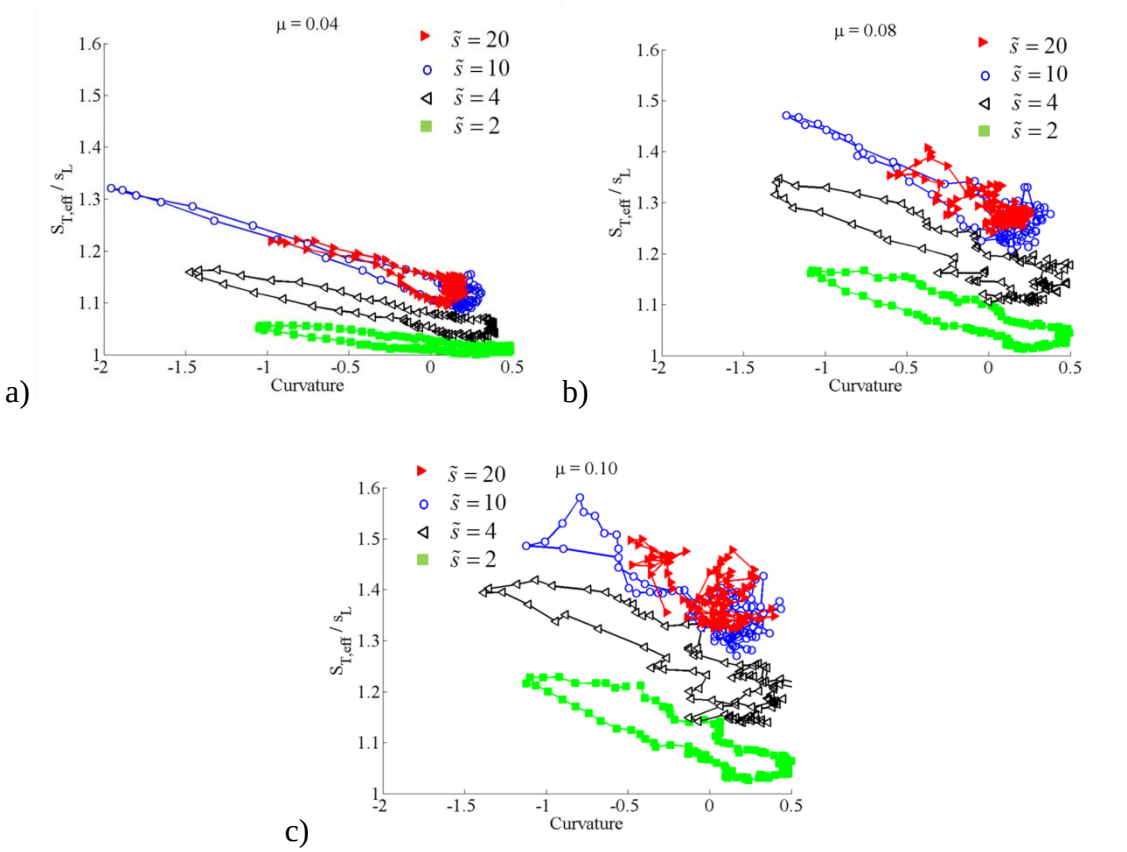

Figure I0.1 Illustration of the $\tilde{S}_{T,eff}$ over a cycle at selected locations over a normalized curvature. a) $\tilde{\mu}$ =0.04 b) $\tilde{\mu}$ =0.08 c) $\tilde{\mu}$ = 0.10 (Other conditions are $\tilde{\varepsilon}$ =0.65 $\tilde{L}_{11}$ =0.65, $\tilde{S}_L$ =0.25).

APPENDIX J

Grid study was performed with refinement of space and time. Figure J0.1 shows comparisons of instantaneous flame position and gain at the forcing frequency, respectively. Twice refinement study shows that results are different by 5% around $\tilde{s}$ =12 downstream distance.

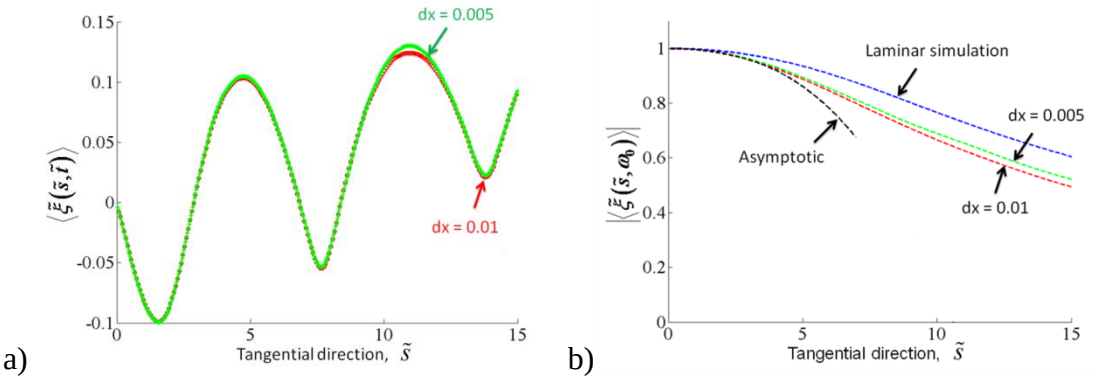

a) b)

Figure J0.1 Comparison of same simulation with different grid size. a) instantaneous flame front. b) gain of the flame response along with laminar simulation and asymptotic solution. (Conditions are $\tilde{\varepsilon}$ =0.65 $\tilde{L}_{11}$ =0.65, $\tilde{S}_L$ =0.25, $\tilde{\mu}$ =0.04).

APPENDIX K

This section compares the Fourier transforms of the flame position in a forced flame by two methods, one by the selected spatial domain and the other by the time domain. The sampling resolutions in time/space will determine the range of the frequencies/wave numbers. This is needed because the temporal sampling frequency for the data shown in Figure 6.11 is not enough to capture the harmonics of the excitation frequency. In the measurement, the sampling frequency is slightly bigger than the twice of forcing frequency, so the temporal Fourier transform cannot capture the harmonics of the fluctuation according to the Nyquist theorem. Still, the harmonic contents can be estimated if the spatial resolution is fine enough. For example, if a signal satisfies a generic form of $F\left(t - x/u_c\right)$, then the spatial Fourier transform is equivalent to the spatial Fourier transform with a constant, u_c.

In order to illustrate this process, we used the results from a numerical simulation result from Sec 6.3.1, which has fine resolutions in space and time. Figure K0.1a shows the one snapshot of the flame position, ξ, over the downstream distance, s, which is the same result shown in Figure 6.4a. Figure K0.1b depicts the time change of the flame position at s/λ_c=2.17, a point indicated in Figure K0.1a. Although Figure K0.1a and b are plotted over different type of domains, the flame position shape around s/λ_c=2.17 is similar to that around t/T=2. Then, the Fourier transforms will be performed to quantify this similarity.

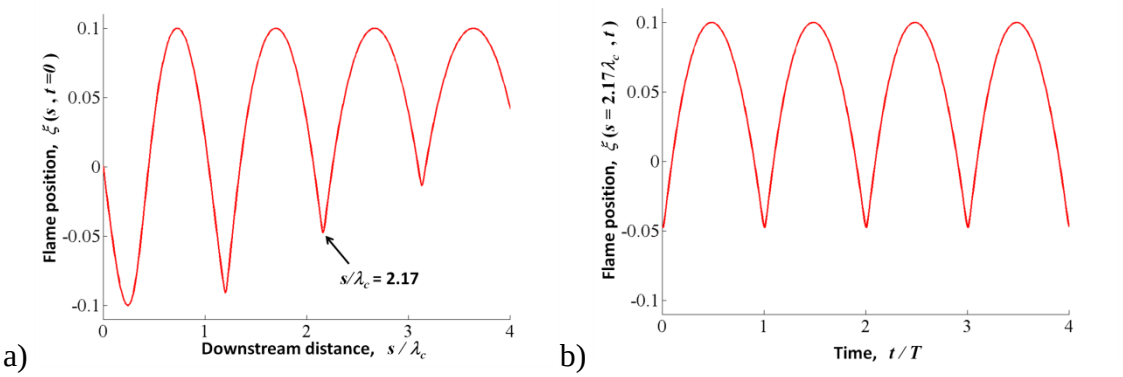

Figure K0.1. a) Dependence of flame position, ξ, upon downstream distance at t=0. b) Dependence of flame position, ξ, upon time at $s/\lambda c$=2.17 (conditions are same as in Figure 6.4a).

In order to perform the Fourier transform, the domain has to be chosen properly. For the time domain, the forcing period will be the proper domain as shown in Figure K0.1b. On the contrary, for the spatial domain, there is no clear domain, rather it evolves downstream distance. For example, the fluctuating amplitude is large near the flame holder and gets smaller further downstream. Therefore, in order to represent the wave shape at the specific location, the minimum length of the spatial domain is required.

This minimum length of the domain was estimated by the phase speed of the flame wrinkles. Consider a signal satisfying $\cos\left(2\pi f_0\left(t - s/u_c\right)\right)$. Then, the minimum length representing the characteristic is the wavelength, λ_f ($=u_c / f_0$), which is equivalent to $2\pi/\left(d\phi/dx\right)$, where ϕ is the phase angle of the Fourier transform of the signal. Therefore, the size of the wave length, λ_f, is determined by obtaining $2\pi/\left(d\phi/dx\right)$ from the measured response. Once the wavelength is determined, the flame position is sampled in a selected spatial domain, centered at a designated location with the width of the wavelength.

Figure K0.2a shows the flame position with the two domains, one by the time domain and the other by the selected spatial domain described in the above. Given these

responses in Figure K0.2a, the Fourier transform were conducted, whose results is shown in Figure K0.2b. Although the domains are different, the gain in the forcing frequency is similar to the gain at the first wave number, and so on with higher harmonics.

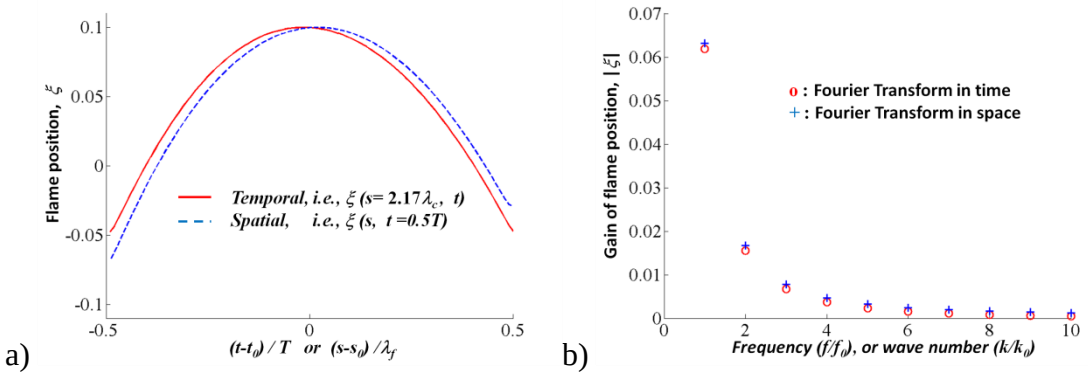

Figure K0.2. a) Dependence of flame position over two different domain, one by the forcing period (t_0 = 0.5T), and the other by the selected spatial domain (s_0 = 2.17λ_c). b) Dependence of the Fourier transform. Data from Figure K0.1.

Lastly, same procedure was performed at all different downstream distance, which is plotted in Figure K0.3. This plot shows the response at the forcing frequency and two harmonics along with the wave numbers (blue dash lines). In addition, the spatial Fourier transform can be performed on different instance, and averaged of the magnitude on different times.

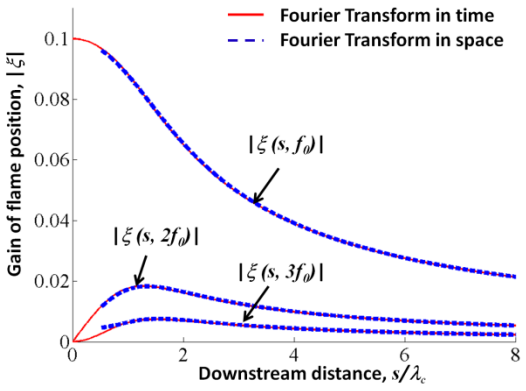

Figure K0.3. Comparison of the Fourier transforms of the flame position, ξ, by two methods, one by the temporal transform and the other by the spatial transform on a selected domain.

REFERENCES

1. *Nitrogen Oxides (NOx), Why and How They Are Controlled*, 2010, U.S. Environmental Protection Agency.
2. *Integrated Science Assessment for Sulfur Oxides - Health Criteria Annexes*, 2008, U.S. Environmental Protection Agency.
3. Zel'dovich, Y.B., *The oxidation of nitrogen in combustion and explosions.* Acta. Physicochimica URSS, 1946. **21**: p. 577.
4. Larsen, C.E., *NASA Experience with Pogo in Human Spaceflight Vehicles*, 2008, NASA Engineering and Safety Center.
5. Lieuwen, T.C. and V. Yang, *Combustion instabilities in gas turbine engines: operational experience, fundamental mechanisms and modeling*. 2005.
6. Blomshield, F.S. *Historical Perspective of Combustion Instability in Motors: Case Studies*. in *37th AIAA Propulsion Conference*. July 2001. Salt Lake City, UT.
7. Rayleigh, J., *The Theory of Sound*. 1945, New York: Dover Publication.
8. Putnam, A.A., *Combustion-driven oscillations in industry*, 1971, New York : American Elsevier.
9. Lieuwen, T. and B.T. Zinn, *The role of equivalence ratio oscillations in driving combustion instabilities in low NOx gas turbines.* Symposium (International) on Combustion, 1998. **27**(2): p. 1809-1816.
10. Dowling, A.P. and J.E.F. Williams, *Sound and sources of sound.* JOHN WILEY & SONS, INC., 605 THIRD AVE., NEW YORK, NY 10158, USA, 1983, 321, 1983.
11. Dowling, A.P., *A kinematic model of a ducted flame.* Journal of Fluid Mechanics, 1999. **394**: p. 51-72.
12. Lee, J.G. and D.A. Santavicca, *Experimental diagnostics for the study of combustion instabilities in lean premixed combustors.* Journal of Propulsion and Power, 2003. **19**(5): p. 735-750.
13. Lee, J.G., K. Kim, and D.A. Santavicca, *Measurement of equivalence ratio fluctuation and its effect on heat release during unstable combustion.* Proceedings of the Combustion Institute, 2000. **28**(1): p. 415-421.
14. Palies, P., et al., *The combined dynamics of swirler and turbulent premixed swirling flames.* Combustion and Flame, 2010. **157**(9): p. 1698-1717.
15. Durox, D., et al., *Experimental analysis of nonlinear flame transfer functions for different flame geometries.* Proceedings of the Combustion Institute, 2009. **32**: p. 1391-1398.
16. Schuller, T., D. Durox, and S. Candel, *A unified model for the prediction of laminar flame transfer functions:: comparisons between conical and V-flame dynamics.* Combustion and Flame, 2003. **134**(1-2): p. 21-34.
17. Kornilov, V.N., et al., *Experimental and numerical investigation of the acoustic response of multi-slit Bunsen burners.* Combustion and Flame, 2009. **156**(10): p. 1957-1970.

18. Giauque, A., et al., *System identification of a large-scale swirled partially premixed combustor using LES and measurements.* Journal of Turbulence, 2005: p. N21.
19. Truffin, K. and T. Poinsot, *Comparison and extension of methods for acoustic identification of burners.* Combustion and Flame, 2005. **142**(4): p. 388-400.
20. Fleifil, M., et al., *Response of a laminar premixed flame to flow oscillations: A kinematic model and thermoacoustic instability results.* Combustion and Flame, 1996. **106**(4): p. 487-510.
21. Shreekrishna, S. Hemchandra, and T. Lieuwen, *Premixed flame response to equivalence ratio perturbations.* Combustion Theory and Modelling, 2010. **14**(5): p. 681-714.
22. Preetham, et al., *Linear Response of Laminar Premixed Flames to Flow Oscillations: Unsteady Stretch Effects.* Journal of Propulsion and Power, 2010. **26**(3).
23. Hemchandra, S., N. Peters, and T. Lieuwen, *Heat release response of acoustically forced turbulent premixed flames-role of kinematic restoration.* Proceedings of the Combustion Institute, 2011. **33**: p. 1609-1617.
24. Shreekrishna and T. Lieuwen. *High Frequency Premixed Flame Response to Acoustic Perturbations* in *15th AIAA/CEAS Aeroacoustic Conference*. 2009. Miami, FL.
25. Palies, P., et al., *Modeling of premixed swirling flames transfer functions.* Proceedings of the Combustion Institute, 2011. **33**(2): p. 2967-2974.
26. Peters, N., *Turbulent Combustion*. 2000: Cambridge Univ Pr.
27. Lieuwen, T., *Unsteady Combustor Physics*. 2013: Cambridge Press.
28. Williams, F.A., *Combustion Theory*. 1985: Addison-Wesley.
29. Aldredge, R., *The speed of isothermal-front propagation in isotropic, weakly turbulent flows.* Combustion Science and Technology, 2006. **178**(7): p. 1201-1215.
30. Huang, Y. and V. Yang, *Dynamics and stability of lean-premixed swirl-stabilized combustion.* Progress in Energy and Combustion Science, 2009. **35**(4): p. 293-364.
31. Pitsch, H. and L. Duchamp de Lageneste, *Large-eddy simulation of premixed turbulent combustion using a level-set approach.* Proceedings of the Combustion Institute, 2002. **29**(2): p. 2001-2008.
32. Menon, S. and W.-H. Jou, *Large-Eddy Simulations of Combustion Instability in an Axisymmetric Ramjet Combustor*. Combustion Science and Technology, 1991. **75**(1-3): p. 53-72.
33. Shanbhogue, S., et al., *Flame sheet dynamics of bluff-body stabilized flames during longitudinal acoustic forcing.* Proceedings of the Combustion Institute, 2009. **32**: p. 1787-1794.
34. Shanbhogue, S., *Dynamics of perturbed exothermic bluff-body flow-fields*, in *School of Aerospace Engineering*2008, Georgia Institute of Technology.
35. Maxworthy, T., *On the mechanism of bluff body flame stabilization at low velocities.* Combustion and Flame, 1962. **6**: p. 233-244.
36. Petersen, R.E. and H.W. Emmons, *Stability of laminar flames.* Physics of Fluids, 1961. **4**(4): p. 456-464.

37. Law, C.K. and C.J. Sung, *Structure, aerodynamics, and geometry of premixed flamelets.* Progress in Energy and Combustion Science, 2000. **26**(4-6): p. 459-505.
38. Turns, S.R., *An introduction to combustion.* Recherche, 2011. **67**.
39. Van Maaren, A. and D.E.G. LPH, *Stretch and the adiabatic burning velocity of methane-and propane-air flames.* Combustion Science and Technology, 1994. **102**(1-6): p. 309-314.
40. Vagelopoulos, C.M., F.N. Egolfopoulos, and C.K. Law, *Further considerations on the determination of laminar flame speeds with the counterflow twin-flame technique.* Symposium (International) on Combustion, 1994. **25**(1): p. 1341-1347.
41. Poinsot, T., T. Echekki, and M.G. Mungal, *A Study of the Laminar Flame Tip and Implications for Premixed Turbulent Combustion.* Combustion Science and Technology, 1992. **81**(1-3): p. 45-73.
42. Echekki, T. and J.H. Chen, *Unsteady strain rate and curvature effects in turbulent premixed methane-air flames.* Combustion and Flame, 1996. **106**(1–2): p. 184-202.
43. Davis, S.G., et al., *An optimized kinetic model of H-2/CO combustion.* Proceedings of the Combustion Institute, 2005. **30**: p. 1283-1292.
44. Smith, G.P., et al., *GRI 3.0*: http://www.me.berkeley.edu/gri_mech/.
45. Venkateswaran, P., et al., *Measurements and analysis of turbulent consumption speeds of H2/CO mixtures.* Combustion and Flame, 2011. **158**(8): p. 1602-1614.
46. Lipatnikov, A. and J. Chomiak, *Turbulent flame speed and thickness: phenomenology, evaluation, and application in multi-dimensional simulations.* Progress in Energy and Combustion Science, 2002. **28**(1): p. 1-74.
47. Karpov, V.P. and E.S. Severin, *Effects of molecular-transport coefficients on the rate of turbulent combustion.* Combustion, Explosion, and Shock Waves, 1980. **16**(1): p. 41-46.
48. Karpov, V., A. Lipatnikov, and V. imont, *A test of an engineering model of premixed turbulent combustion.* Symposium (International) on Combustion, 1996. **26**(1): p. 249-257.
49. Driscoll, J.F., *Turbulent premixed combustion: flamelet structure and its effect on turbulent burning velocities.* Progress in Energy and Combustion Science, 2008. **34**(1): p. 91-134.
50. Cheng, R., K., *Turbulent Combustion Properties of Premixed Syngases*, in *Syngas Combustion*, T. Lieuwen, Yang, V., Editor. To Appear.
51. Gouldin, F. and R.K. Cheng. *International Workshop on Premixed Turbulent Flames*. Available from: http://eetd.lbl.gov/aet/combustion/workshop/workshop.html.
52. Clavin, P. and F. Williams, *Theory of premixed-flame propagation in large-scale turbulence.* Journal of Fluid Mechanics, 1979. **90**(03): p. 589-604.
53. Aldredge, R.C. and F.A. Williams, *Influence of wrinkled premixed-flame dynamics on large-scale, low-intensity turbulent-flow.* Journal of Fluid Mechanics, 1991. **228**: p. 487-511.
54. Creta, F., N. Fogla, and M. Matalon, *Turbulent propagation of premixed flames in the presence of Darrieus-Landau instability.* Combustion Theory and Modelling, 2011. **15**(2): p. 267-298.

55. Creta, F. and M. Matalon, *Propagation of wrinkled turbulent flames in the context of hydrodynamic theory.* Journal of Fluid Mechanics, 2011. **680**: p. 225-264.
56. Evans, L., *Partial Differential Equations (Graduate Studies in Mathematics, Vol. 19).* American Mathematics Society, 1998.
57. Huygens, C., *Treatise on light*, 1962, Dover Publications.
58. Whitham, G., *Linear and nonlinear waves*. Vol. 226. 1974: Wiley New York.
59. Holmes, M.H., *Introduction to perturbation methods*. Texts in applied mathematics. 1995, New York: Springer-Verlag. xiii, 337 p.
60. Jiang, G.S. and D.P. Peng, *Weighted ENO schemes for Hamilton-Jacobi equations.* Siam Journal on Scientific Computing, 2000. **21**(6): p. 2126-2143.
61. Gottlieb, S. and C.W. Shu, *Total Variation Diminishing Runge-Kutta Schemes.* Mathematics of Computation, 1998. **67**(221): p. 73-85.
62. Sethian, J.A., *Level set methods and fast marching methods: evolving interfaces in computational geometry, fluid mechanics, computer vision, and materials science*. 1999: Cambridge Univ Pr.
63. Osher, S. and R.P. Fedkiw, *Level set methods and dynamic implicit surfaces*. Vol. 153. 2003: Springer Verlag.
64. Hemchandra, S. and T. Lieuwen, *Local consumption speed of turbulent premixed flames - An analysis of "memory effects".* Combustion and Flame, 2010. **157**(5): p. 955-965.
65. Dupont, T.F. and Y.J. Liu, *Back and forth error compensation and correction methods for semi-Lagrangian schemes with application to level set interface computations.* Mathematics of Computation, 2007. **76**(258): p. 647-668.
66. Peng, D.P., et al., *A PDE-based fast local level set method.* Journal of Computational Physics, 1999. **155**(2): p. 410-438.
67. Peter, S., *The numerical approximation of a delta function with application to level set methods.* Journal of Computational Physics, 2006. **211**(1): p. 77-90.
68. Wikipedia. *http://en.wikipedia.org/wiki/Bilinear_interpolation*. 2011.
69. Hemchandra, S., *Dynamics of Turbulent Premixed Flames in Acoustic Fields*, in *School of Aerospace Engineering*2009, Georgia Institute of Technology.
70. Hinze, J., *Turbulence*, 1972, McGraw-Hill.
71. Shin, D.H., et al., *Dynamics of a Longitudinally Forced, Bluff Body Stabilized Flame.* Journal of Propulsion and Power, 2011. **27**(1): p. 105-116.
72. Shanbhogue, S.J. and T.C. Lieuwen, *Response of a rod stablized, premixed flame to longitudinal acoustic forcing*, in *ASME Turbo Expo*2006: Barcelona, Spain.
73. Shanbhogue, S.J., et al., *Response of rod stabilized flames to harmonic excitation: shear layer rollup and flame kinematics*, in *Joint Propulsion Conference*2006: Sacramento, CA.
74. Shanbhogue, S.J., M. Seelhorst, and T. Lieuwen, *Vortex phase-jitter in acoustically excited bluff body flames.* International Journal of Spray and Combustion Dynamics, 2009. **1**(3): p. 365-387.
75. Saffman, P.G., *Vortex dynamics*. 1992: Cambridge Univ Pr.
76. Preetham, H. Santosh, and T. Lieuwen, *Dynamics of Laminar Premixed Flames Forced by Harmonic Velocity Disturbances.* Journal of Propulsion and Power, 2008. **24**(6).

77. Michalke, A., *Instability of Compressible Circular Free Jet Regarding Influence of Boundary Layer Thickness of a Jet.* Zeitschrift Fur Flugwissenschaften, 1971. **19**(8-9).
78. Sung, C.J., C.J. Sun, and C.K. Law, *Analytic description of the evolution of two-dimensional flame surfaces.* Combustion and Flame, 1996. **107**(1-2): p. 114-124.
79. Shanbhogue, S. and T. Lieuwen, *Studies on the Vorticity Field of Harmonically Excited Bluff Body Flames*, in *46th AIAA Aerospace Sciences Meeting and Exhibit*2008: Reno, Nevada.
80. Romani, M., *Dynamics of Reacting, Acoustically Excited Bluff-body Flow Fields*, in *Institut fur Luftfahrtantriebe*Aug. 2010, Universitat Stuttgart: Stuttgart, Germany.
81. Schuller, T., D. Durox, and S. Candel, *A unified model for the prediction of laminar flame transfer functions: comparisons between conical and V-flame dynamics.* Combustion and Flame, 2003. **134**(1-2): p. 21-34.
82. Baillot, F., D. Durox, and R. Prudhomme, *Experimental and Theoretical-Study of a Premixed Vibrating Flame.* Combustion and Flame, 1992. **88**(2): p. 149-168.
83. Boyer, L. and J. Quinard, *On the dynamics of anchored flames.* Combustion and Flame, 1990. **82**(1): p. 51-65.
84. Shin, D.H., S.J. Shanbhogue, and T. Lieuwen, *Premixed Flame Kinematics in an Axially Decaying, Harmonically Oscillating Vorticity Field*, in *44th AIAA/ASME/SAE/ASEE Joint Propulsion Conference & Exhibit*2008: Hartford, CT.
85. Emerson, B., et al., *Dynamics of a Transversely Forced, Bluff Body Stabilized Flame*, in *AIAA Aerospace Sciences Meeting and Exhibit*2011: Orlando, FL, USA.
86. Shin, D.-h., et al., *Dynamics of a Longitudinally Forced, Bluff Body Stabilized Flame.* Journal of Propulsion and Power, (to be published).
87. Lieuwen, T., *Modeling premixed combustion-acoustic wave interactions: A review.* Journal of Propulsion and Power, 2003. **19**(5): p. 765-781.
88. Wang, H.Y., C.K. Law, and T. Lieuwen, *Linear response of stretch-affected premixed flames to flow oscillations.* Combustion and Flame, 2009. **156**(4): p. 889-895.
89. Aldredge, R.C., *The Propagation of Wrinkled Premixed Flames in Spatially Periodic Shear-Flow.* Combustion and Flame, 1992. **90**(2): p. 121-133.
90. Lee, D.H. and T.C. Lieuwen, *Premixed flame kinematics in a longitudinal acoustic field.* Journal of Propulsion and Power, 2003. **19**(5): p. 837-846.
91. Searby, G. and D. Rochwerger, *A Parametric Acoustic Instability in Premixed Flames.* Journal of Fluid Mechanics, 1991. **231**: p. 529-543.
92. Vaezi, V. and R.C. Aldredge, *Laminar-flame instabilities in a Taylor-Couette combustor.* Combustion and Flame, 2000. **121**(1-2): p. 356-366.
93. Bychkov, V., *Analytical scalings for flame interaction with sound waves.* Physics of Fluids, 1999. **11**(10): p. 3168-3173.
94. Law, C.K., *Combustion Physics.* Cambridge University, 2006.
95. Bradley, D., P.H. Gaskell, and X.J. Gu, *Burning velocities, markstein lengths, and flame quenching for spherical methane-air flames: A computational study.* Combustion and Flame, 1996. **104**(1–2): p. 176-198.

96. Ayache, S., et al., *Experiments and large-eddy simulations of acoustically forced bluff-body flows.* International Journal of Heat and Fluid Flow, 2010. **31**(5): p. 754-766.
97. Kim, K.T. and S. Hochgreb, *The nonlinear heat release response of stratified lean-premixed flames to acoustic velocity oscillations.* Combustion and Flame, 2011. **158**(12): p. 2482-2499.
98. Thumuluru, S.K., *Effect of Harmonic Forcing on Turbulent Flame Properties*, in *School of Aerospace Engineering*2010, Georgia Institute of Technology: Atlanta GA.
99. Karimi, N., et al., *Linear and non-linear forced response of a conical, ducted, laminar premixed flame.* Combustion and Flame, 2009. **156**(11): p. 2201-2212.
100. Huang, Y., et al., *Experimental investigation of thermoacoustic coupling for low-swirl lean premixed flames.* Journal of Propulsion and Power, 2009. **25**(2): p. 365-373.
101. Kuramoto, Y. and T. Tsuzuki, *Persistent propagation of concentration waves in dissipative media far from thermal equilibrium.* Prog. Theor. Phys, 1976. **55**(2): p. 356-369.
102. Sivashinsky, G.I., *Nonlinear analysis of hydrodynamic instability in laminar flames—I. Derivation of basic equations.* Acta Astronautica, 1977. **4**(11–12): p. 1177-1206.
103. Matalon, M. and B.J. Matkowsky, *Flames as gas-dynamic discontinuities.* Journal of Fluid Mechanics, 1982. **124**(Nov): p. 239-259.
104. Pope, S.B., *Turbulent flows*. 2000: Cambridge Univ Pr.
105. Bendat, J.S. and A.G. Piersol, *Random data: Analysis and measurement procedures*. Vol. 729. 2011: Wiley.
106. Frenkiel, F.N. and P.S. Klebanoff, *Higher-order correlations in a turbulent field.* Physics of Fluids, 1967. **10**(3): p. 507-520.
107. Shin, D.-H. and T. Lieuwen, *Flame wrinkle destruction processes in harmonically forced, laminar premixed flames.* Combustion and Flame, 2012(0).
108. Coats, C.M., *Coherent structures in combustion.* Progress in Energy and Combustion Science, 1996. **22**(5): p. 427-509.
109. Cardell, G.S., *Flow past a circular cylinder with a aermeable splitter plate*, 1993, California Institute of Technology.
110. Peters, N., *A spectral closure for premixed turbulent combustion in the flamelet regime.* Journal of Fluid Mechanics, 1992. **242**: p. 611-629.
111. Lipatnikov, A.N. and J. Chomiak, *Turbulent flame speed and thickness: phenomenology, evaluation, and application in multi-dimensional simulations.* Progress in Energy and Combustion Science, 2002. **28**(1): p. 1-74.
112. Abdel-Gayed, R., D. Bradley, and M. Lawes, *Turbulent burning velocities: a general correlation in terms of straining rates.* Proceedings of the Royal Society of London. A. Mathematical and Physical Sciences, 1987. **414**(1847): p. 389-413.
113. Matalon, M., *On flame stretch.* Combustion Science and Technology, 1983. **31**(3-4): p. 169-181.
114. Evans, L.C., *Partial Differential Equations*. 1997: American Mathematical Society.